eXPRESS Polymer Letters Vol.1, No.4 (2007) 188
Available online at www.expresspolymlett.com
DOI: 10.3144/expresspolymlett.2007.29

Editorial corner – a personal view

Compounding and processing of polymer nanocomposites: from scientific challenges to industrial stakes

P. Krawczak[*]

Department of Polymers and Composites Technology & Mechanical Engineering, Ecole des Mines de Douai, 941 rue Charles Bourseul, BP 10838, 59508 Douai, France

Polymer nanocomposites have emerged as new materials showing promising industrial application potential and have been the focus of an ever-growing interest in the past few years due to their quite exceptional properties at low filler contents (around 5 wt% or less). Compared to neat polymers and depending on the nanofiller used (nanofibres such as carbon nanotubes or cellulose whiskers, nanoplatelets such as layered silicate/clay or layered double hydroxides; nanosized isotropic particles such as silica or titanium dioxide), nanocomposites may offer:

- better mechanical properties (e.g. strength and modulus) and dimensional stability (reduced shrinkage and warpage)
- reduced permeability to gases and improved chemical resistance
- better thermal stability and heat deflection temperature
- flame retardancy and reduced smoke emissions.

However only well-dispersed and well-exfoliated nanoparticles can lead to the expected improvement of properties. Raw material producers, converters and end-users have therefore to tackle both compounding and processing issues. Surface modification of nanofillers with organic surfactant and adaptation of compounding conditions (high shear, high residence time, special screw profile design in case of melt compounding for example) may help to get rid of most of compounding issues. Research groups have made significant progress in that field. The development of masterbatches has reduced the health and safety hazards. The final injection- or extrusion-moulded part may be easily obtained by mixing/diluting the masterbatch with the appropriate polymer matrix. The nanoparticle dispersion (and exfoliation where applicable) is usually assumed to be achieved during the masterbatch compounding. Experience unfortunately often shows that the industrial reality is quite different. More research efforts are still required to identify the processing conditions that allow maintaining the dispersion and avoiding nanoparticle to aggregate again in the manufactured products.

In conclusion the high potential of nanocomposites has already been demonstrated at the lab scale. There is now time to bridge the gap between scientific challenges and industrial stakes. The key issue is currently to maintain nanoparticle dispersion during the industrial scale processing of nanocomposites on machines and equipments that are used to manufacture polymer composites parts on a regular basis. Efforts have to be oriented in this direction.

Prof. Dr. Patricia Krawczak
Member of International Advisory Board

---

[*]Corresponding author, e-mail: krawczak@ensm-douai.fr

© BME-PT and GTE

eXPRESS Polymer Letters Vol.1, No.4 (2007) 189–196
Available online at www.expresspolymlett.com
DOI: 10.3144/expresspolymlett.2007.30

Analysis of polymer grafted inside the porous hydrogel using confocal laser scanning microscopy

I. N. Savina[1,2], *M. Tuncel*[3], *A. Tuncel*[4], *I. Yu. Galaev*[1*], *B. Mattiasson*[1]

[1]Department of Biotechnology, Center for Chemistry and Chemical Engineering, Lund University, Box 124, SE-22100, Lund, Sweden
[2]Protista Biotechnology AB, P.O. Box 86, SE-26722 Lund, Sweden
[3]Department of Anatomy, Faculty of Medicine, Hacettepe University, 06532 Beytepe, Ankara, Turkey
[4]Chemical Engineering Department, Hacettepe University, 06532 Beytepe, Ankara, Turkey

Received 29 January 2007; accepted in revised form 24 March 2007

Abstract. Graft polymerization of glycidyl methacrylate onto the pore surface of polyacrylamide macroporous gel was implemented in DMSO-aqueous solution using diperiodatocuprate(III) complexes as an initiator. The grafting densities up to 410% were achieved. The graft polymerization was confirmed by gravimetrical methods and FTIR. The graft polymerization of polymer inside the pores of the macroporous gel resulted in increased flow resistance through the gel matrix. The distribution of grafted polymer on the gel pore surface material was studied by scanning electron microscopy (SEM) and confocal laser scanning microscopy (CLSM). CLSM is an alternative method for studying morphology of gel surface with grafted polymer having the advantages over the SEM allowing to investigate the distribution of grafted polymer inside the hydrogel in a native hydrated state. The microscopic techniques demonstrated uneven distribution of the grafted polymer inside the gel pores as a result of initiating the graft polymerization by insoluble initiator deposited on the pore surface.

Keywords: *polymer gels, material testing, graft polymerization, confocal laser scanning microscopy*

1. Introduction

Hydrogels with mobile polymer chains terminally or loop-wise attached to the hydrogel polymer backbone are of interest for different applications in the biotechnological, medical and pharmaceutical field. Generically, polymer chains of various nature (hydrophilic-hydrophobic, ion-exchange, stimuli-responsive polymer chains) could be introduced into the hydrogel backbone by graft polymerization providing hydrogels with additional behaviour. Thus the wettability, biocompatibility, and water content of the hydrogels were improved by grafting polymer chains from polymer backbone [1]. The terminally attached polymer chains are flexible and capable of fast changing their conformation. This feature has been used for increasing the swelling degree and swelling rate of hydrogels [2] and to accelerate the rate of shrinking/swelling of stimuli-sensitive hydogels in response to changes of external condition (pH, temperature) [3, 4]. The localization of functional groups (cation-exchange, anion-exchange, affinity, etc.) at the polymer chains terminally attached to hydrogel surface makes it possible to increase the loading capacity and mass transfer rates and results in marked changes in selectivity of hydrogels during their interactions with biological nano- and macroparticles [5, 6]. Thus the grafted hydrogels have attracted a considerable attention as promising materials for producing new stimuli-responsive drug delivery systems [7–9], biomimetic actuators [10] or chromatographic materials [6].

---

[*]Corresponding author, e-mail: igor.galaev@biotek.lu.se

© BME-PT and GTE

The hydrogels with terminally bound polymer chains could be prepared by different methods. Hydrogels with freely mobile polymer chains terminally attached onto polymer backbone were prepared by co-polymerization of monomer mixture containing macromonomer [4, 5, 11] or as a result of cross-linking of preformed grafted polymer [12]. Grafting polymers onto an already prepared gel surface is another method, commonly used for gel surface modification. This could be implemented using *grafting to* method, when the preformed polymer chains with terminally functional groups covalently bound to the surface [13], or using *grafting from* method, when the polymer chains are grown via monomer polymerization initiated from the active sites on the gel surface [14]. When comparing these two methods, the *grafting from* method allows the formation of grafted layer with higher density and thickness of polymer brushes, which could be controlled by the amounts of monomer and catalyst used. The formation of high density of polymer brushes using *grafting to* method is difficult because of steric crowding of reactive sites at the gel surface by already bound polymer chains.

The structure of grafted layer, thickness, density and distribution of polymer grafted in the bulk of hydrogel, is very important considering controlling the gel behavior. Introduction of additional grafted polymer into the gel backbone is usually characterized by using gravimetric methods, infrared spectral analysis and different scanning calorimetry. The determination of the structure of polymer layer grafted on the surface of hydrogel presents especially a big challenge. In this case, the polymer brushes could not be analyzed by techniques traditionally used for the analysis of polymer brushes grafted on flat surfaces like AFM, ellipsometry, surface plasmon resonance or using quartz crystal microbalance. The microscopic methods give the possibility to look inside the bulk structure of polymer materials and visualize the surface morphology of the porous polymer material. Scanning electron microscopy (SEM) has been used for the study of the surface morphology of grafted hydrogels [1]. It reveals the formation of additional polymer layer on the surface of hydrogels. However, sample preparation for SEM requires drying the sample followed by metal coating that might alter hydrogel morphology and the picture obtained represents grafted polymer layer in dehydrated state. This problem could be solved by applying confocal laser scanning microscopy (CLSM). CLSM offers advantages over conventional SEM procedures as it does not require special water removal prior to examination that allows for studying the bulk structure of hydrogel samples in their native state [15–17].

CLSM is a technique to gain high resolution views of thick specimens by rejection of out of focus scattering. Through the use of a pinhole aperture, light emerging from material above and below the plane of interest is effectively blocked, resulting in the detection of light from a thin specimen slide that is centred on the focal plane. This feature of CLSM, known as ‘optical sectioning’, makes it possible to scan at various *x-y* planes corresponding to different depths of the sample, and, thus to reconstruct the 3-D region of the specimen. CLSM has been widely used for investigation of the bulk structure of polymer materials [15–17]. However to the best of our knowledge there were no reports on the study of polymer grafted on the surfaces in the bulk of porous hydrogel material. Studies on grafted polymers with CLSM are mainly restricted to flat surfaces. For example, Nakayama *et al.* studied the thickness of grafted polymer layer on the surface of PET films using CLSM [18]. The grafted surface was treated by staining with rose bengal, which fluorescence light was observed under a fluorescent microscope. The fluorescence intensity, which can be correlated to the graft yields, provides the information about thickness of grafted polymer layer on the polymer film.

In this study we have attempted to use CLSM for studying the distribution of grafted polymer on the pore surface in the bulk of porous gel material. Glycidyl methacrylate (GMA) was grafted onto the surface of macroporous polyacrylamide gel, so called cryogel (pAAm cryogel) [19], using diperiodatocuprate(III) as initiator. The gel pore surface morphology and distribution of grafted polymer in the bulk of grafted pAAm cryogel were studied by SEM and CLSM.

2. Experimental part

2.1. Materials

Glycidyl methacrylate (GMA, ≥97% purity) was from Fluka (Seelz, Germany) and used without additional purification. Acrylamide (AAm, more than 99.9 % purity, electrophoresis reagent), methylene-*bis*-acrylamide (MBAA, 99%), N,N,N',N'-tetra-methyl-ethylenediamine (TEMED, 99%), ammonium persulfate (APS, 98%) and fluoresceinamine, isomer I were from Aldrich (Steinheim, FRG). The potassium diperiodatocuprate(III) solution contained 0.056 M of Cu (III) was prepared according to the method described previously [20]. The rest of chemicals were of the best quality available.

2.2. Methods

2.2.1. Preparation of pAAm cryogels

Dry pAAm cryogels were provided by Protista Biotechnology AB (Lund, Sweden). The pAAm cryogels were prepared in glass tubes from polymerization medium containing 6 w/v% (AAm+MBAA) and 8/1 AAm/MBAA, the amount of APS as well as TEMED was 1.2 w/w% of the total monomer weight. The polymerization solution in the tubes was frozen at –12°C and kept at this temperature for 20 h. After thawing and washing with water (200 ml) the gel matrix was dried at 60°C and stored in dry state.

2.2.2. Preparation of the grafted cryogels

Graft polymerization was carried out according to method described earlier [21]. A dried pAAm cryogel (0.10±0.03 g) was placed in a glass tube and saturated with initiator solution (0.35 M Cu(III), 1 M NaCl). The columns saturated with initiator solution were incubated for 10 min at room temperature and then washed with degassed solution of 0.5 M NaCl until pH of washing solution was 7.0. The samples were incubated at 40°C for 30 min. The monomer solutions in DMSO (70 v/v%) was passed through the gel matrix at a flow rate of 2 ml/min. The flow was stopped by corking the glass tube. The glass tubes were placed in water-bath at 80°C for 4 h. Any soluble homopolymer of GMA was extracted from the grafted cryogels with DMSO. The un-reacted diperiodatocuprate(III) and reaction byproducts were removed by washing with 30 ml 0.1 M HCl. Finally, the gel was washed with an excess of deionized water.

2.2.3. Characterization of graft cryogels

The grafting degree (*G*) and density (*D*) of the graft polymerization were calculated as Equations (1), (2):

$$G\,[\%] = \frac{W_1 - W_0}{W_0}\cdot 100 \qquad (1)$$

$$D\,[\text{mmole/ml}] = \frac{W_1 - W_0}{V}\cdot\frac{1000}{M_w} \qquad (2)$$

where W_0 and W_1, are the weights [g] of original and grafted samples, respectively. V is the volume [ml] of sample, M_w is the molecular weight of monomer used for the graft polymerization.

Flow rate of water passing through the column was measured at the constant hydrostatic pressure equal to 100 cm of water-column corresponding to a pressure of circa 0.01 MPa according to Plieva *et al.* [22].

The FTIR spectra of dried plain cryogel and grafted cryogel in potassium bromide pellets were recorded using an FTIR-8300 spectrophotometer (Shimadzu). Scanning electron microscopy was carried out using JEOL JSM-5600LV scanning electron microscope [22].

Confocal microscopy was carried out as follows. A disc of approximately 1 mm in height was cut from the wet cryogel monolith. The disk was labelled with fluoresceinamine and examined in confocal laser scanning microscope (CLSM, Leica SP2, Heidelberg, Germany) equipped with He-Ne laser. The disc was placed on a glass slide with a cover slip. CLSM images were taken from the disc interior with both maximum projection and transparency modes. The excitation and emission wavelengths were 488 and 519 nm, respectively. All images were generated by optical sectioning in z-direction. For this purpose, 500 optical sections were taken along with a z-distance of 160 µm. The samples were stained with fluoresceinamine which was covalently bound to the grafted poly-GMA as follows. Dried cryogels were placed in glass tube and saturated with solution of fluoresceinamine (50 mg/ml in aqueous solution of DMSO, 50 v/v%, pH 7.0). The glass tubes were sealed and placed in thermostated bath at 70°C for 5 h. Then the cryogel was washed with excess of water to remove unbound fluoresceinamine.

3. Results and discussion

Glycidyl methacrylate (GMA) was grafted onto the pore walls of macroporous polyacrylamide hydrogel, so called cryogel (pAAm cryogel), using diperiodatocuprate as initiator. Cryogels are produced by radical copolymerization of acrylamide with methylene-*bis*-acrylamide in partially frozen reaction media [22, 23]. They are characterized by dense non-porous polymer walls and a system of large interconnected pores filled with water. The swollen cryogel fill up the glass tubes where it was prepared so that the liquid when applied on top of the gel plug passes through the interconnected porous system of the cryogel. The cryogel with mean pore size about 35 μm with pore size distribution of 5–100 μm was used in this study [24, 25]. The structure of large interconnected pores of cryogels promote grafting providing an ample surface for grafting and ensuring a good mass transport of reagents in the bulk of the gel matrix. Soluble (non-grafted) homopolymer and insoluble by-products of initiator oxidation formed during the polymerization reaction are easily washed out after finishing the graft polymerization.

Graft polymerization of GMA was initiated by diperiodatocuprate(III) which is an efficient initiator of radical polymerization of vinyl monomers on the polyacrylamide backbone [21, 26, 27]. Diperiodatocuprate(III) forms, via redox reaction with amide groups on the polymer backbone, amidil radicals which initiate radical polymerization (for mechanism see Zhang *et al.* [28]). The graft polymerization was implemented using a two-steps method: saturating the cryogels with aqueous solution of initiator and replacing it with monomer solution in aqueous-organic mixture. The initiator was deposited onto the pore surface in the form of insoluble sodium diperiodatocuprate(III) during the saturation with initiator solution. The soluble initiator and KOH presented in the initiator solution were removed by washing with NaCl (see methods). This approach allows implementing effective graft polymerization of water insoluble GMA in the DMSO-water medium and allows avoiding the high-alkaline conditions during the graft polymerization, decreasing the risk of hydrolysis of epoxy groups and the polyacrylamide backbone during the graft polymerization [21].

The cryogels with high density of grafted GMA up to 1.44 mmol/ml of cryogel (grafting percentage, $G\% = 410\%$) were prepared using this method. The grafting percentage ($G\%$) and the density of GMA grafted (D_{GMA}, mmol/ml of cryogel) increase with increase in the monomer concentration (Table 1).

Table 1. The grafting percentage (G%) and the density (D_{GMA}) of GMA grafted pAAm cryogel

Monomer concentration [M]	G [%]	D_{GMA} [mmol/ml of cryogel]
0.1	15	0.05
0.3	79	0.28
0.5	150	0.53
0.7	191	0.67
1.0	275	1.00
1.5	410	1.44

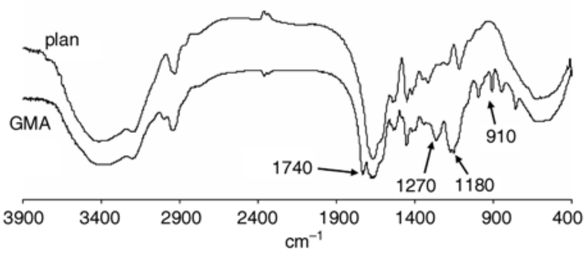

Figure 1. FTIR-spectra of non-grafted (plain) and GMA-grafted pAAm cryogels

The grafting of GMA was confirmed by comparing FTIR spectra of grafted and non-grafted, plain cryogel. In FTIR spectrum of GMA-grafted pAAm cryogel, the strong band of C(=O)–O stretching vibration appeared in the region 1270 cm^{-1} (Figure 1). This band together with the $\nu C{=}O$ at 1740 cm^{-1} revealed the ether structure in the grafted polymer [29]. The presence of the 910 cm^{-1} band indicated the incorporation of epoxy groups [29]. There is the strong band at 1170 cm^{-1} in the spectrum of GMA-grafted pAAm cryogel. This band could be related to C–N stretching vibration and NH in-plane deformation of secondary amides [29]. These data confirm initiation of graft polymerization from the amide group of redox reaction of diperiodatocuprate(III) with amide groups on the polymer backbone pAAm cryogel ($–C(=O)NH_2$) and formation of grafted polymer chain (–C(=O)NH-polyGMA).

The graft polymerization of the polymer inside the cryogel resulted in increased flow resistance of the cryogel (Figure 2). Previously, it was demonstrated that measuring the flow rates through the grafted pAAm cryogel monoliths at the constant pressure of water column represents a simple method for the comparative study of pore structure of the cryogel samples and the changes in the pore structure imposed additionally by the grafted polymer layer [30]. The presence of the high concentration of the grafted polymer inside the pores localized near the pore surface obstructed the flow of solutes through the GMA-grafted pAAm cryogel matrix increasing the flow resistance.

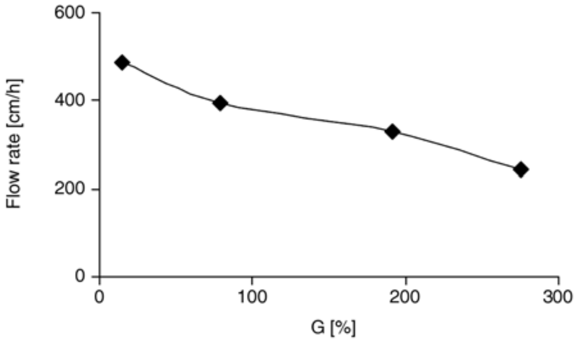

Figure 2. Flow rate of water through the GMA-grafted cryogel

The distribution of the grafted polymer within the pore of the cryogel was studied by SEM. SEM clearly demonstrated the formation of newly-formed polymer phase inside the cryogel pores (Figure 3, for structure of non-grafted pAAm cryogel see Figure 2 in Plieva *et al.* [23]). The grafted polymer is visible in the form of particles of different shape and size, which are unevenly distributed over the polymer surface of the cryogel walls (Figure 3). There are areas with small particles (less then 1 μm) 'evenly' distributed within restricted area together with the particles of large size up to 20 μm (Figure 3a, b). Moreover the rod- and star-shaped particles of the grafted polymer of the size ca. 100 μm are also present (Figure 3c, d). As the graft polymerization has been initiated with insoluble initiator, sodium diperiodatocuprate(III) complexes, deposited at the surface of the pores, the uneven distribution of the insoluble initiator could result from the efficient synthesis of grafted polymer occurring at specific sites rather than producing molecular brushes covering evenly the surface of pores. Thus the SEM demonstrated that the graft polymerization initiated by initiator deposited at the surface resulted in an uneven distribution of grafted polymer and formation of the small and large polymer pieces of grafted polymer in the cryogel pores.

However, when using SEM the cryogel sample must be dried before investigation thus it could represent the altered structure of the grafted cryogel. Therefore, in our study we have attempted to use CLSM for the characterization of the bulk structure of the grafted cryogel. With this technique water does not need to be removed prior to examination and the surface morphology of the cryogel and the layer of grafted polymer could be studied in hydrated state and in much depth compared to

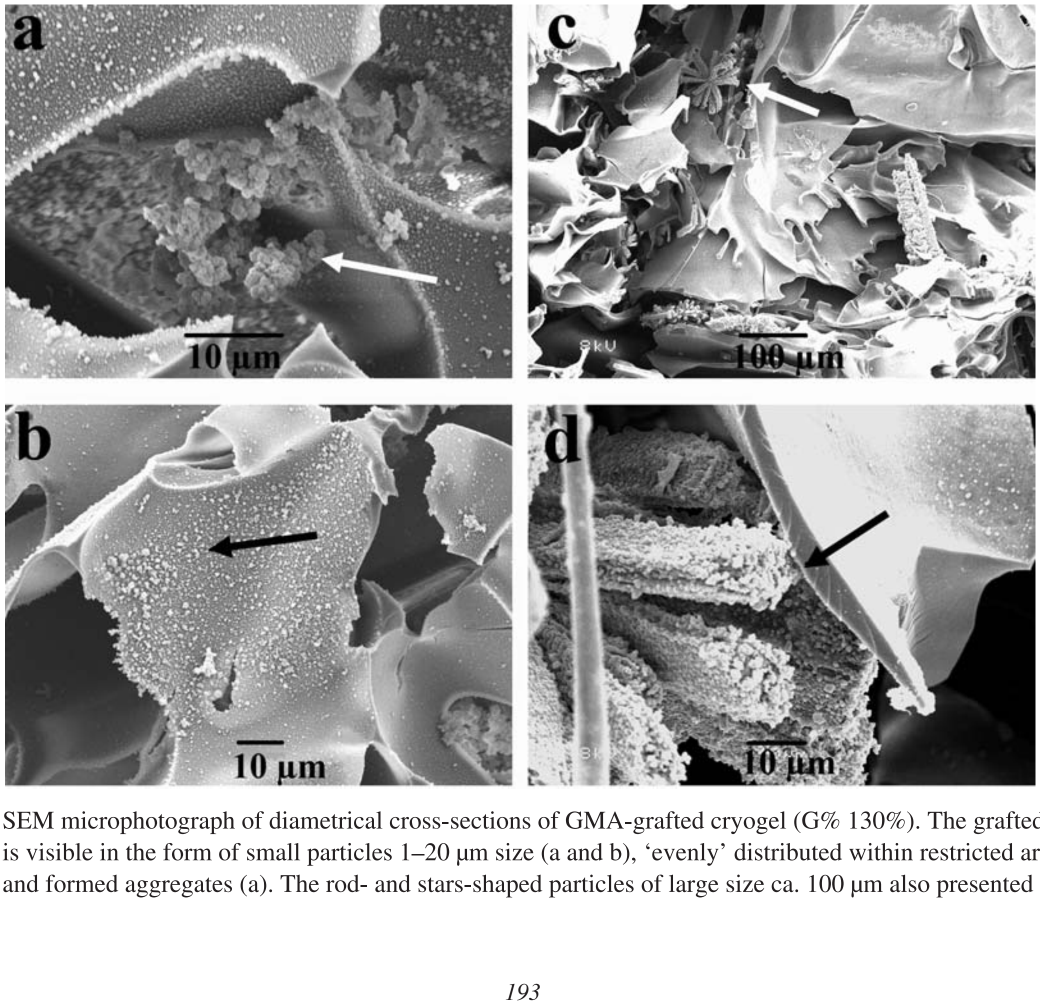

Figure 3. SEM microphotograph of diametrical cross-sections of GMA-grafted cryogel (G% 130%). The grafted polymer is visible in the form of small particles 1–20 μm size (a and b), 'evenly' distributed within restricted area (b) and formed aggregates (a). The rod- and stars-shaped particles of large size ca. 100 μm also presented (c and d)

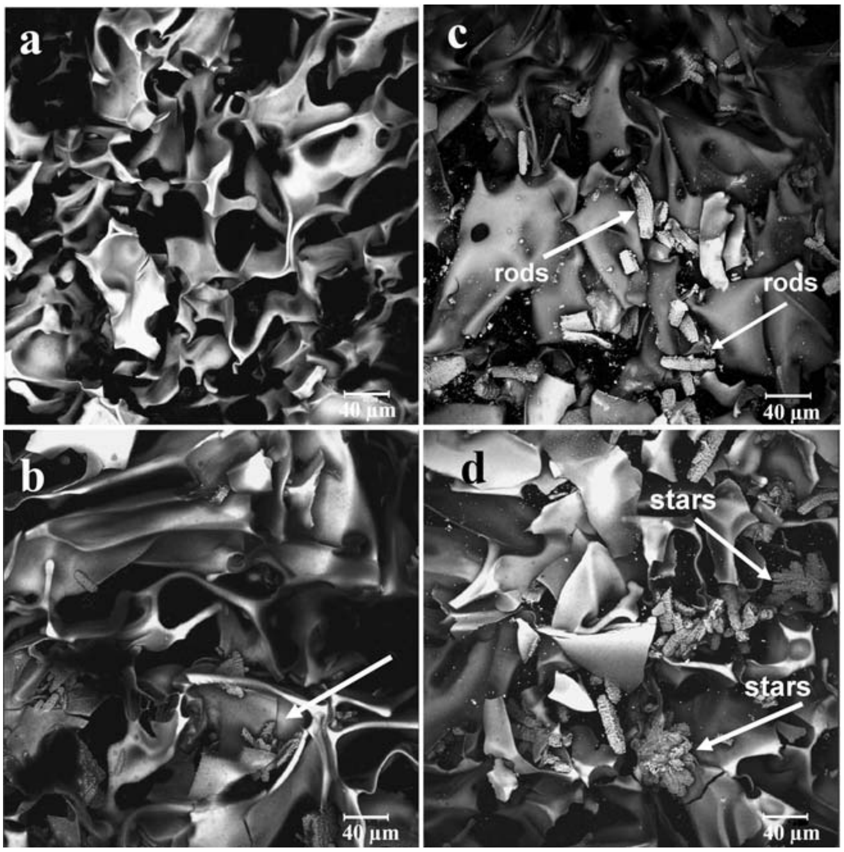

Figure 4. CLSM microphotographs of non-grafted (a) and GMA-grafted (b, c, d) pAAm cryogel. The grafted polymer are visible in the form of rod- and star-shaped particles (b, c and d)

when SEM was used. It should be mentioned, that at present there is no other direct technique suitable for studying the structure of layers of polymer grafted inside the porous hydrogel material in its native hydrated state.

The grafted layer was stained by covalent coupling of fluoresceinamine to epoxy groups and the result was visualized by CLSM, the 3D images were reconstructed representing the structure of the grafted cryogel in the native non-dehydrated state. The CLSM despite somewhat lower resolution than SEM, revealed the same macrostructure of the cryogel as SEM did with thick polymer walls and large pores up to 100 μm (Figure 4a). The grafted polymer of GMA was present in the form of particles of different shape (Figure 4b, c, d). CLSM also revealed uneven distribution of grafted GMA in the pores of the cryogel along with the formation of the large rods- and star-shaped particles supporting the mechanism of uneven formation of the initiating centers on the gel surface during the graft polymerization initiated by the initiator deposited on the surface (Figure 4b, c, d). Thus, in order to control *grafting from* in a rational way it is important not only to control the grafting efficiency i. e. how much polymer is grafted, but it is also vital for the production of the material with desired properties to control how the grafted polymer is distributed along the surface (in this particular case the surface of macropores) used for the grafting.

4. Conclusions

GMA was effectively grafted onto the surface of pAAm cryogel using diperiodatocuprate(III) as initiator. The high densities of GMA grafting up to 1.44 mmole of GMA per ml of cryogel or 410% grafting have been achieved. FTIR, SEM and CLSM confirmed the formation of additional grafted polymer attached to the pore walls of the pAAm cryogel. SEM and CLSM were successfully used for studying of morphology of the gel surface with grafted polymer. CLSM has the advantage over SEM allowing investigations of the distribution of the grafted polymer inside the hydrogel in their native hydrated state. Both microscopic techniques demonstrated uneven distribution of the grafted polymer inside the gel pores as a result of initiating the graft polymerization by insoluble initiator deposited on the pore surface.

Acknowledgements

This work was financially supported by Protista International AB (Bjuv, Sweden), The Swedish Foundation for Strategic Research, The Swedish Foundation for International Cooperation in Research and Higher education (STINT, IG2003-2089), The Swedish Research Council (Projects 348-2004-4916 and 621-2005-3604) and The Swedish Institute (Visby Program, project 01211/2004).

References

[1] Shukla S., Bajpai A. K., Kulkarni R. A.: Preparation, characterization, and water-sorption study of polyvinyl alcohol based hydrogels with grafted hydrophilic and hydrophobic segments. Journal of Applied Polymer Science, **95**, 1129–1142 (2005).

[2] Mahdavinia G. R., Zohuriaan-Mehr M. J., Pourjavadi A.: Modified chitosan III, superabsorbency, salt- and pH-sensitivity of smart ampholytic hydrogels from chitosan-g-PAN. Polymers for Advanced Technologies, **15**, 173–180 (2004).

[3] Kaneko Y., Nakamura S., Sakai K., Aoyagi T., Kikuchi A., Sakurai Y., Okano T.: Rapid deswelling response of poly(N-isopropylacrylamide) hydrogels by the formation of water release channels using poly(ethylene oxide) graft chains. Macromolecules, **31**, 6099–6105 (1998).

[4] Yoshida R., Uchida K., Kaneko Y., Sakai K., Kikuchi A., Sakurai Y., Okano T.: Comb-type grafted hydrogels with rapid deswelling response to temperature changes. Nature, **374**, 240–242 (1995).

[5] Kaufmann M.: Unstable proteins: how to subject them to chromatographic separations for purification procedures. Journal of Chromatography B: Biomedical Sciences and Applications, **699**, 347–369 (1997).

[6] Müller W.: New ion exchangers for the chromatography of biopolymers. Journal of Chromatography A, **510**, 133–140 (1990).

[7] Peppas N. A.: Devices based on intelligent biopolymers for oral protein delivery. International Journal of Pharmaceutics, **277**, 11–17 (2004).

[8] Pourjavadi A., Sadeghi M., Hosseinzadeh H.: Modified carrageenan. 5. Preparation, swelling behavior, salt- and pH-sensitivity of partially hydrolyzed crosslinked carrageenan-graft-polymethacrylamide superabsorbent hydrogel. Polymers for Advanced Technologies, **15**, 645–653 (2004).

[9] Kumashiro Y., Ooya T., Yui N.: Dextran hydrogels containing poly(N-isopropylacrylamide) as grafts and cross-linkers exhibiting enzymatic regulation in a specific temperature range. Macromolecular Rapid Communications, **25**, 867–872 (2004).

[10] Kaneko Y., Sakai K., Kikuchi A., Sakurai Y., Okano T.: Fast swelling/deswelling kinetics of comb-type grafted poly(N-isopropylacrylamide) hydrogels. Macromolecular Symposia, **109**, 41–53 (1996).

[11] Kuckling D., Wohlrab S.: Synthesis and characterization of biresponsive graft copolymer gels. Polymer, **43**, 1533–1536 (2002).

[12] Lowman A. M., Peppas N. A.: Analysis of the complexation/decomplexation phenomena in graft copolymer Networks. Macromolecules, **30**, 4959–65 (1997).

[13] Kim J. H., Lee S. B., Kim S. J., Lee Y. M.: Rapid temperature/pH response of porous alginate-g-poly(N-isopropylacrylamide) hydrogels. Polymer, **43**, 7549–7558 (2002).

[14] Han T. L., Kumar R. N., Rozman H. D., Noor M. A. M.: GMA grafted sago starch as a reactive component in ultra violet radiation curable coatings. Carbohydrate Polymers, **54**, 509–516 (2003).

[15] Tjia J. S., Moghe P. V.: Analysis of 3-D microstructure of porous poly(lactide-glycolide) matrixes using confocal microscopy. Journal of Biomedical Materials Research, **43**, 291–299 (1998).

[16] Risbud M. V., Bhonde R. R.: Polyamide 6 composite membranes: Properties and in vitro biocompatibility evaluation. Journal of Biomaterials Science. Polymer edition, **12**, 125–136 (2001).

[17] Saito H., Nakanishi K., Hirao K., Jinnai H.: Mutual consistency between simulated and measured pressure drops in silica monoliths based on geometrical parameters obtained by three-dimensional laser scanning confocal microscope observations. Journal of Chromatography A, **1119**, 95–104 (2006).

[18] Nakayama Y., Matsuda T.: Surface macromolecular architectural designs using photo-graft copolymerization based on photochemistry of benzyl N,N-diethyldithiocarbamate. Macromolecules, **29**, 8622–8630 (1996).

[19] Lozinsky V. I., Galaev I. Y., Plieva F. M., Savina I. N., Jungvid H., Mattiasson B.: Polymeric cryogels as promising materials of biotechnological interest. Trends in Biotechnology, **21**, 445–451 (2003).

[20] Jaiswal P. K., Yadava K. L.: Determination of sugars and organic acids with periodato complex of copper(III). Indian Journal of Chemistry, **11**, 837–838 (1973).

[21] Savina I. N., Galaev I. Y., Mattiasson B.: Graft polymerization of vinyl monomers inside macroporous polyacrylamide gel, cryogel, in aqueous and aqueous-organic media initiated by diperiodatocuprate(III) complexes. Journal of Polymer Science Part A: Polymer Chemistry, **44**, 1952–1963 (2006).

[22] Plieva F. M., Andersson J., Galaev I. Y., Mattiasson B.: Characterization of polyacrylamide based monolithic columns. Journal of Separation Science, **27**, 828–836 (2004).

[23] Plieva F. M., Savina I. N., Deraz S., Andersson J., Galaev I. Y., Mattiasson B.: Characterization of supermacroporous monolithic polyacrylamide based matrices designed for chromatography of bioparticles. Journal of Chromatography B: Analytical Technologies in the Biomedical and Life Sciences, **807**, 129–437 (2004).

[24] Plieva F. M., Karlsson M., Aguilar M. R., Gomez D., Mikhalovsky S., Galaev I. Y.: Pore structure in supermacroporous polyacrylamide based cryogels. Soft Matter, **1**, 303–309 (2005).

[25] Persson P., Baybak O., Plieva F., Galaev I. Y., Mattiasson B., Nilsson B., Axelsson A.: Characterization of a continuous supermacroporous monolithic matrix for chromatographic separation of large bioparticles. Biotechnology and Bioengineering, **88**, 224–236 (2004).

[26] Savina I. N., Galaev I. Y., Mattiasson B.: Graft polymerization of acrylic acid onto macroporous polyacrylamide gel (cryogel) initiated by potassium diperiodatocuprate. Polymer, **46**, 9596–9603 (2005).

[27] Savina I. N., Galaev I. Y., Mattiasson B.: Anion-exchange supermacroporous monolithic matrices with grafted polymer brushes of N,N-dimethylaminoethylmethacrylate. Journal of Chromatography A, **1092**, 199–205 (2005).

[28] Zhang X., Liu W. H., Chen Y. M., Gong A. J., Chen C. F., Xi, F.: Self-condensing vinyl polymerization of acrylamide. Polymer Bulletin, **43**, 29–34 (1999).

[29] Roeges N. P. G.: A guide to the complete interpretation of infrared spectra of organic structures. John Wiley and Sons Ltd, Chichester (1994).

[30] Savina I. N., Galaev I. Y., Mattiasson B.: Ion-exchange macroporous hydrophilic gel monolith with grafted polymer brushes. Journal of Molecular Recognition, **19**, 313–321 (2006).

eXPRESS Polymer Letters Vol.1, No.4 (2007) 197–207
Available online at www.expresspolymlett.com
DOI: 10.3144/expresspolymlett.2007.31

Liquid crystalline polymers IX
Main chain thermotropic poly (azomethine – ether)s containing thiazole moiety linked with polymethylene spacers

K. I. Aly[*], *M. A. Abbady, S. A. Mahgoub, M. A. Hussein*

Polymer Laboratory 122, Chemistry Department, Faculty of Science, Assiut University, Assiut, 71516, Egypt

Received 3 December 2006; accepted in revised form 18 March 2007

Abstract. A new homologous series of thermally stable thermotropic liquid crystalline poly(azomethine-ether)s based on thiazole moiety were synthesized by solution polycondensation of 4,4'-diformyl-α,ω-diphenoxyalkanes, **I–IV** or 4,4'-diformyl-2,2'-dimethoxy-α,ω,-diphenoxyalkanes **V–VIII** with the new bis(2-aminothiazole) monomer **X**. A model compound **XI** was synthesized from **X** with benzaldehyde and characterized by elemental and spectral analyses. The inherent viscosities of the resulting polymers were in the range 0.43–1.34 dl/g. All the poly(azomethine-ether)s were insoluble in common organic solvents but dissolved completely in concentrated H_2SO_4 and formic acid. The mesomorphic properties of these polymers were studied as a function of the diphenoxyalkane space length. Their thermotropic liquid crystalline properties were examined by DSC and optical polarizing microscopy and demonstrated that the resulting polymers form nematic mesophases over wide temperature ranges. The thermogravimetric analyses of those polymers were evaluated by TGA and DSC measurements and correlated to their structural units. X-ray analysis showed that polymers having some degree of crystallinity in the region $2\theta = 5–60°$. In addition, the morphological properties of selected examples were tested by scanning electron microscopy.

Keywords: *polymer synthesis, molecular engineering, liquid crystal, thermotropic, thermal properties, thiazole poly(azomethine-ether)s*

1. Introduction

Polymers incorporating mesogenic moieties in the main chain are known to exhibit liquid crystalline behavior. The direct study of mesomorphic homopolymers is however frequently hampered by their high melting points. Lowering of the solid crystal to liquid crystal transition temperature may be effected by separation of the rigid mesogenic moieties with regularly spaced sequences of flexiblizing groups or by co-polycondensation [1, 2]. However, most wholly aromatic poly(azomethine)s have high softening temperatures which make melt spinning and injection molding impracticable [3, 4]. These polymers may start to decompose before reaching the melting point. One method for lowering the high melting point of rod-like polymers is to introduce flexible aliphatic units into the main chain [5]. This lowering may be also achieved by using substituent group, thereby increasing the diameter or decreasing the axial ratio of the mesogenic units [6]. Thermotropic (heat-induced) liquid crystalline behavior of polymeric materials is of considerable current interest, not only because of their potential as high-strength fibers, plastics, moldings, etc [7]. Morgan *et al.* [8] described the preparation and properties of a variety of wholly aromatic melt-anisotropic poly(azomethine)s. However, a literature survey revealed that few poly(azomethine)s had been synthesized [9, 10].

---

[*] Corresponding author, e-mail: Kamal_61@yahoo.com

© BME-PT and GTE

The first poly(azomethine)s were prepared by Guillon and Skoulios [9] from benzidine and 4,4’-diformyl-α,ω-diphenoxydecane. Also, terephthaldehyde was reacted with 4,4’-diamino-α,ω-diphenoxyalkanes to obtain poly(azomethine-ether)s [10]. Li and Chang [11] synthesized a series of poly(azomethine-ether)s by the condensation of 1,4-phenylenediamine and 4,4’-diformyl-α,ω-diphenoxyalkane derivatives and studied their LC properties. On the other hand, the anisotropy of the liquid crystalline mesophase offers the possibility of production of novel high performance materials, exhibiting excellent properties due to a proper arrangement of macromolecules in the mesophase during the processing. Moreover, polymers exhibiting liquid crystallinity consist of macromolecules with rigid structure, characterized by high extension of backbones. A major aim of this work has been to investigate the effect of inclusion of flexible spacers as well as thiazole moiety on the liquid crystal properties. In addition, other characteristics of these polymers such as thermostability, solubility, morphology and crystallinity are discussed.

2. Experimental

2.1. Measurements

Elemental analyses were carried out using an Elemental Analyses system GmbH, VARIOEL, $V_{2.3}$ July 1998 CHNS Mode. Infrared Spectra from 4000–600 cm^{-1} of solid samples of the synthesized monomers and polymers were obtained by the KBr method using a Shimadzu 2110 PC Scanning Spectrophotometer. The ^1H-NMR spectra were recorded on a GNM-LA 400-MHz NMR spectrophotometer at room temperature in DMSO or $CDCl_3$ using TMS as the internal reference. Mass spectra were recorded on a Jeol JMS_{600} mass spectrometer. The inherent viscosity was measured with an Ubbelhode Viscometer in Conc. H_2SO_4 at 30°C (0.5 g/l). The solubility of polymers were examined using 0.02 g of polymer in 3–5 ml of solvent at room temperature. The X-ray diffractographs of the polymers were obtained with a Philips X-ray pw 1710 diffractometer, and Ni-filtered CuK_α radiations. Thermogravimetric analysis (TGA) and differential thermogravmetry (DTG) were carried out in air with TA 2000 thermal analyzer at heating rate of 10°C/min in air. The maximum position of the melting endotherms was taken to be the m.p.s. The isotropization temperatures were determined by observing polymer melts with a polarizing microscope, GARL-ZEISS (JENA) equipped with a hot-stage Chaixmeca (Nancy, France). The temperature at which initial formation of isotropic phases occurred was taken as the isotropization temperature, T_i. At the same time, optical textures of the polymer melts were very closely followed to determine the nature of their mesophase. The morphologies of polymers were examined by scanning electron microscopy (SEM) using a Jeol JSM-5400 LV instrument.

2.2. Reagents and solvents

Diphenylether from (Merck) was used without purification. p-hydroxy-benzaldehyde from (Aldrich) was used without crystallization. 4-hydroxy-3-methoxybenzaldehyde (vanillin) from EL-Nassr Chemical Company (Egypt) was used as it is. Dihaloalkanes (Aldrich) were used without purification. All solvents and other reagents were of high purity and were further purified by standard methods [12].

2.3. Monomers syntheses

2.3.1. Synthesis of 4,4’-bis(2”-aminothiazol-4”-yl)diphenyl ether X

A mixture of 1 gm ($3.09\cdot10^{-3}$ mole) of 4,4’-bis(chloroacetyl)diphenyl ether **IX**; and 0.47 gm ($6.18\cdot10^{-3}$ mole) of thiourea in 20 ml absolute ethanol was refluxed for 4 hours. The clear solution was poured onto cold sodium acetate solution and the precipitated product was collected by filtration and crystallized from ethyl acetate as yellowish crystals, m.p 240°C, and yield 87%.

Anal. Calc. for $C_{18}H_{14}N_4OS_2$:
C, 59.01; H, 3.82; N, 15.30; S, 17.48.
Found: C, 58.95; H, 3.86; N, 15.13; S, 17.59.

2.3.2. Preparation of 4,4’-diformyl-α,ω-diphenoxyalkanes I–IV and 4,4’-diformyl-2,2’dimethoxy-α,ω-diphenoxyalkanes V–VIII

The title compounds were prepared as described previously in the literature [13], and also as described in our previous papers [14, 15].

2.4. Synthesis of model compound – (2”-methylideneamino-thiazol-4”-yl)-diphenyl ether XI

Model compound was synthesized by refluxing a mixture of monomer **X** ($2.73\cdot10^{-3}$ mole) and benzaldehyde ($4.6\cdot10^{-3}$ mole) in about 20–25 ml of absolute ethanol in the presence of few drops of piperidine as a catalyst for 6 hours. The precipitated product was collected by filtration as yellow crystals and recrystallized from ethanol, m.p 158°C, and yield 85%.

Anal. Calc. for $C_{32}H_{22}N_4OS_2$:
C, 70.84; H, 4.05; N, 10.33; S, 11.80.
Found: C, 70.90; H, 3.98; N, 10.39; S, 11.76.

2.5. Polymerization

General procedures

A typical example of the polycondensation for poly (azomethine-ether)s $\mathbf{XII}_{a–e}$ and $\mathbf{XIII}_{a–e}$ is now described:

In a three necked flask equipped with a condenser, dry nitrogen inlet, outlet, and dropping funnel, a mixture of ($2\cdot10^{-3}$ mole) bis(2-aminothiazole) monomer **X** suspended in 20–30 ml absolute ethanol and a few drops of piperidine was introduced as a basic catalyst. The different prepared bis-aldehydes ($2\cdot10^{-3}$ mole) was dissolved in 15 ml of absolute ethanol was added in dropwise manner at 25°C, during the stirring in about 20 minutes. After complete the addition of bis-aldehydes, the stirring was continued for 12–15 hrs. at ~80°C, during this time, the viscosity of the solution increased rapidly and the polymer began to precipitate in the early stages of the reaction. The polymer precipitated was isolated by filtration as a highly yellowish solid polymers, then washed with hot methanol and hot acetone and then dried under reduced pressure (1 mm/Hg) at 80°C for 48 hours.

All the poly(azomethine-ether)s were synthesized by an analogous procedure. Their yields, inherent viscosities, and elemental analyses are listed in Table 1.

3. Results and discussion

3.1. Monomer synthesis

A new series of thermotropic liquid crystalline poly(azomethine-ether)s based on thiazole moiety were synthesized. The monomer compound **X** was synthesized by the interaction of 4,4’-bis(chloroacetyl)diphenyl ether **IX** with thiourea in absolute ethanol, most probably according to the following known mechanism [16], which is based on the interaction of enol form of the diketone with the mercapto form of thiourea through elimination of H_2O and HCl molecules from the reactants, as shown in Figure 1.

Table 1. Elemental analyses, yields and inherent viscosity of poly(azomethine-ether)s $\mathbf{XII}_{a–e}$ and $\mathbf{XIII}_{a–e}$

Polymer number	Yield [%]	η^*_{inh} [dl/g]	Molecular formula [mol.Wt.]	Elemental analyses				
					C [%]	H [%]	N [%]	S [%]
XII$_a$	72	0.61	$C_{34}H_{24}N_4O_3S_2$	Calcd	68.00	4.00	9.33	10.66
			(600)	Found	67.22	3.66	9.56	10.22
b	87	0.49	$C_{36}H_{28}N_4O_3S_2$	Calcd	68.78	4.45	8.91	10.19
			(628)	Found	67.83	4.70	8.60	9.92
c	91	0.53	$C_{38}H_{32}N_4O_3S_2$	Calcd	69.51	4.87	8.53	9.75
			(656)	Found	68.08	4.34	8.19	9.29
d	75	0.95	$C_{40}H_{36}N_4O_3S_2$	Calcd	70.17	5.26	8.18	9.35
			(684)	Found	68.99	4.88	7.89	9.55
e	85	0.85	$C_{42}H_{40}N_4O_3S_2$	Calcd	70.78	5.61	7.86	8.98
			(712)	Found	69.77	5.28	7.38	8.61
XIII$_a$	79	0.81	$C_{36}H_{28}N_4O_5S_2$	Calcd	65.45	4.24	8.48	9.69
			(660)	Found	63.88	3.94	8.40	9.55
b	84	0.65	$C_{38}H_{32}N_4O_5S_2$	Calcd	66.27	4.65	8.13	9.30
			(688)	Found	65.09	4.92	7.96	9.22
c	93	1.21	$C_{40}H_{36}N_4O_5S_2$	Calcd	67.03	5.02	7.82	8.93
			(716)	Found	65.79	4.67	7.66	9.04
d	78	0.79	$C_{42}H_{40}N_4O_5S_2$	Calcd	67.74	5.37	7.52	8.60
			(744)	Found	66.33	4.97	7.17	8.43
e	90	1.19	$C_{44}H_{44}N_4O_5S_2$	Calcd	68.39	5.69	7.25	8.29
			(772)	Found	67.46	5.11	7.55	8.13

*Measured in H_2SO_4 , with C = 0.5 g/100 ml at 30°C

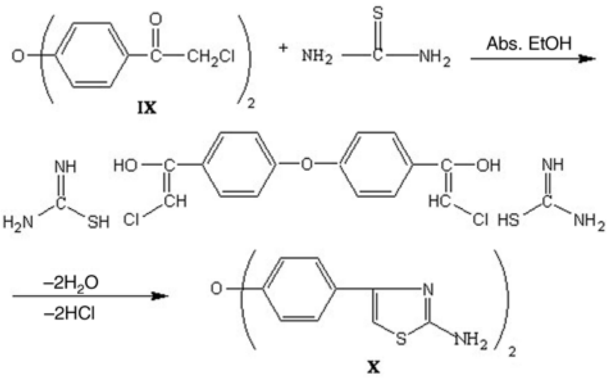

Figure 1. Synthesis of monomer **X**

Elucidation of the structure o monomer **X** was based on correct elemental and spectral data. The IR spectrum displayed characteristic absorption bands at 3400–3290 cm^{-1} due to primary amino group and absorption band at 1625 cm^{-1} due to C=N. The ^{1}H-NMR spectrum (in DMSO-d_6, ppm) showed the following δ values: at 7.8–6.95 (m, 8H of aromatic and 2–CH–S) and at 6.97 (s, 4H of primary amino group, interfered with the aromatic protons and exchangeable with D_2O). The mass spectrum exhibited a molecular ion peak at m/z = 365.80 (100%) which is in agreement with its molecular formula ($C_{18}H_{14}N_4OS_2$). Other peaks were observed at m/z = 333.80 ($M^+ - 2NH_2$, 0.4%); at m/z = 267.77 ($M^+ - C_3H_3N_2S$, 19.1%) and at m/z = 167.86 ($M^+ - C_6H_6N_4S_2$, 0.4%).

3.2. Synthesis of model compound

Before attempting polymerization, model compound **XI** for the desired poly(azomethine-ether)s was synthesized by the interaction of 1 mole of monomer **X** with 2 moles of benzaldehyle in absolute ethanol ad in the presence of few drops of piperidine as a basic catalyst [17] as described in Figure 2.

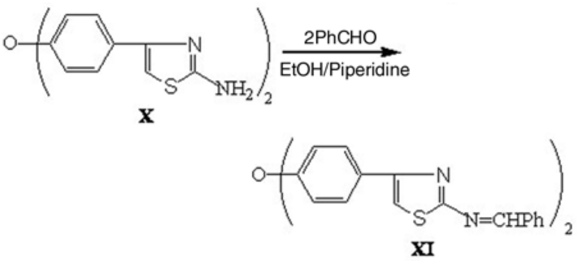

Figure 2. Synthesis of Model Compound **XI**

The structure of model compound **XI** was confirmed by both correct elemental and spectral analyses. The IR spectrum showed the disappearance of NH_2 vibration at 3400–3290 cm^{-1} and gave characteristic absorption bands at 1596 cm^{-1} due to C=N. The ^{1}H-NMR spectrum (in T.F.A., ppm) showed the following values: at 8.01–7.01 (m, 18H of aromatic protons), and at 9.56 (s, 2H oh the –S–CH=). While, the mass spectrum of model compound **XI** exhibited a molecular ion peak at m/z = 542 (0.2%) which is in agreement with its molecular formula ($C_{32}H_{22}N_4OS_2$). Other peaks were in accordance with the proposed structure.

3.3. Synthesis of poly(azomethine-ether)s

A new homologous series of thermotropic liquid crystalline poly(azomethine-ether)s based on thiazole moiety **XII**$_{a-e}$; **XIII**$_{a-e}$ were synthesized in high yields by solution polycondensation of bis(2-aminothiazole) monomer **X** with two series of diformyl-α,ω-diphenoxyalkanes **I–VIII** This method was used for the preparation of conjugated polyazomethine arylidene polymers [18] and liquid crystalline poly (azomethine-ethert)s [19] as published in our previous work. The expected structures of the resulting poly(azomethine – ether)s **XII**$_{a-e}$ and **XIII**$_{a-e}$ were confirmed by elemental and spectral analyses. Results for the properties of the polymers

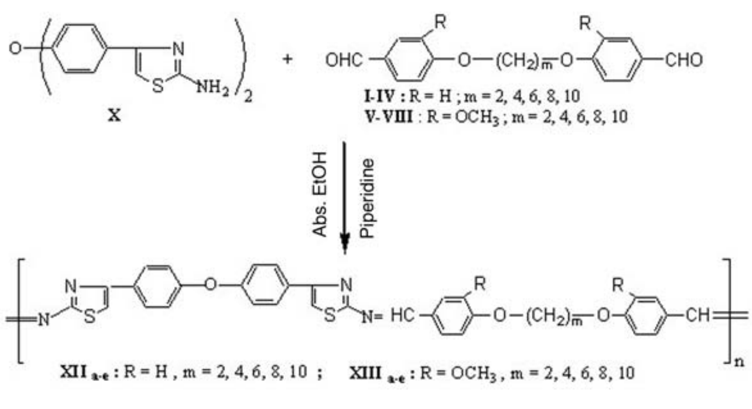

Figure 3. Synthesis of poly(azomethine-ether)s **XII**$_{a-e}$; **XIII**$_{a-e}$

are listed in Table 1. The direct polycondensation easily affords high to moderate molecular mass polymers in quantitative yields. The monomers used and the polymers are depicted in Figure 3.

As mentioned in our previous work [18], the first successful synthesis of high molecular mass, wholly aromatic polyazomethines by the solution polycondensation technique, was that reported by Suematsu *et al.* [3]. This was followed by the work of Saegura *et al.* [20] who synthesized a series of polyazomethines containing heterocyclic moieties. Both groups used m-cresol as a solvent. Li and Chang [11] prepared a series of poly(azomethione-ether)s in a mixture of m-cresol and o-chlorophenol at room temperature. In this work, m-cresol and o-chlorophenol were not the solvents of choice, not only because it was difficult to remove water during the polymerization, but also because the heterogeneity of the reaction medium might have resulted in the formation of the low molecular mass polymers. Experimentation led us to believe that ethanol was a better solvent fore this purpose, because the poly(azomethine-ether)s with inherent viscosities up to 0.71 dl/g were readily obtained in high yield after a few minutes. The polycondensation results are summarized in Table 1. It should be noted that the analyses of the polymers deviated bym 1.2 to 1.5% from the theoretical values. However, it is not uncommon for the polymers to trap solvent molecules within the polymer matrix, especially polymers of high molecular weight [21]. Spectral data support the structural assignment for the resulting poly(azomethine-ether)s and the IR data from KBr disks for all the polymers showed characteristic absorption due to CH stretching of CH_2 groups (aliphatic spacers) at 2940–2860 cm^{-1}, CH=N (azomethine) groups at 1620–1595 cm^{-1}; phenylene rings at 1590–1510 cm^{-1} and C–O–C bonds (ether linkage) at 1240–1270 cm^{-1}.

3.4. Polymer characterization

3.4.1. Solubility

The solubility characteristics of the poly(azomethie-ether)s $\mathbf{XII_{a-e}}$ and $\mathbf{XIII_{a-e}}$ were tested using various solvents including DMF (dimethylformamide), DMSO (dimethylsulfoxide), DMA (dimethylacetamide) THF (tetrahydrofuran), chloroform-acetone (1:1), methylene chloride, formic acid and conc. H_2SO_4. A 5% (w/v) solution was taken as a criterion for solubility. It can be clarified from Table 2 that all the poly (azomethine-ether)s are freely soluble in protonic acids like formic and H_2SO_4 acids. In common organic solvents and halogenated hydrocarbons all polymers are insoluble. In polar aprotic solvents, such as DMF, DMSO, DMA and THF, the majority of the polymers showed partial solubility (except, polymers $\mathbf{XIII_{b-e}}$ are dissolved easily). Comparing the solubility of polymers derived from 4,4’-diformyl-α,ω-diphenoxyalkanes (polymers $\mathbf{XII_{a-e}}$) with those derived from 4,4’-diformyl-2,2’dimethoxy-α,ω-diphenoxyalkanes (polymers $\mathbf{XIII_{a-e}}$), we found that the latter possesses better solubility than the former due to the presence of OCH_3 groups with high steric effect as compared to those containing H atoms which make the solution easier. More particularly, presence of thiazole moiety in the polymer backbone leads to increasing chain packing distances and decreasing inter-chain interactions such as hydrogen bon ding so that making solution

Table 2. Solubility characteristics of poly(azomethine-ether)s $\mathbf{XII_{a-e}}$ and $\mathbf{XIII_{a-e}}$

Polymer number	DMF	DMSO	DMA	THF	Chloroform + Acetone (1:1)	CH_2Cl_2	HCOOH	Conc H_2SO_4
$\mathbf{XII_a}$	+	+	+	+	–	–	++	++
b	+	+	+	+	–	–	++	++
c	+	+	+	+	–	–	++	++
d	+	+	+	+	–	–	++	++
e	+	+	+	+	+	+	++	++
$\mathbf{XIII_a}$	+	++	++	+	–	+	++	++
b	++	++	++	+	–	+	++	++
c	++	++	++	++	–	+	++	++
d	++	++	++	++	+	+	++	++
e	++	++	++	++	+	+	++	++

++: Soluble at room temperature (RT)
+: Partialy soluble at (RT)
–: Insoluble

somewhat easier than other poly(azomethine)s [22].

3.4.2. Inherent viscosity

The inherent viscosities (η_{inh}) of all poly(azomethine-ether)s **$XII_{a–e}$** and **$XIII_{a–e}$** were determined in concentrated sulphuric acid (9 M) at 30°C with a Ubbelohde Suspended Level Viscometer. The inherent viscosity value is defined as Equation (1):

$$\eta_{inh} = \frac{2.3}{C}\log\frac{\eta}{\eta_0} \tag{1}$$

The solution concentration C is 0.5 g/100 ml, η/η_0 = relative viscosity (or viscosity ratio). The data are listed in Table 1. It can be clarified from this table that polymers **$XII_{c,e}$** have high viscosity values (1.21, 1.19 dl/g) and this may be attributed to high molecular weight of these two polymers. On the other hand, polymers **$XII_{a–c}$** have low viscosities (0.61, 0.49 and 0.53 dl/g respectively), and this may be attributed to low molecular weight of these polymers. It should be noted also that the inherent viscosity of polymer **XII_c** (as a example) in concentrated sulphuric acid (9 M) at 30°C decreased to around 2% during 4 days and then remained practically constant as shown in Figure 4, thus indicating the formation of a stable solution [23].

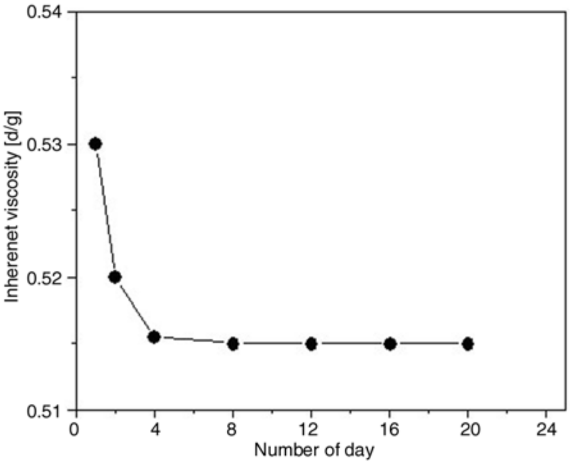

Figure 4. Stability of poly(azomethine – ether) **XII_c** in H_2SO_4 at 30°C

3.4.3. X-ray measurements

The X-ray diffractograms of selected examples of the poly(azomethine-ether)s **$XII_{b,d,e}$** and **$XIII_{b,d,e}$** are shown in Figures 5, 6. The polymers show many reflection peaks that are ranging in crystalline phase lying in region 2θ = 5–60°. This indicates that there is a large class of structures that are intermediate in the ordered states between crystalline and amorphous phases (with pronounced long-range order) in the arrangement of their atoms

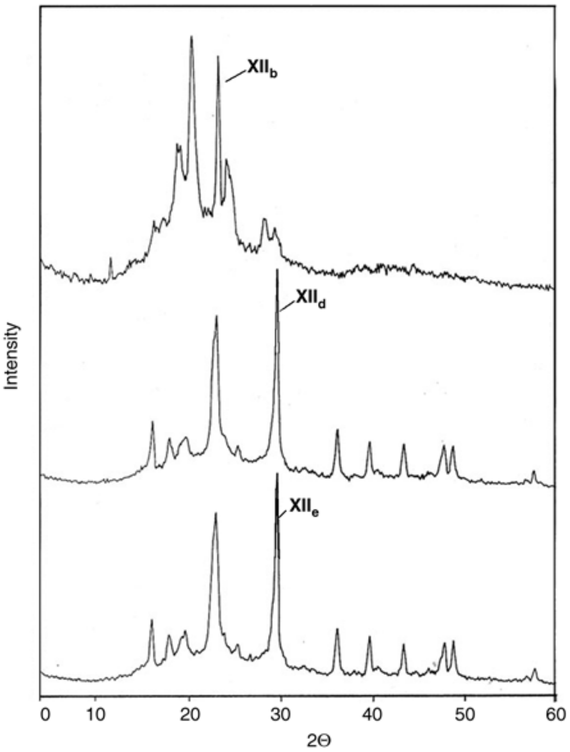

Figure 5. X-ray diffraction patterns of polymers **$XII_{b,d,e}$**

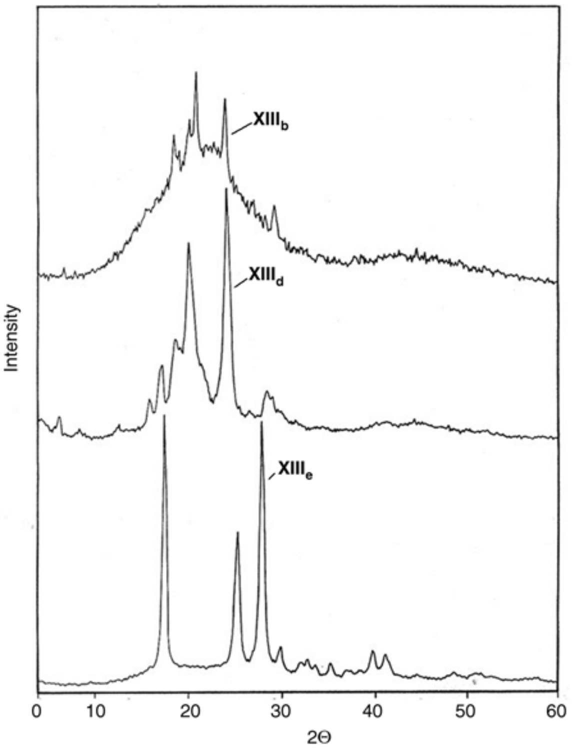

Figure 6. X-ray diffraction patterns of polymers **$XIII_{b,d,e}$**

and molecules. Moreover, the presence of C=N as polar groups provides some order between two extent of crystallinity [24]. More particularly, the diffractograms of polymers **XII$_b$**, **XIII$_b$** which contains short spacer –$(CH_2)_4$– shows few sharp reflection peaks (i.e. show semicrystalline characteristics). When the length of spacer increases, as in polymers **XII$_{d,e}$**, **XIII$_{d,e}$** which contain eight or ten methylene groups –$(CH_2)_8$– or –$(CH_2)_{10}$–, the reflection sharpness increased and the polymer became crystalline. This is explained by the fact that increasing the number of methylene groups in the spacers results in increasing polymer chain flexibility [25], and hence increases crystallinity.

In addition, it was found that the absence of the bulky methoxy substituent in polymers **XII$_{b,d,e}$** and the presence of a hydrogen atom instead showed a tendency to higher crystallinity than in polymers **XIII$_{b,d,e}$** which contain methoxy substituent, where the presence of methoxy group as substituent in the phenyl ring caused some hindrance between the repeating units and forced it to unsymmetrical orientation in the polymer chains and reduced the closely packed structure i.e. crystallinity [26].

3.4.4. Morphological features

The morphology of the synthesized polymers was examined by scanning electron microscopy (SEM). The samples were prepared by putting a smooth part of polymer powder on a copper holder and subsequently coating it with gold palladium alloy. SEM images were taken on a penta Z Z-50 P Camera with Ilford film at an accelerating voltage of 15 kV using a low-dose technique [27]. The study of selected polymers showed that the surface of polymer **XII$_a$** (Figure 7a, magnification X = 1000) consisted of porous particles, with higher magnification showed cavity shape (Figure 7b, X = 2000) while magnification of X = 3500 (Figure 7c) showed more porous particles with globular grains. However, the surface of polymer **XIII$_c$** (magnification X = 1500) showed coral-like particles, with higher magnifications (X = 3500) showed spongy shape.

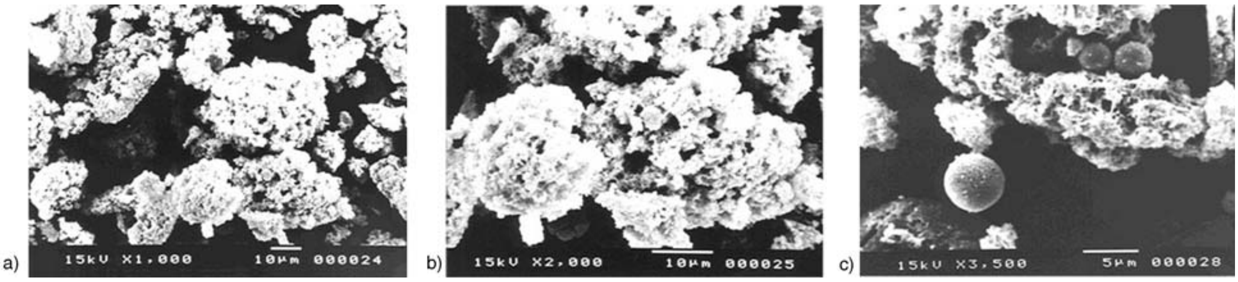

Figure 7. SEM images of polymer **XII$_a$** surface at different magnifications, a) X = 1000; b) X = 2000 and c) X = 3500

3.5. Thermotropic liquid crystal properties of poly(azomethine-ether)s XII$_{a-e}$ and XIII$_{a-e}$

The thermal properties of the poly(azomethine-ether)s **XII$_{a–e}$** and **XIII$_{a–e}$** were characterized by DSC, TGA and by optical polarized microscope (OPM) with heating stage. The poly(azomethine-ether)s **XII$_{a–e}$** and **XIII$_{a–e}$** exhibit threaded-schlieren texture of nematic and good spheroid texture during polarized microscope observation. The phase transition temperatures of the polymers are shown in Table 3. The microscopic observations by OPM allowed detection of the beginning of the melting process and the subsequent transition to the fully isotropic liquid, while the DSC measurements give the temperatures determined at the endothermal maxima [28]. The isotropization temperatures of these polymers was observed by using an optical polarizing microscope equipped with a heating stage in the temperature range of 163–280°C for the polymers **XII$_{a–e}$** and **XIII$_{c–e}$**.

3.5.1. DSC analyses

In DSC studies, most of the polymers revealed multiple or more endothermic peaks on DSC thermograms, probably due to polymorphism [29]. In some cases, the peaks in DSC are broad, especially in polymers **XII$_{a,b,c}$** and **XIII$_c$**, exhibiting thermal decomposition. For this reason, isotropization temperatures of the polymes were identified by observing the textures of the melts on a cross-polarizing microscope. All the poly(azomethine-ether)s were characterized by DSC (except **XII$_e$** and **XIII$_{a,b}$**) and conducted at a heating and cooling rate 10°C min^{-1}. The heating traces of the polymers dis-

Table 3. Transition behavior of poly(azomethine -ether)s $\mathbf{XII_{a–e}}$ and $\mathbf{XIII_{a–e}}$

Polymer number	m	x	Stirred opalescence	Phase transition temperatures [°C, microscope]*			Phase transition temperatures [°C, DSC]		
				T_m	T_i	ΔT	T_m	T_i	ΔT
$\mathbf{XII_a}$	2	H	Strong	227	280	53	224	288	64
$_{\mathbf{b}}$	4	H	Strong	219	270	51	213	280	67
$_{\mathbf{c}}$	6	H	Strong	179	257	78	180	268	88
$_{\mathbf{d}}$	8	H	Strong	172	216	30	178	228	50
$_{\mathbf{e}}$	10	H	Strong	153	166	13	–	–	–
$\mathbf{XIII_a}$	2	OCH_3	None	–	–	–	–	–	–
$_{\mathbf{b}}$	4	OCH_3	None	–	–	–	–	–	–
$_{\mathbf{c}}$	6	OCH_3	Strong	175	195	20	184	215	31
$_{\mathbf{d}}$	8	OCH_3	Strong	169	182	13	175	204	29
$_{\mathbf{e}}$	10	OCH_3	Strong	147	163	16	166	188	22

*Measured by a polarizing microscope equipped with a heating stage

play a glass-transition (T_g), which is weak in the case of polymer $\mathbf{XII_c}$ shows the DSC profiles of the melting process of sample $\mathbf{XII_c}$ that revealed multiple endotherms at 117°C (T_g), 180°C (T_m), 268°C (T_i) and 371°C, probably also indicating decomposition. When the sample was cooled after preheating to 440°C, there were no endothermal or exothermal peaks. Figure 8 shows the DSC profiles of the melting process of sample $\mathbf{XII_d}$ that revealed multiple endotherms at 150°C (T_g),178°C (T_m), 228°C (T_i) and 349°C, also probably with decomposition. When the sample was cooled after preheating to 460°C, there were no endothermal or exothermal peaks. This effect might be due to solid-to-solid (T_{ss}), solid-to-mesophse (T_m) and mesophase-to-solid (T_i) [30] transitions which are observed by an optical microscope.

It should noted that, the phase transition temperature for polymers $\mathbf{XII_c}$ and $\mathbf{XII_d}$ respectively (see Figure 3), are very close to the temperature of the phase transitions observed by microscopy. The little difference between temperatures (not more than 12°C) may be attributed to the observing of the temperatures during the raising in the microscopy [2, 31]. The effect of spacer length on the thermal properties of poly(azomethine-ether)s $\mathbf{XII_{a–e}}$ and $\mathbf{XIII_{a–e}}$ is shown in Table 3; both melting point and isotropization temperature decreased as the length of the flexible aliphatic spacer in the polymer chain increased. The effect of substituents on the thermal properties of polymers $\mathbf{XII_{a\text{-}e}}$ and $\mathbf{XIII_{a\text{-}e}}$ is also shown in Table 3; both the melting point and isotropization temperature decreased by the introduction of methoxy groups into the polymer main chain [32]. Similar observations were reported in previous work [33]. It is known that substituents can reduce the coplanarity of adjacent mesogenic groups and increase the diameter or decrease the axial ratio of the mesogenic units [34]. Thus, the unsubstituted para-linked poly(azomethine-ether)s is infusible below its decomposition temperature. But fusibility is achieved by the introduction of methoxy group into the mesogenic moiety, which lowers the transition temperatures, but of course; also decreases the orientational interactions thereby decreasing the mesophase stability [11].

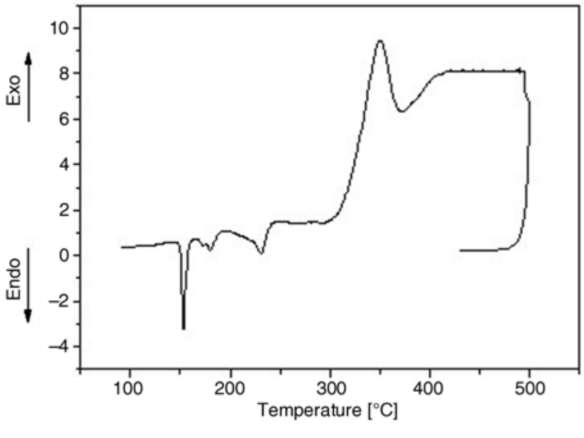

Figure 8. The DSC curve of polymer $\mathbf{XII_d}$

3.5.2. TGA measurements

The thermal behavior of the poly(azomethine-ether)s $\mathbf{XII_{a\text{-}e}}$ and $\mathbf{XIII_{a\text{-}e}}$ was evaluated by TGA and DTG in air at a heating rate of 10°C min^{-1}. TGA curves show a small weight loss in the range 2–4% starting at 160°C until 200°C which may be attributed to loss of observed moisture and entrapped solvents. The thermographs of selected examples from these polymers are given in Figures 9, 10 while Table 4 gives the temperatures for various percentages

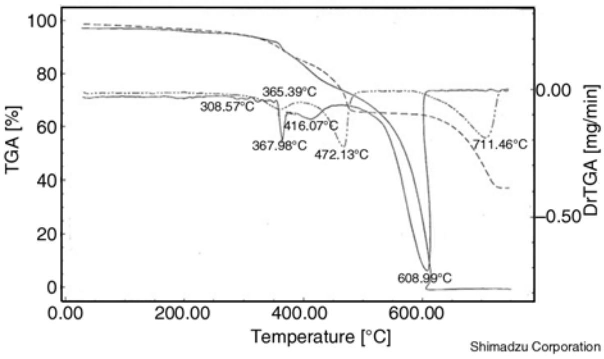

Figure 9. The TGA and DTG traces of polymers **XII$_c$** and **XII$_d$** in air at a heating rate of 10°C/min

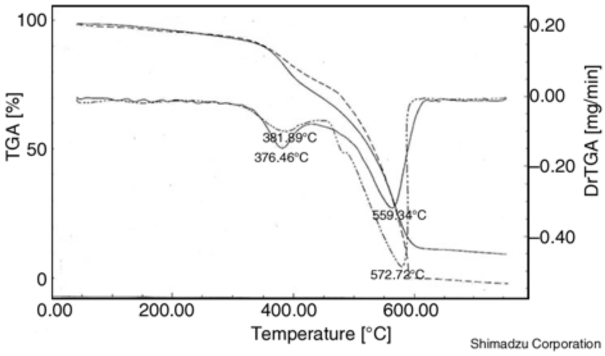

Figure 10. The TGA and DTG traces of polymers **XIII$_c$** and **XIII$_d$** in air at a heating rate of 10°C/min

Table 4. Thermal properties of poly(azomethin-ether)s **XII$_{b–e}$** and **XIII$_{c–e}$**

Polymer number	Temperature [°C] for various % decomposition*				
	10	**20**	**30**	**40**	**50**
XII$_b$	378	409	460	487	513
c	378	436	516	553	582
d	368	450	478	656	690
e	387	427	509	541	562
XIII$_c$	360	400	454	497	530
d	363	420	477	508	536
e	370	424	498	533	556

*The values were determined by TGA at heating rate of 10°C/min

weight loss. The initial decomposition of these polymers (5% loss) started at 312°C for series **XII$_{a-e}$** and at 295°C for series **XIII$_{a–e}$**. All the polymers showed similar decomposition patterns in two steps except polymers **XII$_{b–d}$** which occurs in three steps. The first step is slow and ranges between 249 and 443°C; the second step is a fast degradation and ranges between 456 and 645°C the extended nature of the decomposition of these polymers is through pyrolytic oxidation C=N and rupture of many bonds. The degradation becomes maximal at around 550°C and is nearly complete at around 720°C. The temperature for 10% weight loss is considered to be the polymer decomposition temperature [25, 35] (PDT); it occurs in the range 360–387°C for all the polymers. In Figures 9, 10 mass loss is seen to be rapid between ~340–392°C for polymer **XII$_c$** in the first region, between ~395–473°C in the second region and between ~475–664°C in the third region. For polymer **XII$_d$**, the mass loss was rapid between ~259–396°C in the first region, between ~400–530°C in the second region and between ~535–720°C in the third region. For polymer **XIII$_c$**, the mass loss was rapid between ~279–410°C in the first region, between ~413–709°C in the second region. For polymer **XIII$_d$**, the mass loss was rapid between ~268–409°C in the first region, between ~415–607°C in the second region.

It should be noted that, the behavior of all polymers in the first region was nearly identical. The expected nature of decomposition of this type of polymer is a pyrolytic oxidation of C=N, scission of many bonds, in addition to the formation of char as an end product [15]. Polymers **XII$_{a–e}$** containing no methoxy substituent in the main chain is somewhat higher in thermal stability than polymers **XIII$_{a–e}$**. All the synthesized polymers exhibit higher thermal stability than other similar poly(azomethine-ether)s, which may be attributed to the presence of thiazole moiety in the polymers main chain.

3.5.3. Texture observation

To support further the information gained by DSC on the thermotropic behavior of the synthesized polymers, qualitative observation of the textures between crossed polarizers was carried out for poly(azomethine-ether)s **XII$_{a–e}$** and **XIII$_{a–e}$**. Optical microscopy showed that all the polymers melt yield viscous, birefringent liquid crystal phases except polymers **XIII$_{a,b}$**, which did not show any birefringence, so providing direct evidence for lack of mesomorphic behavior for these polymers. The temperatures correspond roughly with those observed by DSC; differences may be due to variations in heating rates. The character of the texture at a given temperature was fixed by quenching it in liquid nitrogen. Micrographs were then obtained on heating to room temperature (not shown). Observation of poly(azomethine-ether) **XII$_b$** under a polarizing microscope revealed that this polymer exhibited a threaded-schlieren texture of nematic

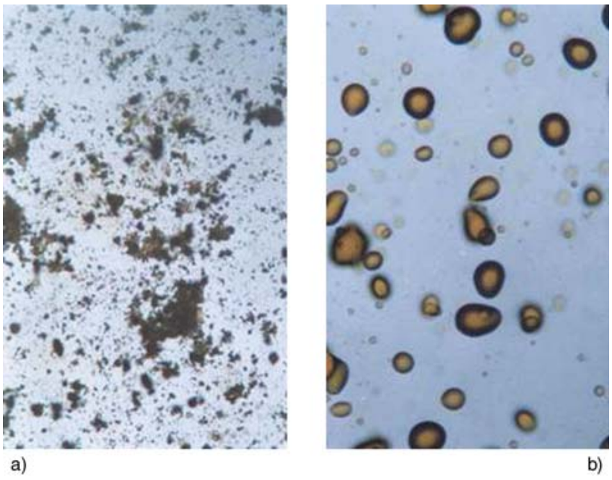

Figure 11. Photomicrographs of polymer $\mathbf{XII_b}$ in the heating cycle at (a) 219°C, (b) 270°C (Magnification $X = 200$)

phase with a thick dark rim in Figure 11a (before melting), and the mesophase extend up to the isotropic at 270°C (T_i). After cooling to room temperature a highly spheroidal texture appeared (c.f. Figure 11b).Observation of poly(azomethine-ether) $\mathbf{XII_c}$ in the anisotropic melt displayed the typical schlieren textures as shown in (before melting), and at 257°C (T_i).

In addition to, observation of poly(azomethine-ether) $\mathbf{XIII_d}$ under a polarizing microscope revealed that this polymer exhibited a good spheroid structure with a thick dark rim (before melting), and the mesophase extends up to the isotropization temperature at 182°C (T_i). After cooling to room temperature a highly spheroidal texture appeared.

The textures observed were generally grey, although annealing samples for long periods led to the formation of well developed schlieren textures [36].

4. Conclusions

A novel series of thermally stable liquid crystalline poly(azomethine-ether)s containing thiazole moiety have been synthesized. A solution polycondensation technique at ~80°C was used. The majority of the polymers are insoluble in common organic solvents and halogenated hydrocarbons. Most of them exhibited melt birefringence and stirred opalescence during polarized microscope observation.

Both (T_m) and (T_i) values increased as the length of the flexible aliphatic spacers increased and decreased with introduction of the methoxy group as a substituent in the polymers main chain.

Acknowledgements

It is pleasure to acknowledgement Dr. M. Abd El-Moniem at Geology Department, Faculty of Science, Assiut University for his assistance in the Optical properties measurements.

References

[1] Janneli P., Roviello A., Sirigu A.: Liquid crystal behavior of linear copolymers I. European Polymer Journal, **18**, 745–751 (1982).

[2] Sek D.: Liquid crystalline properties of new poly (azomethine esters). European Polymer Journal, **20**, 923–926 (1984).

[3] Suematsu K., Nakamurra K., Takeda J.: Synthesis of aromatic polyimines by the condensation of aromatic dialdehyde and diamine. Colloid and Polymer Science, **261**, 493–501 (1983).

[4] Sek D.: Synthesis of polyazomethinesters and relationship between their structures and thermal stability. Polymer Journal, **14**, 173–179 (1982).

[5] Roviello A., Sirigu A.: Mesophasic structures in polymers. A preliminary account on the mesophases of some poly-alkanoate of p,p'-dihydroxy-α, α'-dimethyl benzalazin. Journal of Polymer Science: Polymer Letters Edition, **13**, 455–463 (1975).

[6] Ober C. K., Jin J. I., Lenz R. W.: Liquid crystal polymer I. Springer-Verlag, Berlin (1984).

[7] Chapoy L. L: Recent advances in liquid crystalline polymers. Elsevier, London (1986).

[8] Morgan P. W., Kwolek S. L., Pletcher T. C.: Aromatic azomethine polymers and fibers. Macromolecules, **20**, 729–739 (1987).

[9] Guillon D., Skoulion A.: Mesophases smectiques thermotropes de polybases de Schiff. Molecular Crystals and Liquid Crystals, **49**, 119–123 (1978).

[10] Wojtkowski P. W.: Aromatic-aliphatic azomethine ether. Polymers and fibers. Macromolecules, **20**, 740–749 (1987).

[11] Li C-H., Chang T-C.: Studies on thermotropic liquid crystalline polymers-part II. Synthesis and properties of poly(azomethine-ether). European Polymer Journal, **27**, 35–39 (1991).

[12] Perrin D. D., Armarigo W. L. F., Perrin D. F.: Purification of laboratory chemicals. Pergamon, New York (1980).

[13] Liang A. L., Hsu K. Y., Li C. H., Chang T. C.: Studies on thermotropic liquid crystalline polymers: 4. Synthesis and properties of poly (ether ester amide)s. Polymer, **33**, 2217–2221 (1992).

[14] Aly K. I.: Liquid crystalline polymers: 2. synthesis and thermotropic studies of poly (arylidene-ether)s containing cyclo pentanone moiety in the main chain. High Performance Polymers, **11**, 437–452 (1999).

[15] Aly K.I.: Liquid crystalline polymers: 3. Synthesis and liquid crystal properties of thrmotropic poly(arylidene-ether)s and copolymers containing cycloalkanone moiety in the polymer backbone. Journal of

Macromolecular Science, Part A: Pure and Applied Chemistry, **37**, 93–115, (2000).

[16] Joule J. A., Smith G. G.: Heterocyclic chemistry. Blackvell Science, Oxford (2000).

[17] Patai S.: Chemistry of carbonyl group, Jonathan Grobe Books, Deep River (1966).

[18] Aly. K. I., Khalaf A. A.: New polymer syntheses IX. Synthesis and properties of new conducting polyazomethine polymers containing main chain cycloalkanone and pyridine moieties. Journal of applied polymer science, **77**, 1218–1229 (2000).

[19] Aly K. I., Ahmed R. A.: Liquid crystalline polymers V. Thermotropic liquid crystalline poly(azomethine-ether)s containing cycloalkanone moiety in the polymer backbone. Liquid Crystals, **27**, 451–458 (2000).

[20] Saegura Y., Koshikawa T., Nakamura S.: Synthesis and characterization of 1,3,4-oxadiazole-containing polyazomethines. Journal of Polymer Science: Polymer Chemistry, **30**, 1369–1373 (1992).

[21] Andrew S. M., Bass R. G.: Polypyrazolinones from aromatic di(propynoic ester)s and aromatic dihydrazines. Journal of Polymer Science Part A: Polymer Chemistry, **27**, 1225–1239 (1989).

[22] Hsiao S. H., Liou G. S.: A new class of aromatic poly(1,3,4-oxadiazole)s and poly (amide-1,3,4-oxadiazole)s containing (naphthalene dioxy)diphenylene groups. Polymer Journal, **34**, 917–924 (2002).

[23] Patra S.; Lenka S., Nayak P. L.: Synthetic resins II. Preparation and characterization of resins prepared from aminoacetophenone. Journal of Applied Polymer Science, **32**, 5071–5083 (1986).

[24] Mandelkern L: Crystallization of polymers. McGraw-Hill, New York (1964).

[25] Aly K. I.: New polymer syntheses VIII. Synthesis, characterization and morphology of new unsaturated copolyesters based on dibenzylidene-cycloalkanones. Polymer International, **47**, 483–490 (1998).

[26] Aly K. I.: The synthesis and characteristics of some new polymeric quinone and diarylidene derivatives. Ph.D. Thesis, Assiut University, Egypt 1989.

[27] Tager A.: Physical Chemistry of Polymers. Mir, Moscow (1972).

[28] Aly K. I.: New polymer syntheses III. Synthesis and characterization of new unsaturated polycarbonates. High Performance Polymers, **6**, 149–154 (1994).

[29] Roviello A., Sirigu A.: Poly[oxytetradecanedioyloxy-1,4-phenylene-(2 methylvinylene)-1,4-phenylene]. A polymer showing monotropic mesomorphism. Die Makromolekulare Chemie, **180**, 2543–2545 (2003).

[30] Sato M., Manabf Y., Sasaki T., Ohtomo Y., Komatsu F.: Synthesis and thermal properties of novel thermotropic aromatic – aliphatic homo- and copolyamides. European Polymer Journal, **27**, 1391–1395 (1991).

[31] Sek D.: Synthesis and properties of new poly(azomethinesters). European Polymer Journal, **20**, 805–809 (1984).

[32] Ozcayir Y., Blumstein A.: Diacetylenic liquid-crystalline polymers and copolymers I. Derivatives of diphenyldiacetylene. Journal of Polymer Science: Polymer Chemistry, **24**, 1217–1225 (1986).

[33] Aly K. I., Hammam A. S.: Liquid crystalline polymers I. Main chain thermotropic poly (arylidene-ether)s containing cyclopentanone moiety linked with polymethylene spacers. European Polymer Journal, **36**, 1933–1942 (2000).

[34] Ober C. K., Jin J. I., Lenz R. W.: Liquid Crystal Polymer Springer-Vertag Berlin (1984).

[35] Aly K. I., Abd-Alla A.: Arylidene polymers XX. Synthesis and characterization of some new photochromic heterocyclic arylidene polymers contaning 1,3,4-oxadiazole and 1,2,4- triazole moieties in the main chain. Polymer Journal, **24**, 165–171 (1992).

[36] Demus D., L. Richter: Textures of liquid crystals. Verlag Chemie, Weinheim (1978).

eXPRESS Polymer Letters Vol.1, No.4 (2007) 208–216
Available online at www.expresspolymlett.com
DOI: 10.3144/expresspolymlett.2007.32

Thermal degradation studies of LDPE containing cobalt stearate as pro-oxidant

P. K. Roy[1], *P. Surekha*[1], *C. Rajagopal*[1], *V. Choudhary*[2*]

[1]Centre for Fire, Explosive and Environment Safety, Timarpur, Delhi 110054, India
[2]Centre for Polymer Science and Engineering, I.I.T, Delhi, Hauzkhas, Delhi 110016, India

Received 9 February 2007; accepted in revised form 18 March 2007

Abstract. The influence of a typical prooxidative additive, cobalt stearate, on the thermal stability, degradation kinetics and lifetime of low-density polyethylene (LDPE) was investigated using non-isothermal thermogravimetric analysis (TGA) in both nitrogen and air atmosphere. The derivative thermogravimetric (DTG) curves indicate single stage and multistage decomposition process in nitrogen and air atmosphere respectively. The kinetic parameters of degradation were evaluated using the Flynn-Wall-Ozawa iso-conversion technique. The apparent activation energies for decomposition have been calculated for degradation under nitrogen atmosphere. The lifetime of LDPE (time for 5% mass loss) was estimated to be $8.2\cdot10^{26}$ min in nitrogen and was found to decrease dramatically with increase in the concentration of cobalt stearate thereby revealing its pro-oxidative ability. Studies indicated that the service/process temperature also has a strong influence on the lifetime of all the formulations investigated. The effect of cobalt stearate on the air oven aging behavior of LDPE at two different temperatures (70°C and 100°C) was also investigated to demonstrate the pro-oxidative nature of cobalt stearate.

Keywords: *thermal properties, LDPE, thermogravimetric analysis, thermal stability, kinetics of degradation*

1. Introduction

The last few decades have seen a tremendous increase in the use of polyethylene, particularly in the agriculture and packaging sectors. This has resulted in its increased production and associated plastic litter problem as polyethylene in its pure form is extremely resistant to environmental degradation. It has been estimated that polyethylene would degrade less than 0.5% in 100 years, and 1% if exposed to sunlight for 2 years before biodegradation [1]. An excellent way to render polyethylene degradable is to blend it with pro-oxidant additives, which can effectively enhance the degradability of these materials. Common pro-oxidants include transition metal salts with higher fatty acids, cobalt stearate being a typical example. We have reported in our previous studies that polyethylene containing cobalt carboxylates exhibit a higher susceptibility to both photo as well as thermo-oxidative degradation [2–5]. However, the effect of pro-oxidant on the lifetime of polymer by non-isothermal thermogravimetry has not been investigated previously. The incorporation of these additives is expected to decrease the lifetime of polyethylene in general.

The kinetics of degradation can generate parameters, which can be subsequently used to deduce the lifetime of polymers at different temperatures. The thermal decomposition of linear polyethylene has been reported to occur via random chain scission yielding little or no monomer but many small fragments [6]. However, LDPE contains short butyl branches, which can act as weak links causing initiation to occur adjacent to these sites. It is almost impossible to obtain the exact kinetic parameters for each reaction involved in the polymer decom-

---

[*] Corresponding author, e-mail: veenach@hotmail.com

© BME-PT and GTE

position and apparent kinetic parameters are often used to represent the behaviour of polymer decomposition in general [7]. Actually these parameters rather represent the overall weight loss behaviour during the polymer thermal decomposition as a function of temperature.

This study is concerned with the degradation behaviour of a series of formulations containing cobalt stearate in the concentration range (0.05–0.2% *w/w*) using non-isothermal thermogravimetric analysis in two different atmospheres: nitrogen and air. The kinetic parameters have been calculated which have been subsequently employed to predict the effect of cobalt stearate on the lifetime of LDPE. Air oven aging studies have also been performed at two different temperatures (70°C and 100°C) to demonstrate practically the pro-oxidant activity of cobalt stearate on LDPE.

2. Experimental

2.1. Materials

Commercial low-density polyethylene (LDPE) (Indothene, 24FS040) was used for the preparation of films. The MFI for the polymer was 3.7 g/10 min at 190°C under 2.16 kg load, with crystalline melting point of 110°C and density of 0.92 g/cm^3. Cobalt acetate, sodium hydroxide and stearic acid (AR grade, E. Merck) were used without further purification. Cobalt stearate was synthesised by double decomposition process according to the procedure reported in the literature [8]. The thermal characterisation and other physico-chemical properties of cobalt stearate have been reported in our previous papers [2–5].

2.2. Film preparation

Films of 70 micron thickness were prepared by mixing varying concentrations (0.05%–0.2% w/w) of cobalt stearate with LDPE using an extruder (Dayal make, Delhi, India) with a 19 mm screw of L:D::22:1, attached to a film blowing unit. A blow up ratio of 5.5:1 was used to prepare films. The temperature in the barrel sections of the extruder was maintained at 120°C and 130°C respectively, and that of the die head section was 135°C.

LDPE film has been designated as F1 and LDPE containing 0.05%, 0.1%, 0.15% and 0.2% of cobalt stearate have been designated as FCS5, FCS10, FCS15 and FCS20 respectively.

2.3. Thermal analysis

The non isothermal thermogravimetric analysis was performed on a Perkin Elmer Diamond Simultaneous TGA-DTA-DSC. The experiments were conducted under flowing atmosphere of nitrogen and air atmosphere at a purge rate of 200 ml/min. The samples were studied in the form of thin films, about 70±1 μm, prepared by film blowing technique. The films were sliced with a razor blade into thin oblong pieces prior to TGA analysis. A quantity of 3.5±0.3 mg was placed in an open alumina sample pan. The sample was then equilibrated to 200°C before being heated to 550°C at different heating rates (3–10°C/min) for TGA analysis. The actual heating rate was calculated from temperature measurements made during the period of polymer decomposition. For DSC analysis, the samples were heated from 50°C to 200°C at 3°C/min.

2.4. Thermo oxidative tests

The thermooxidative tests were carried out by placing the extruded films of F1 and FCS10 in an air oven at two different temperatures (70°C and 100°C) for extended periods as reported in the literature [9]. The changes due to thermo-oxidation were monitored by recording changes in mechanical properties, structure and MFI.

Changes in the mechanical properties i.e. tensile strength and elongation at break were monitored using a Materials strength-testing machine, (JRI-TT25, Delhi, India). Samples with a gauge length of 100 mm and width of 10 mm were cut from the films for tensile strength measurements as per ASTM 882-85. The speed of testing was 100 mm/min. The tests were undertaken in an air-conditioned environment at 20°C and a relative humidity of 65%. Five samples were tested for each experiment and the average value has been reported.

Structural changes upon exposure were investigated using FTIR spectroscopy. Carbonyl Index (CI), as determined from FTIR spectra was used to characterize the extent of degradation in polyethylene. It is defined as the ratio of absorbance of carbonyl band around 1740 cm^{-1} and internal thickness band at 2020 cm^{-1}. These have been calculated by the baseline method.

$$\text{Carbonyl Index (CI)} = \frac{\text{Absorption at } 1740\ \text{cm}^{-1}\ \text{(the maximum of carconyl peak)}}{\text{Absorption at } 2020\ \text{cm}^{-1}\ \text{(internal thickness band)}}$$

The Melt Flow indices of all formulations before and after exposure was measured using MFI (International Equipments, Mumbai) at 190°C according to ASTM D1238. The extrudates were cut at regular intervals of 30 s after application of 2.16 kg of dead weight.

3. Results and discussion

3.1. Thermal stability

The melting point of LDPE, as determined from the peak of the endothermic melting transition in the DSC trace, was observed at ~110°C. It was observed that the melting point remains unaltered even after blending with cobalt stearate.

The thermogravimetric (TG) and derivative thermogravimetric (DTG) traces for FCS10 performed in nitrogen atmosphere at three different heating rates are presented in Figure 1. As is evident from the figure, all the samples exhibit single step decomposition in nitrogen atmosphere over a relatively short temperature range. In inert atmosphere, random scission has been reported to be the primary pathway for degradation in polyethylene [9]. However, this is also accompanied by polymer branching. From the figures, it can be concluded that both, scission as well as branching, occur simultaneously resulting in a single mass loss step. The degradation temperature was found to increase with increase in the heating rate (β), which corresponds to the time temperature superposition principle. A shorter time is required for the sample to reach a given temperature at a faster heating rate. The onset temperature of degradation (T_{onset}), temperature of maximum loss (T_{max}), end temperature of degradation (T_{end}), temperature corresponding to 5% loss (T_{5l}) and 50% loss (T_{50l}) have been calculated from the DTG curves (3°C/min) and are presented in Table 1. It was observed that T_{onset} shifts to lower temperatures with increase in the concentration of cobalt stearate, which also results in larger ΔT (difference of T_{onset} and T_{end}). This also indicates that the degradation require relatively longer time periods.

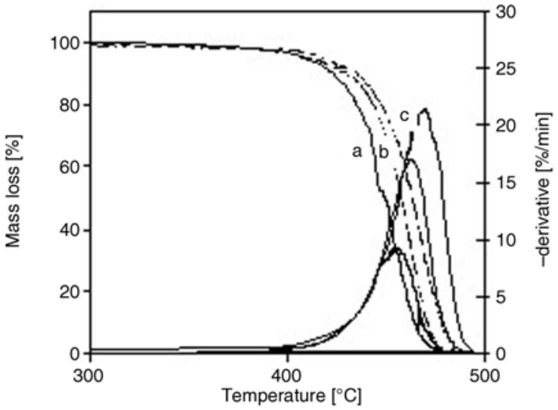

Figure 1. TG/DTG traces for the thermal decomposition of FCS10 in nitrogen atmosphere at different heating rates a) 3°C/min, b) 5°C/min, c) 7°C/min

In air atmosphere, a slight increase in the weight due to heating till 160–200°C, and this has been attributed to the formation of polymeric oxides [9]. In the present investigation, a similar increase was observed in all the samples during the initial equilibration process. The increased weight at 200°C was read as 100% for the subsequent dynamic thermogravimetric investigations. The thermogravimetric (TG) and derivative thermogravimetric (DTG) traces for FCS10 performed in air atmosphere at three different heating rates are presented in Figure 2. Multi step decomposition was observed in air atmosphere. It is apparent that the samples start losing weight from the inception of the experi-

Table 1. Results of TG/DTG traces of films in nitrogen atmosphere and its kinetic degradation parameter

Sample	T_{onset} [°C]	T_{max} [°C]	T_{end} [°C]	T_{5l} [°C]	T_{50l} [°C]	ΔT [°C]	IPDT [°C]	n	lnA
F1	401	456	486	406	449	84	449	0.9	47
FCS5	400	456	486	406	450	85	447	0.9	40
FCS10	400	456	485	405	450	85	447	0.9	15
FCS15	399	456	484	400	452	85	446	0.9	14
FCS20	390	457	482	400	453	92	445	0.9	13

T_{onset}: Onset temperature of degradation, T_{max}: temperature of maximum rate of mass loss, T_{end}: end temperature of degradation, T_{5l}: temperature corresponding to 5% mass loss, T_{50l}: temperature corresponding to 50% mass loss, $\Delta T = T_{end} - T_{onset}$, IPDT: Integral Procedural decomposition temperature; n: order of reaction, A: pre-exponential factor

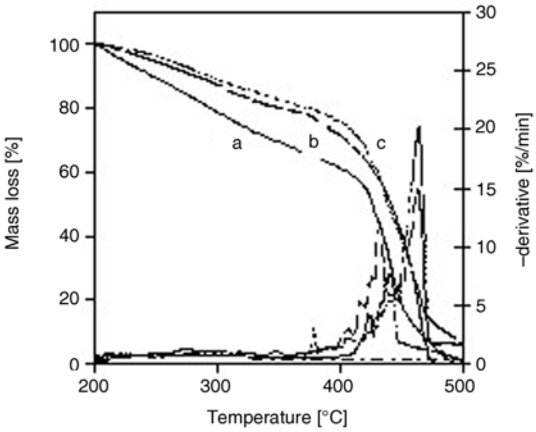

Figure 2. TG/DTG traces for the thermal decomposition of FCS10 in air atmosphere at different heating rates a) 3°C/min, b) 5°C/min, c) 7°C/min

ment after 200°C. It is well known that the degradation of polyethylene in air occurs via reaction with oxygen [10], which results in the degradation becoming exothermic at around ~400°C. This leads to an unsteady degradation process, which does not show any systematic temperature shifts with heating rate and occurs rather randomly at this temperature (~400°C). Contrary to the behavior in nitrogen atmosphere, the degradation temperature was not found to increase with increase in the heating rate (β) in air. Table 2 reports the temperature at which 5% and 50% mass loss occur's as T_{5l} and T_{50l} respectively. On comparing Table 1 and 2, we observe that the degradation occurs at much lower temperatures in air than in nitrogen atmosphere. Addition of cobalt stearate to polyethylene leads to further lowering of these characteristic temperatures, which indicate its pro-oxidative nature.

Integral Procedural Decomposition Temperature (IPDT), which sums up the shape of thermogravimetric curve, was calculated according to the method developed by Doyle [11]. The area under the thermogravimetric trace, from the initial temperature of 200°C to the final temperature (T_f) of 500°C was determined. The ratio of this area to the total area of rectangular plot bounded by the curve gives A^*. The IPDT was obtained by employing the following relationship (1):

$$\text{IPDT} = A^* (T_f - T_i) + T_i \tag{1}$$

where $T_f = 500°\text{C}$ and $T_i = 200°\text{C}$. The IPDT values have been reported in Table 1. The IPDT was found to decrease slightly with increase in the concentration of cobalt stearate.

As the polymers investigated in the present study consist solely of carbon and hydrogen elements, there is minimal residue once the degradation is over.

Table 2. Characteristic temperatures for thermo-oxidative degradation of polyethylene

Sample designation	T_{5l} [°C]	T_{50l} [°C]	IPDT [°C]	lnA
F1	286	426	392	15
FCS5	282	412	390	13
FCS10	252	400	386	10
FCS15	267	400	385	7
FCS20	222	400	380	6

3.2. Kinetic evaluations

3.2.1. Multiple constant heating rates: Flynn-Wall-Ozawa method

The most commonly used approach to determine the apparent kinetic parameters is first to measure the weight loss behaviour during the material decomposition and then to employ the Arrhenius equation (Equation (2)) to fit this data.

$$\frac{\mathrm{d}\alpha}{\mathrm{d}t} = Ae^{-\frac{E_a}{RT}}(1-\alpha)^n \tag{2}$$

where A is the frequency factor, n is the reaction order, E_a is the apparent kinetic energy of the degradation reaction, R is the gas constant, α is the conversion and T is the absolute temperature. In thermogravimetric analysis, the conversion rate of a reaction is defined as the ratio of actual mass loss to the total mass loss corresponding to the degradation process (3):

$$\alpha = \frac{M_0 - M}{M_0 - M_f} \tag{3}$$

where M, M_0 and M_f are the actual, initial and final mass of the sample respectively.

Ozawa, Flynn and coworkers [12, 13] derived a method for the determination of activation energy based on the Equation (4):

$$\log\beta \cong 0.457\left(-\frac{E_a}{RT}\right) + \left[\log\left(\frac{AE_a}{R}\right) - \log F(\alpha) - 2.315\right] \tag{4}$$

where β is the heating rate. Thus, at the same conversion, the activation energy, E_a is obtained from the plot of $\log\beta$ against $1/T$.

3.2.2. Degradation kinetics in nitrogen

Based on Equation (4), the isoconversional graph between logarithm of heating rate (logβ) and $1/T$ for different values of percentage conversion for FCS10 and F1 were plotted and found to be almost parallel straight lines in nitrogen atmosphere. The variation of iso-conversional activation energy with conversion for all the formulations is presented in Figure 3. For neat LDPE, the activation energy increases moderately from 250 to 280 kJmol^{-1} throughout the degradation processes. Similar increase in the activation energy has been observed previously [14]. As has been reported by Peterson *et al.* [14], the observed variation in the activation energy can be attributed to the degradation kinetics being governed by different processes at the initial and final stages, the lower value of the activation energy being associated with the initial process that occur at the weak links. Low-density polyethylene is a branched polymer containing butyl branches, which can act as weak links. As these weak links are consumed, the limiting step of degradation shifts towards the degradation initiated by random scission. This type of degradation requires higher energy. The activation energy 'E_a' as well as frequency factor 'A' were found to decrease significantly with increase in the concentration of cobalt stearate. This indicates that cobalt stearate is capable of catalyzing the degradation process in polyethylene by providing an alternative route for degradation. During processing of polyethylene in the presence of cobalt stearate, certain intermediates may be formed which decompose first requiring a lower activation energy. During the carbonization process, the polymeric structure of polyethylene breaks down, producing smaller intermediate species, which can further react and produce smaller hydrocarbon molecules, liquids and gases [15–18]. However, not every bond broken in the polymer chain leads to the evaporation of the product formed. Only the fragments small enough to evaporate at that temperature actually leave the crucible and balance records a weight loss. Both physical as well as chemical processes influence the rate of change of polymer mass and hence the degradation kinetics [19–20].

3.2.3. Degradation kinetics in air

The thermal degradation process in air is a very complex process and does not exhibit any systematic temperature shifts with heating rate (Figure 2). Degradation in air leads to the formation of several different products including peroxides, acids and alcohols. The initial degradation process (α<0.2) leads to the formation of peroxides and the calculated value of activation energy in this period (~80–90 kJ mol^{-1}) is consistent with the energy associated with decomposition of peroxides [14]. The activation energy of PE becomes erratic thereafter. However, after the conversion reaches 20% the E_a increases and the degradation becomes exothermic at ~400°C. This temperature is consistent with the ignition temperature of many carboxylic acids, which predominate at the later stages of degradation [14]. As a result of this random decomposition phenomenon at ~400°C, the activation energy changes erratically around the extent of conversion related to this temperature region.

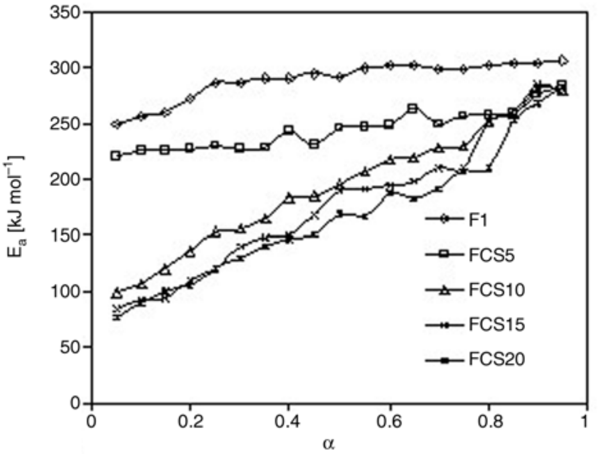

Figure 3. E_a dependencies obtained by iso-conversional analysis of TGA data in nitrogen

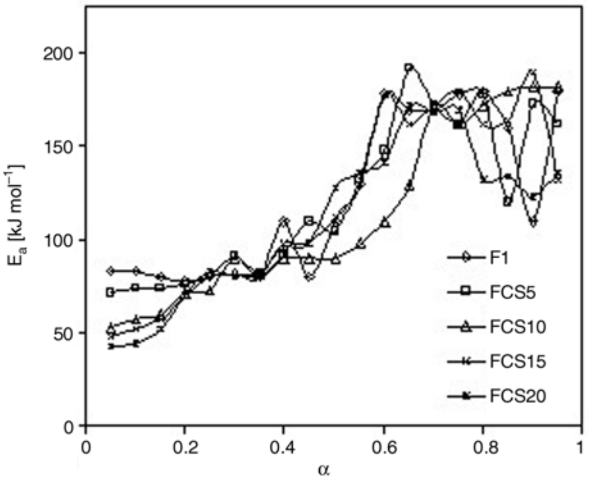

Figure 4. E_a dependencies obtained by iso-conversional analysis of TGA data in air

Therefore the isoconversion plots of $\log\beta$ *versus* $1/T$ in air atmosphere are not parallel as in nitrogen atmosphere. The variation of iso-conversional activation energy with conversion for all the formulations in air atmosphere is presented in Figure 4. The erratic changes in E_a indicate that the multistep decomposition in air is a complex mass loss process involving several different reactions with varied mechanisms. It is apparent that the activation energy 'E_a' as well as frequency factor 'A' is much lesser in air atmosphere than in nitrogen atmosphere. In the presence of cobalt stearate, the E_a decreases and the relative lowering of E_a is dependant on the concentration of additive thereby indicating the prooxidative ability of cobalt stearate.

3.3. Lifetime predictions

Lifetime estimations are very useful in the development or selection of polymers for different applications. The lifetime is usually determined by accelerated aging, like air oven aging studies, which require long time periods. The apparent kinetic parameters calculated from this study have been used to arrive at the lifetime of the formulations. The estimated lifetime of a polymer to failure has been defined as the time when the mass loss reaches 5 wt%, i.e $\alpha = 0.05$ [21–23]. From the integration of Equation (2), the lifetime can be estimated by Equation (5):

$$t_f = \frac{(1-0.95^{1-n})}{A(1-n)} \exp\frac{E_a}{RT} \quad (n \neq 1) \tag{5}$$

or Equation (6):

$$t_f = \frac{0.0513}{A} \exp\frac{E_a}{RT} \quad (n = 1) \tag{6}$$

The reaction order value (n) can be obtained directly from the symmetrical index of a derivative thermogravimetry (DTG) peak based on the second Kissinger technique [23], Equation (7):

$$n = 1.88 \frac{\left|\frac{\mathrm{d}^2\alpha}{\mathrm{d}t^2}\right|_L}{\left|\frac{\mathrm{d}^2\alpha}{\mathrm{d}t^2}\right|_R} \tag{7}$$

where, the indices L and R correspond to the left and right peak ($\mathrm{d}^2\alpha/\mathrm{d}t^2$) values on the second derivative thermogravimetry (DDTG) curve for the decomposition process.

The n and $\ln A$ values for the decomposition in nitrogen atmosphere are listed in Table 1. Using the kinetic data and Equation (4), the estimated values of lifetime in nitrogen and air atmosphere at a mass loss of 5% at various temperatures are presented in Table 3 and 4. The theoretically calculated lifetime in nitrogen at 25°C decrease from $8\cdot10^{26}$ min to $2.5\cdot10^6$ min as the concentration of cobalt stearate increased to 0.2% w/w. The estimated lifetime for all compositions were substantially lesser in air atmosphere than in nitrogen atmosphere. For air atmosphere, the lifetime was predicted assuming pseudo first order reaction kinetics. It can be seen that the lifetime is strongly dependant on the serv-

Table 3. Results of lifetime as a function of service temperature in the presence of varying amounts of cobalt stearate in nitrogen atmosphere

Sample designation	Lifetime [minutes]					
	25°C	75°C	100°C	125°C	150°C	200°C
F1	$8.2\cdot10^{26}$	$7.5\cdot10^{19}$	$1.2\cdot10^{17}$	$4\cdot10^{14}$	$2.7\cdot10^{12}$	$6.3\cdot10^{8}$
FCS5	$1.3\cdot10^{20}$	$3.5\cdot10^{14}$	$2.2\cdot10^{12}$	$2.3\cdot10^{10}$	$4.5\cdot10^{8}$	$5.7\cdot10^{5}$
FCS10	$2.5\cdot10^{9}$	$7.9\cdot10^{6}$	$7.9\cdot10^{5}$	$1.06\cdot10^{5}$	$1.8\cdot10^{4}$	$9.0\cdot10^{2}$
FCS15	$2.4\cdot10^{8}$	$1.6\cdot10^{6}$	$2.2\cdot10^{5}$	$3.9\cdot10^{4}$	$8.5\cdot10^{3}$	$6.5\cdot10^{2}$
FCS20	$2.5\cdot10^{6}$	$2.9\cdot10^{4}$	$5.0\cdot10^{3}$	$1.1\cdot10^{3}$	$2.8\cdot10^{2}$	28

Table 4. Results of lifetime as a function of service temperature in the presence of varying amounts of cobalt stearate in air atmosphere

Sample designation	Lifetime [minutes]					
	25°C	75°C	100°C	125°C	150°C	200°C
F1	$2.1\cdot10^{8}$	$2.7\cdot10^{4}$	$4.2\cdot10^{6}$	$7.3\cdot10^{2}$	$1.6\cdot10^{2}$	$1.5\cdot10^{5}$
FCS5	$3.9\cdot10^{6}$	$6.5\cdot10^{3}$	$4.3\cdot10^{3}$	$2.8\cdot10^{2}$	79	14
FCS10	$4.5\cdot10^{5}$	$3.6\cdot10^{2}$	$1.2\cdot10^{3}$	35	16	9
FCS15	$3.5\cdot10^{3}$	$3.1\cdot10^{2}$	$1.1\cdot10^{2}$	11	14	5
FCS20	$8.9\cdot10^{2}$	$2.1\cdot10^{2}$	$1.1\cdot10^{2}$	10	5	3

ice temperature and decrease dramatically as the temperature increases from 25°C to 200°C. To test these predictions, isothermal runs were performed in nitrogen and air atmosphere. The isothermal runs for FCS20 at different temperatures in nitrogen and air atmosphere are presented in Figure 5 and 6. It can be observed that the predictions are fairly accurate in nitrogen atmosphere especially at high temperatures but inaccurate in air atmosphere. In air, all the samples gained weight, due to the formation of polymeric oxides [9], as a function of time at lower temperatures and lost weight only at temperatures higher than melting point. From Figure 2, it is apparent that in air atmosphere, the degradation process does not exhibit any systematic temperature shifts with heating rate as a result of which the log β *vs* 1/*T* are not parallel. This result in deviation of actual lifetime from those predicted. Moreover, the kinetics of the degradation process depends strongly on the chain mobility, which further depends on the physical state of the polymer. The chain mobility is much higher in the molten state than in the solid state thereby making the predictions even more inaccurate in the solid state.

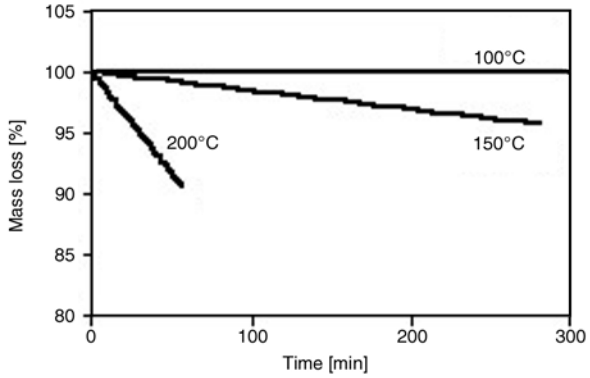

Figure 5. Isothermal runs on FCS20 in nitrogen atmosphere at different temperatures

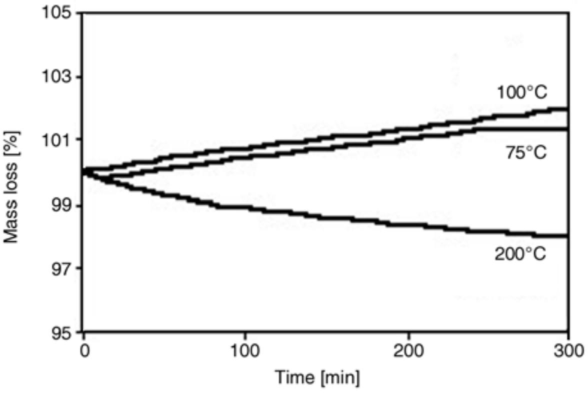

Figure 6. Isothermal runs on FCS20 in air atmosphere at different temperatures

3.4. Air-oven aging studies

Although the lifetime of LDPE and other formulations could not be quantified using non-isothermal technique in air atmosphere, cobalt stearate does have a strong effect on the lifetime of LDPE, and this has been demonstrated by air oven studies. Figure 7–10 depict the effect of thermal exposure (at 70°C and 100°C) on the elongation at break and CI of F1 and FCS10 films. LDPE films have a tensile strength of 12.8±1 MPa and elongation at break of 149±10 mm respectively. FCS10 also exhibits mechanical properties in the same range initially indicating that it does not lead to degradation during the processing stage. It was observed that the tensile strength does not show any decrease, however, elongation at break show a massive decrease and the same have been reported here. FCS10 films lose ~90% of its initial elongation after 100 h and 9 h of thermal exposure at 70°C and 100°C respectively (Figure 8 and 10). Neat LDPE films however

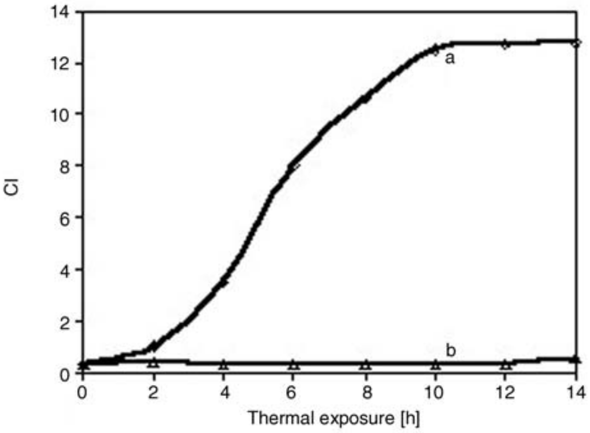

Figure 7. Variation of Carbonyl Index [CI] of a) FCS10 and b) F1 with thermal exposure at 100°C

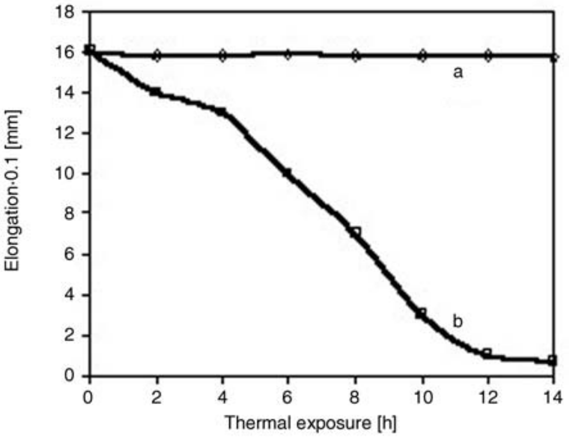

Figure 8. Variation of Elongation at break for a) F1 and b) FCS10 with thermal exposure at 100°C

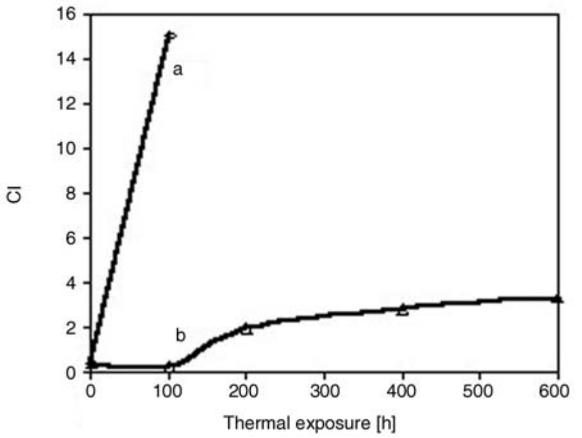

Figure 9. Variation of Carbonyl Index [CI] of a) FCS10 and b) F1 with thermal exposure at 70°C

show only 60–70% loss even after 600 h of thermal exposure at 70°C. Investigation of the FTIR spectra reveals that FCS10 shows significant changes in the carbonyl (1785–1700 cm^{-1}), amorphous (1300 cm^{-1}) and hydroxyl regions (3400 cm^{-1}). The absorption band due to stretching of carbonyl group, which is centered around 1714 cm^{-1} grow in intensity and at the same time, a band broadening is observed which indicate the presence of numerous oxidation products like aldehydes (1733 cm^{-1}), carboxylic acid groups (1700 cm^{-1}) and (lactones (1780 cm^{-1}) [24]. It has been reported that polyethylene films enter into the decay stage at CI greater than 6 [25]. Increase in the CI of F1 was not significant and did not reach this stage even after 600 h of thermal exposure at 70°C. Samples containing cobalt stearate however had undergone significant degradation as apparent from a large increase in CI during the initial period of thermo-oxidation and the samples completely broke off after 100 h of exposure. The effect of air oven ageing on the MFI was also determined and it was observed that MFI for neat LDPE increased from 3.67 to 7.56 after 600 h of thermal exposure at 70°C, which is indicative of chain scission resulting in lower molecular weight. The increase in MFI of FCS10 sample was much higher and could not be determined after 9 h of thermal exposure at 100°C and ~100 h at 70°C. The molecular weight of these films decreased drastically which affected the flow behaviour of the polymer and it flowed freely under the MFI test conditions. All these results indicate that cobalt stearate can cause rapid thermo-oxidative degradation of LDPE.

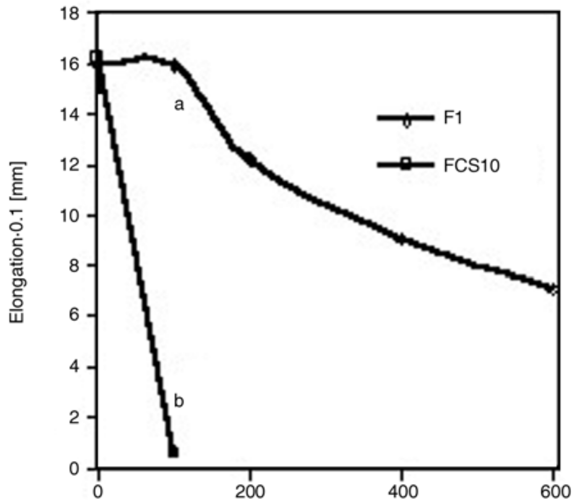

Figure 10. Variation of Elongation at break for a) F1 and b) FCS10 with thermal exposure at 70°C

Although the pro-oxidative nature of cobalt stearate is also reflected in the non-isothermal thermogravimetric analysis, the lifetime of the polymer cannot be predicted based on empirical equations because of the non-systematic degradation of the polymer in air atmosphere.

4. Conclusions

The thermal stability and degradation kinetics of LDPE and formulations containing cobalt stearate as a pro-oxidant has been investigated in this paper. The apparent kinetic parameters were evaluated using Flynn-Wall-Ozawa iso-conversion technique, which has yielded the dependencies of the effective activation energy on the extent of polyethylene degradation. The activation energy was calculated from the slopes of the iso-conversion plots and was found to be much higher in nitrogen than in air atmosphere. In nitrogen atmosphere, the activation energy was found to increase with conversion and the higher values of activation energy observed in the latter stages indicate that the degradation becomes limited by degradation initiated by random chain scission. In air, the later stages of degradation are obscured by polymer ignition at ~400°C. Cobalt stearate accelerated both pyrolysis as well as thermo-oxidative degradation as indicated by lower E_a values which indicate that in presence of cobalt stearate, the degradation follows an alternate route. The influence of cobalt stearate on the pyrolysis products was beyond the scope of this study and still needs to be addressed. Presence of even small amounts of cobalt stearate in LDPE films resulted in a significant decrease in the lifetime. The theoretically derived values of lifetime were confirmed by isothermal runs at selected temperatures. The studies indicated that the predictions are fairly accurate in nitrogen atmosphere but fail in air atmosphere. This has been explained on the basis of irregular degradation process in air atmosphere.

Acknowledgements

The authors wish to acknowledge A. K. Kapoor, Director, Centre for Fire, Explosive and Environment Safety for providing the laboratory facilities. Thanks are also due to Dr. Raman for FTIR analysis.

References

[1] Khabbaz F., Albertsson A. C.: Rapid test methods for analyzing degradable polyolefins with a pro-oxidant system. Journal of Applied Polymer Science, **79**, 2309–2316 (2001).

[2] Roy P. K., Surekha P., Rajagopal C., Raman R., Choudhary V.: Study on the degradation of low-density polyethylene in the presence of cobalt stearate and benzyl. Journal of Applied Polymer Science, **99**, 236–243 (2006).

[3] Roy P. K., Surekha P., Rajagopal C., Chatterjee S. N., Choudhary V.: Effect of benzil and cobalt stearate on the aging of low-density polyethylene films. Polymer Degradation and Stability, **90**, 577–585 (2005).

[4] Roy P. K., Surekha P., Rajagopal C., Chatterjee S. N., Choudhary V.: Accelerated aging of LDPE films containing cobalt complexes as prooxidants. Polymer Degradation and Stability, **91**, 1791–1799 (2006).

[5] Roy P. K., Surekha P., Rajagopal C., Choudhary V.: Effect of cobalt carboxylates on the photo-oxidative degradation of low-density polyethylene. Part I. Polymer Degradation and Stability, **91**, 1980–1988 (2006).

[6] Stivala S. S., Kimura J., Gabbay S. M.: Thermal Degradation and Oxidative Processes. in 'Degradation and stabilization of polymers' (ed.: Allen N. S.) Applied Science Publishers, London, 82–83 (1983).

[7] Yang J., Miranda R., Roy C.: Using the DTG curve fitting method to determine the apparent kinetic parameters of thermal decomposition of polymers. Polymer Degradation and Stability, **73**, 455–461 (2001).

[8] Landau M.: Driers and Metallic Soaps. in 'Encyclopedia of Chemical Technology' (ed.: Howe-Grant M.) John Wiley & Sons, New York, Volume **8**, 432–445 (1991).

[9] Hinsken H., Moss S., Pauquet J-R., Zweifel H.: Degradation of polymers during melt processing. Polymer Degradation and Stability, **34**, 279–293 (1991).

[10] Vasele C., Costea E., Odochian L.: The thermoxidative decomposition of low density polyethylene in non-isothermal conditions. Thermochimica Acta, **184**, 305–311 (1991).

[11] Doyle C. D.: Estimating thermal stability of experimental polymers by Empirical thermogravimetric analysis. Analytical Chemistry, **33**, 77–79 (1961).

[12] Ozawa T.: Non-isothermal kinetics and generalized time. Thermochimica Acta, **100**, 109–113 (1986).

[13] Flynn J. H., Wall L. A.: A quick direct method for the determination of activation energy from thermogravimetric data. Journal of Polymer Science: B Polymer Letters, **4**, 323–328 (1966).

[14] Peterson J. D., Vyazovkin S., Wight C. A.: Kinetics of the thermal and thermo-oxidative degradation of polystyrene, polyethylene and poly (propylene). Macromolecular Chemistry and Physics, **202**, 775–784 (2001).

[15] Kiran Ciliz N., Ekinci E., Snape C. E.: Recycling of plastic waste via pyrolysis. Resources, Conservation. Recycling, **29**, 273–283 (2000).

[16] Kiran Ciliz N., Ekinci E., Snape C. E.: Pyrolysis of virgin and waste polypropylene and its mixtures with waste polyethylene and polystyrene. Waste Management, **24**, 173–181 (2004).

[17] Heikkinen J. M., Hordijk J. C., de Jong W., Spliethoff H.: Thermogravimetry as a tool to classify waste components to be used for energy generation. Journal of Analytical and Applied Pyrolysis, **71**, 883–900 (2004).

[18] Dominguez A., Blanco C. G., Barriocanal C., Alvarez R., Dez M. A.: Gas chromatographic study of the volatile products from coal and polyethylene wastes. Journal of. Chromatograph A, **918**, 135–144 (2001).

[19] Koo J. M., Kim S. W.: Reaction kinetic model for optimal pyrolysis of plastic waste mixtures. Waste Management Research, **11**, 515–529 (1993).

[20] McCoy B. J.: Distribution kinetics for temperature programmed pyrolysis. Industrial Engineering Chemical Research, **38**, 4531–4537 (1999).

[21] Wang H., Tao X., Newton E.: Thermal degradation kinetics and lifetime prediction of a luminescent conducting polymer. Polymer International, **53**, 20–26 (2004).

[22] Li X. G., Huang M. R.: Thermal decomposition kinetics of thermotropic poly (oxybenzoate-co-oxynaphthoate) vectra copolyester. Polymer Degradation and Stability, **64**, 81–90 (1999).

[23] Huang M. R., Li X. G.: Thermal degradation of cellulose and cellulose esters. Journal of Applied Polymer Science, **68**, 293–304 (1998).

[24] Gugumus F.: Thermooxidative degradation of polyolefins in the solid state: part I. Experimental kinetics of functional group formation. Polymer Degradation and Stability, **52**, 131–144 (1996).

[25] Lin Y.: Study of photooxidative degradation of LDPE film containing cerium carboxylate photosensitiser. Journal of Applied Polymer Science, **63**, 811–818 (1997).

eXPRESS Polymer Letters Vol.1, No.4 (2007) 217–225
Available online at www.expresspolymlett.com
DOI: 10.3144/expresspolymlett.2007.33

Tensile property of thin microcellular PC sheets prepared by compression molding

Z. Xiao, R. Guan, Y. Jiang, Y. Li*

College of Chemistry and Chemical Engineering, Hubei University, Wuhan, 430062, China

Received 3 January 2007; accepted in revised form 1 April 2007

Abstract. Thin microcellular polycarbonate (PC) sheets have been prepared by compression molding. Tensile tests were performed on microcellular PC sheets prepared under different conditions, and results show that foaming time plays the main role on the tensile property. The cellular structure prepared in this process has been shown to have a significant effect on the corresponding tensile property of microcellular PC foams. For these foams, Single Blend model can be used to predict the effect of the relative density on the relative strength, but the experiment data of the tensile modulus is much lower than that predicted by Square-Relationship Model. The effect of cell size on the tensile property of microcellular PC foams was also investigated, and found that the cell size can affect the tensile property, which is different from the result of Kumar. In order to make the tensile property predictable, some mathematical formulas were also simulated.

Keywords: *mechanical properties, microcellular, polycarbonate, simulation*

1. Introduction

Due to the special structure of microcellular foams, they can be used in many areas, such as packaging, insulation, bone substitute material, military aircraft and microelectronic application. In the microcellular foam application, the mechanical property is a very important factor to consider.

There is considerable literature on the mechanical properties of conventional foams [1–8], particularly in the book edited by Gibson and Ashby [2], but too limited reports on that of microcellular foams. Since the microcellular foam was successfully prepared by Suh and his co-workers [9–11] in Massachusetts Institute of Technology, some researchers have focused on the tensile property of microcellular foam. Waldman [12] reported that the tensile strength of microcellular polystyrene (PS) foam follows a linear relationship with the specific density, but much higher than that of the structural foam when Young's modulus is kept constant. Kumar and Van der Wel [13] found that the tensile strength of polycarbonate (PC) microcellular foam was lower than that predicted by the law of mixture, and Young's modulus was larger than that of structural foam. Collias and Baird [14] studied the tensile toughness (the area under the stress-strain curve) of microcellular foams of PS, PC and Styrene-Acrylonitrile (SAN) copolymer. They concluded that microcellular PS foam shows limited improvement in the tensile toughness, but microcellular SAN and PC foams show deterioration in tensile toughness. Later on, Sun *et al.* [15] carried out mechanical tests both in compression and tension, and they drew a conclusion that Young's modulus and strength are closely related to the relative density. Youn and Suh [16] found that the flexural toughness of polyester microcellular foam increases by a factor of 3 for 30% bubble volume fraction compared to the neat polyester, although the strength is about the same. Aroka [17] investigated the effect of the cell size and shape on the

---

*Corresponding author, e-mail: rongguan@hubu.edu.cn

© BME-PT and GTE

compressive yield stress of microcellular PS foam, and found that the compressive strength of foam increases with the increase of cell size, and their data are higher than those predicted by an anisotropic foam model. Recently there has been some research dealing with the effect of relative density on the mechanical property of microcellular composite foams [18, 19], however, they only related mechanical property with the relative density, but fewer reports are available on the effect of processing parameters and cell size on the tensile property.

The objective of this paper is twofold. One is to assess the importance of processing parameters which affect the tensile property. These processing parameters include foaming time, foaming pressure and foaming temperature. The other is to investigate the effect of cellular structure, that is, the relative density and the cell size, on the tensile property, and compare the experimental data with the values predicted by Gibson and Ashby [2].

2. Experimental

2.1. Materials

The polycarbonate (PC) sheets used in this work were commercial-grade product with a thickness of 0.178 mm, purchased from GE Corporation. Low density polyethylene (LDPE) pellet from Sinopec Beijing Yanshan Chemical Corporation Factory (Beijing, China), with a melt index 2 g/10 min at 190°C, was used as received. Commercial-grade azobisformamide (AC) from Wuhan Hanhong Chemical Reagent Corporation of China (Wuhan, China), was used as blowing agent. The amount of gas yielded, which mainly consists of nitrogen, carbon monxide, carbon dioxide and ammonia, is about 200–220 ml/g. Dicumyl peroxide (DCP), Sinopharm Chemical Reagent Coporation, Ltd. (Shanghai, China), was used as received. Analytical-grade zinc oxide (ZnO) from Shanghai Shiyi Chemical Reagent Co.Ltd. (Shanghai, China), was used as activate agent for AC decomposition.

2.2. Microcellular PC foam preparation

The preparation of microcellular PC foam consists of two processing steps. First, according to the formula, 200 g LDPE, 40 g AC, 5 g DCP and 20 g ZnO were mixed in a two-roll mill as a gas source for PC foaming. Second, the PC sheets and the mixed LDPE were placed in a 250×250×2 mm mold together and loaded in a hydraulic hot press under experimental conditions.

After the required foaming time and other conditions were reached, the pressure was released and the mold was taken out of the hot press immediately. Then we unloaded the mold, quenched it to room temperature within 30 s; and removed the microcellular PC foam from the mold. Thus, the microcellular PC samples were ready for property characterization after being kept at room temperature for at least 2 days.

2.3. Microcellular PC foam characterization

The cell size of the foamed samples was calculated according to the image observed under a Nikon YS2 optical microscopy (using a 100× amplify camera lens), following the procedure described previously by Kumar *et al.* [20] and Equations (1) and (2).

$$V_f = \frac{\pi D_c^3 N_f}{6} \tag{1}$$

$$N_0 = \frac{N_f}{1 - V_f} \tag{2}$$

where V_f is the volume fraction of the foamed material, D_c is the average cell size measured from the photographs, N_f is the cell density relative to the foamed material, and N_0 is the cell density relative to the neat material.

The specific density of foamed samples was measured according to the method used by Yuan [19], and concrete procedure was shown in ASTM-792 standard. When the specific density was less than 1.0, the foamed samples were immersed into water by the help of a thin copper sheet. The specific density and relative density are calculated by Equations (3) and (4), respectively.

$$\rho_f = 0.9975 \cdot \frac{M_a}{M_w} \tag{3}$$

$$\rho_r = \frac{\rho_f}{\rho_0} \tag{4}$$

where ρ_0, ρ_f is the specific density of the unfoamed and foamed material, respectively; M_a and M_w are the weight of the samples measured in air and water, respectively; ρ_r is the relative density.

The microcellular PC sheets were machined into dumbbell-shape specimens with a gage length of 50 mm (ASTM D638 type II specimen), the specimen thickness varied with the expansion of foam. For each sample, at least five samples were tested and the average data are reported in this article. The tensile test was carried out at room temperature using a Shimadzu AG-A all-purpose testing machine (Japan) equipped with a 1000 lb load cell at a constant crosshead rate of 50 mm/min.

3. Results and discussion

3.1. Tensile behavior of unfoamed and microcellular PC sheets

Figure 1 shows the typical stress-strain curves of unfoamed and microcellular foamed PC sheets, they can be divided into three regions: in the first region stress increases steeply with the increase of strain; the central region in which stress remains constant and strain varies quickly; and the last region where stress varies with the increase of strain up to fracture. The relative density decreases when PC sheet is microcellularly foamed, the tensile strength at break, the elongation at break evidently decreases and the yield point becomes faint. This is because the gas acts as a plasticizer. The experimental data that reflect the effect of processing parameters on the tensile property, such as tensile strength, tensile modulus, specific strength, breaking elongation, are listed in Table 1 and are discussed as follows.

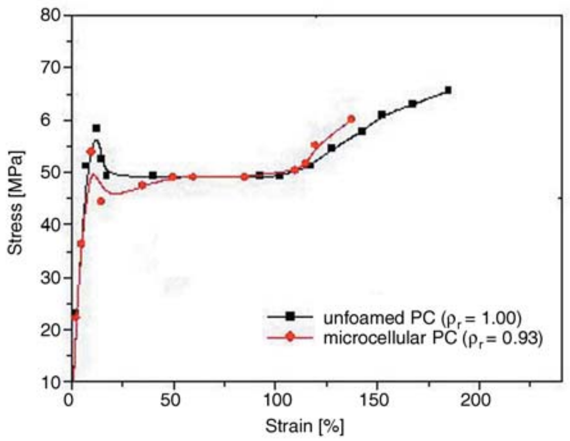

Figure1. The stress-strain curves of unfoamed and microcellular PC sheets (foaming time is 10 min, foaming pressure is 20 MPa, foaming temperature is 130°C)

3.1.1. The effect of processing parameters on tensile strength

From Figure 2, it can be seen that the tensile strength decreases with the increase of each processing parameter. However, when foaming time varies, the tensile strength changes more than the ones in other foaming conditions. Hence, combined with Table 1, it can be concluded that foaming time plays the main role on the tensile strength. Under the pressure of 18 MPa, 20 MPa and 22 MPa as shown in Figure 2a, the tensile strength is evidently affected by foaming time, and decreases with the increase of foaming time. The foaming pressure can also affect the tensile strength as shown in Figure 2b, when foaming pressure increases, the

Table 1. The experimental data of the microcellular PC sheets prepared under different processing conditions

Foaming time [min]	Foaming pressure [MPa]	Upper-plate temperature [°C]	Cell size [µm]	Standard deviation [µm]	Cell density N_0 [10^8 cells/cm^3]	Relative density	Tensile modulus [MPa]	Tensile strength [MPa]	Breaking elongation [%]
0	0	0	0	0	0	1.000	2157.5	66.1	185.70
7	18	140	9.2	1.12	2.18	0.912	951.1	60.6	153.82
8	18	140	4.5	0.974	27.84	0.876	925.2	59.4	145.30
9	18	140	6.6	0.844	8.22	0.874	877.2	58.8	143.06
10	18	140	7.1	0.966	6.37	0.804	825.9	56.9	134.80
11	18	140	10.3	1.28	4.15	0.747	771.3	51.3	133.54
12	18	140	10.8	2.19	2.53	0.767	680.8	47.2	131.82
10	12	140	9.0	0.842	7.46	0.896	970.0	60.2	123.49
10	14	140	8.0	1.59	16.09	0.874	879.9	58.6	125.49
10	16	140	7.4	0.982	17.64	0.872	833.4	58.0	127.05
10	18	140	7.1	0.966	23.32	0.864	825.9	57.5	134.80
10	20	140	6.8	0.965	22.78	0.857	784.9	56.9	127.21
10	22	140	6.2	1.27	33.86	0.844	766.3	55.2	123.55
10	20	130	4.3	0.718	23.87	0.927	906.8	58.8	131.22
10	20	135	5.6	0.768	16.61	0.857	822.5	57.9	123.40
10	20	140	6.8	0.965	10.30	0.795	784.9	56.9	127.21

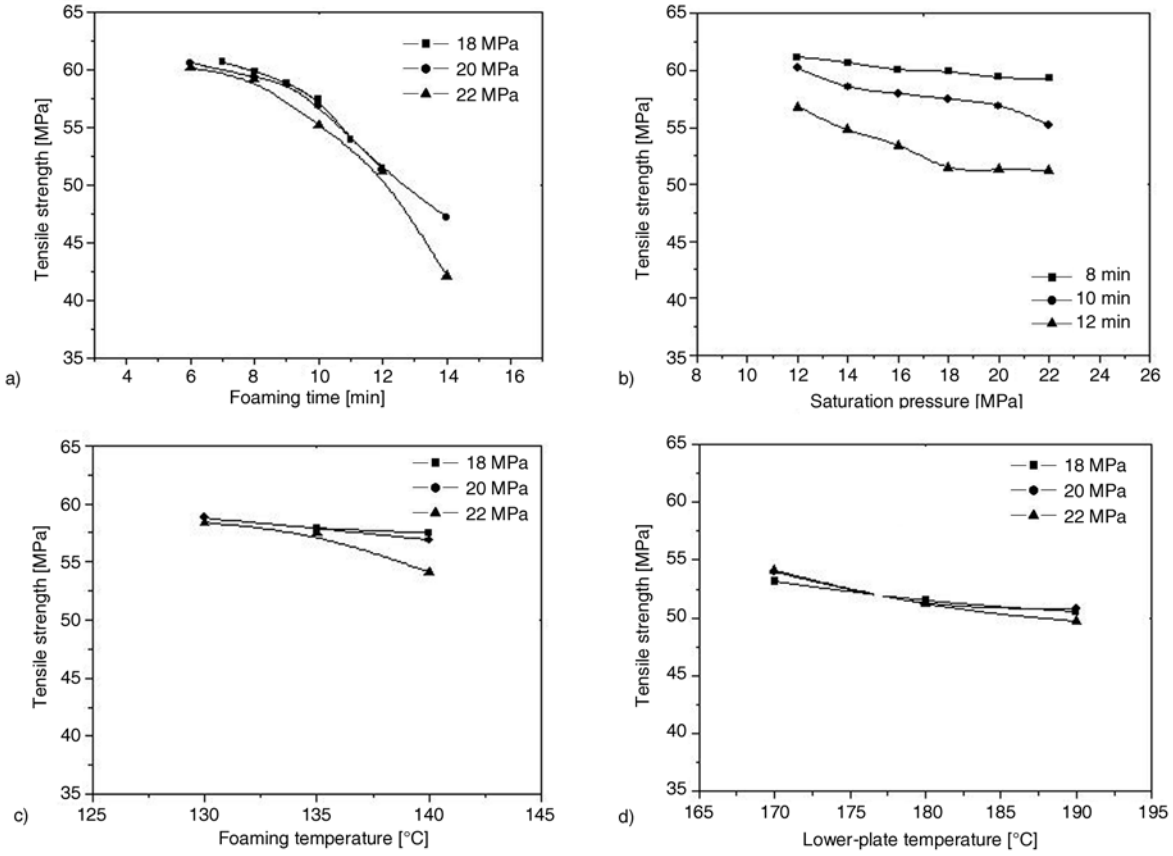

Figure 2. The effect of processing parameters on tensile strength of microcellular PC sheets

tensile strength decreases gradually. But the effect of upper-plate temperature and lower-plate temperature on the tensile strength is too limited as shown in Figures 2c and 2d. This is perhaps due to the decrease of relative density and the growth of cell. When foaming time, foaming temperature and lower-plate temperature increase, the relative density decreases and the cell size increases. Thus, the foamed microcellular PC can stand less stress. As for the effect of foaming pressure on the tensile strength, although cell size decreases with the increase of foaming pressure, the decreased relative density plays the main role in the tensile strength. The result is the same to that reported by Gibson [2], the tensile strength is proportional to the relative density. And the foaming time plays more important role in the decreased relative density than other foaming conditions in our considered experimental conditions. So the tensile strength decreases with the increase of foaming parameters, especially with the increase of foaming time.

3.1.2. The effect of processing parameters on tensile modulus

As shown in Figure 3, tensile modulus decreases with the increase of each processing parameter, and foaming time affects tensile modulus to larger extent, the variation trend is similar to that of tensile strength. When foaming time increases, tensile modulus decreases to the lowest point as shown in Figure 3a; and as the other three processing parameters increase, tensile modulus decreases to different points as shown in Figures 3b, 3c and 3d. The reason is similar to that of the tensile strength, the tensile modulus is also a function of the relative density. The relative density decreases with the increase of processing parameters; and decreases much more with the foaming time than with other foaming conditions. In addition, the dissolved gas acts as a plasticizer when performing tensile test. So the tensile modulus also decreases with the increase of each processing parameter, especially with the increase of the foaming time.

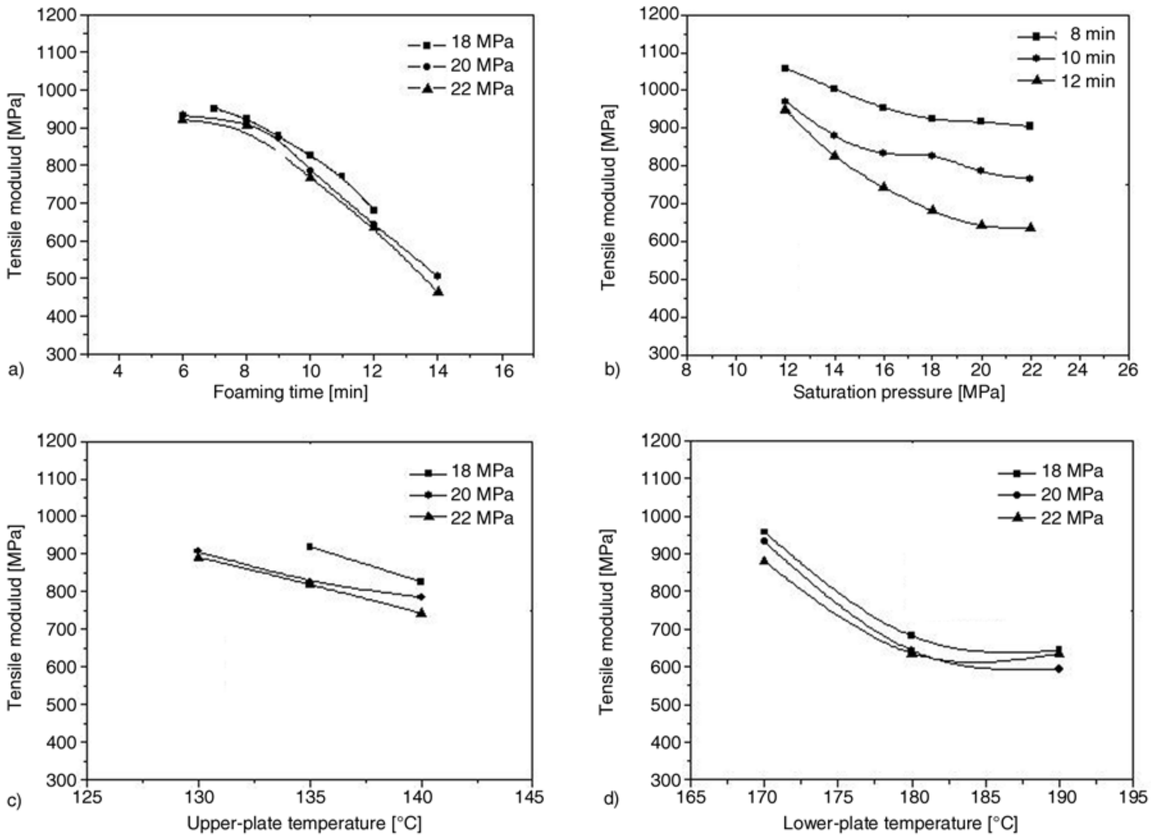

Figure 3. The effect of processing parameters on tensile modulus of microcellular PC sheets

3.1.3. The effect of processing parameters on specific strength

In this paper, the specific strength, which is affected by processing parameters in a complex manner, is defined as the ratio of tensile strength to relative density. The specific strength of non-foamed PC sheet is 66.1 MPa, in most cases, it becomes larger when PC sheets are in microcellular foamed state, as shown in Figure 4. When foaming time and lower-plate temperature increase, the specific strength increases to a certain value and then decreases as shown in Figures 4a and 4d. But when the foaming pressure and upper-plate temperature increase, the specific strength increases as shown in Figures 4b and 4c. This result satisfies the initial aim of inventing microcellular foam. After microcellular foaming, the mechanical property decreases less compared to the decreased relative density, so the specific strength of PC sheet is increased after microcellular foaming.

3.1.4. The effect of processing parameters on elongation at break

Elongation at berak is an important parameter to assess whether the microcellular foam is toughened or not, and the elongation at break of non-foamed PC sheet is 185.70% in our experiment. From Figure 5 we can see that the elongation at break of microcellular PC sheets is decreased, it agrees with the result of Kumar and Van der Wel [13]. When foaming time increases, the elongation at break decreases to larger extent under the pressure of 18 MPa, 20 MPa and 22 MPa, but the elongation at break varies differently with the increase of each processing parameter. This result may be caused by the decreased relative density and the deterioration of microcells. The relative density decreases with the increase of processing parameters, the elongation at break decreases. When the microcells generated are larger than certain size, they can result in the embrittlement of the foamed sample. Hence, the reduced elongation at break after microcellular foaming in this research may be the result of larger cell size.

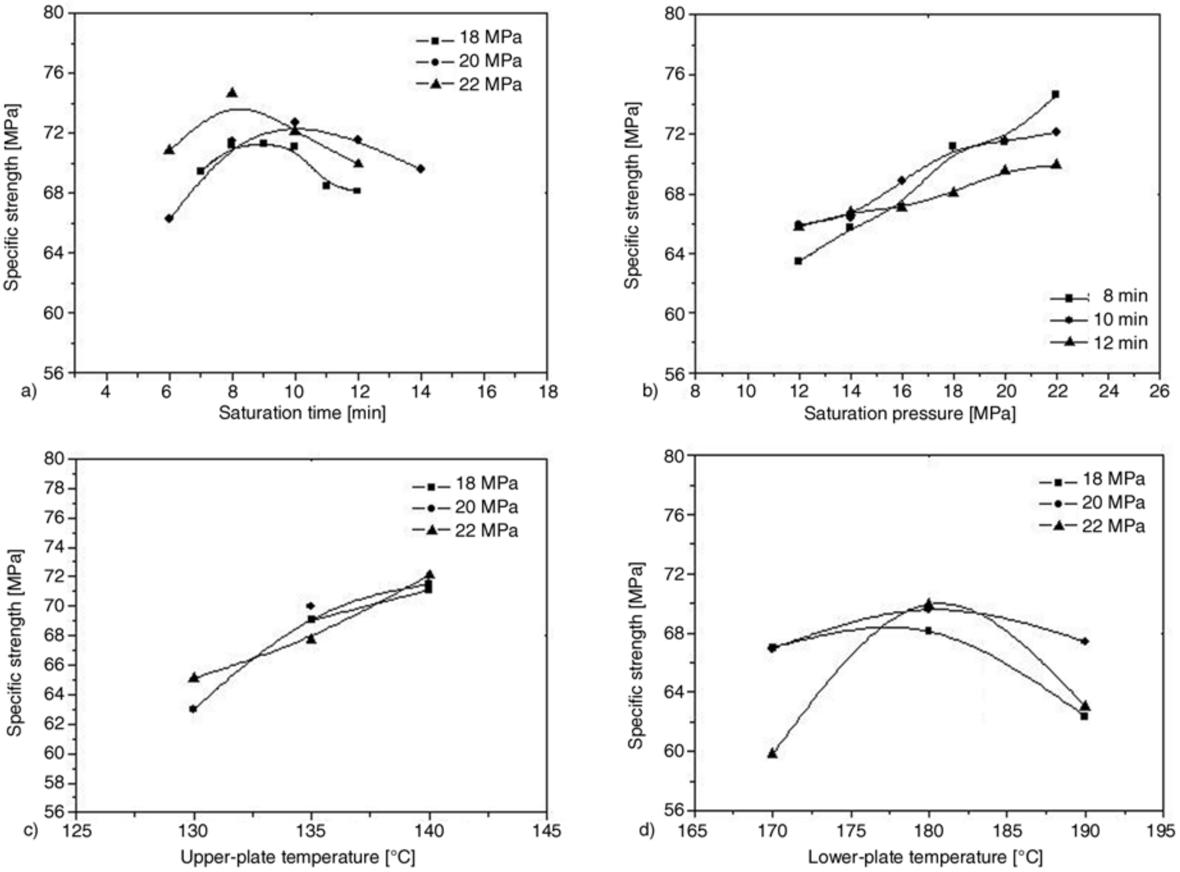

Figure 4. The effect of processing parameters on specific strength of microcellular PC sheets

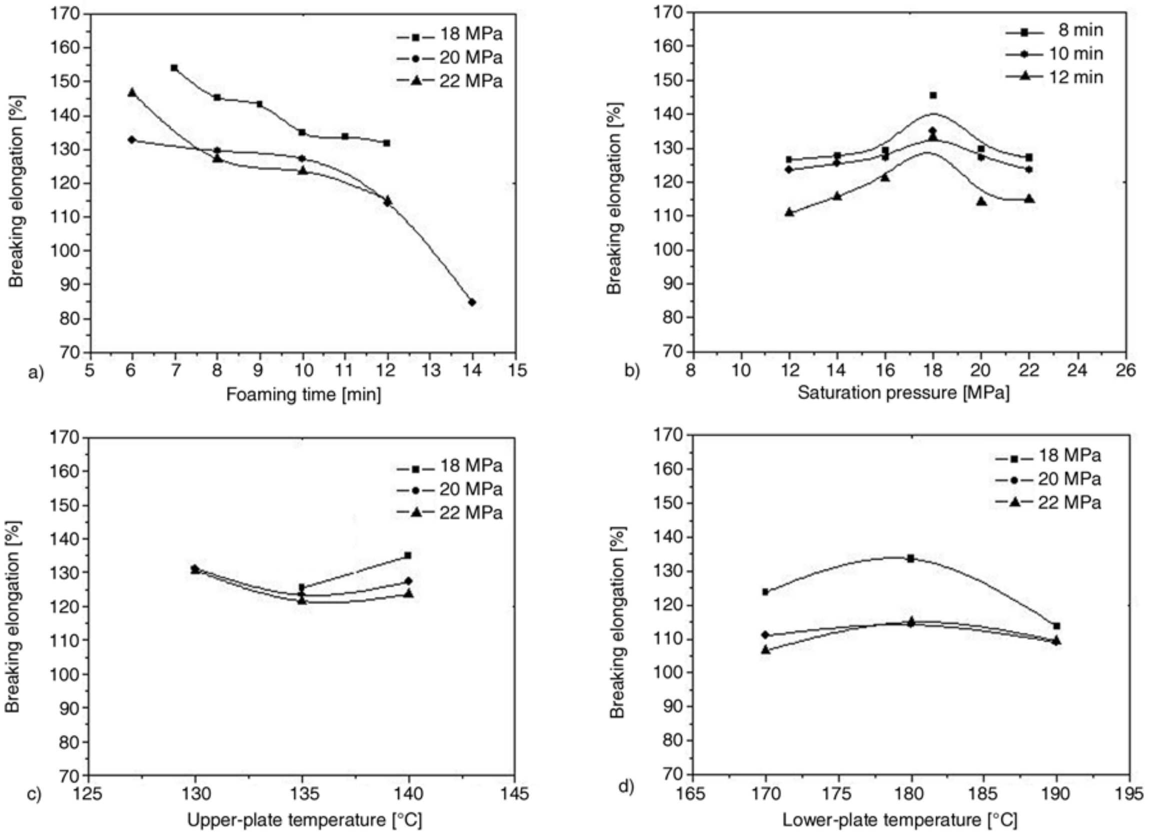

Figure 5. The effect of processing parameters on breaking elongation of microcellular PC sheets

3.2. The effect of relative density on tensile property

In order to investigate the effect of relative density on tensile property clearly, some microcellular PC sheets with the same cell size and the different relative density were tested by using universal tensile tester. Figure 6 shows the effect of the relative density on the tensile strength and the tensile modulus of microcellular PC sheets, whose cell size is in the range of 5.0~6.0 μm and the relative density is in the range of 0.65~0.98. As shown in Figure 6, the relative tensile strength and the relative tensile modulus increase with the increase of relative density. We have compared our experimental data with that predicted by the Square-Relationship model and Single Blend model [21]. The two models are represented by Equations (5) and (6).

$$E_r = \rho_r^2 \tag{5}$$

$$\sigma_r = \rho_r \tag{6}$$

where E_r is the relative tensile modulus of microcellular foam (E_f/E_0), E_f is the tensile modulus of microcellular foam [MPa], E_0 is the tensile modulus of non-foamed polymer [MPa]; σ_r is the relative tensile strength of microcellular foam (σ_f/σ_0), σ_f, tensile strength of the foam [MPa]; σ_0, tensile modulus of the non-foamed polymer [MPa].

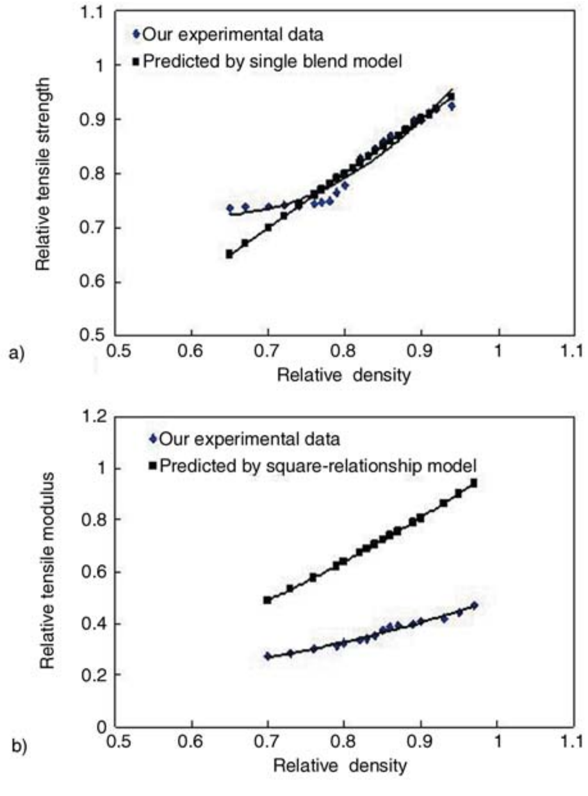

Figure 6. The effect of relative density on tensile property of microcellular PC sheets

The comparisons between experimental data and predicted value are shown in Figure 6. The experimental data of the relative strength at break approximately fits well with the curve predicted by Single Blend model for the relative density is in the range of 0.65~0.98, but the relative modulus is evidently smaller than that predicted by Square-Relationship Model, this may come from the origin material property and its cell size. In order to accurately predict the tensile strength and the tensile modulus relationship with the relative density, the experimental data between the tensile property and the relative density were simulated, and Equations (7) and (8) are fit to our experimental data well.

$$E_r = 0.8021\rho_r^2 - 0.6041\rho_r + 0.2987 \tag{7}$$

$$\sigma_r = 2.5278\rho_r^2 - 3.2232\rho_r + 1.7521 \tag{8}$$

3.3. The effect of cell density on tensile property

There have been fewer reports about the effect of cell size on the tensile property. Only Kumar and Weller [22] investigated the effect of cell size on the tensile behavior of microcellular PC, and found that the cell size had no effect on the tensile behavior. Since the microcellular foams exhibit some special properties compared to the conventional foams with the same specific density, we assume that the cell size should have the effect on the tensile property. Thus, we selected the microcellular PC foam samples with the same relative density and the different cell size, and measured their tensile property.

Figure 7 shows the effect of cell size on the tensile strength and the tensile modulus of microcellular PC sheets, whose relative density is in the range of 0.86~0.87 and cell size is in the range of 3~14 μm. As shown in Figure 7, the relative tensile strength and the relative tensile modulus decrease with the increase of cell size, which doesn't agree with Kumar's conclusion [22]. The disagreement may be the result of the different way of preparing the microcellular PC foam. When the cell size becomes larger as shown in Figure 8 and the relative density keeps constant, each bubble can stand less stress

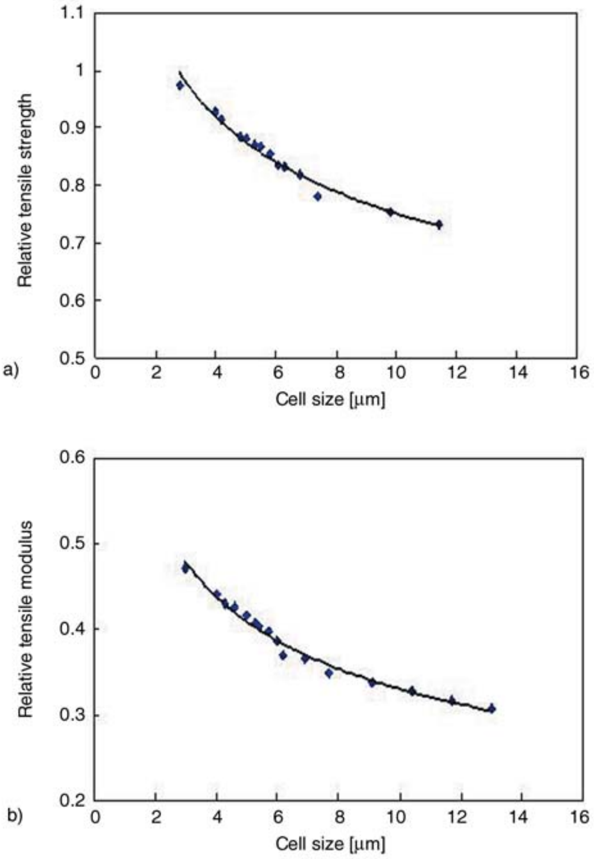

Figure 7. The effect of cell size on tensile property of microcellular PC sheets

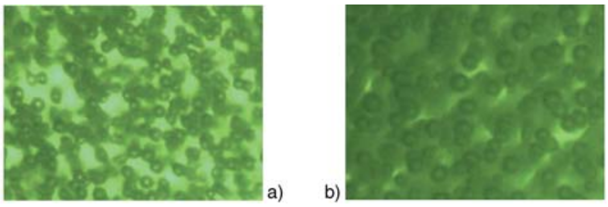

Figure 8. The photograph of optical microscope of microcellular PC; (a): smaller cell and (b): lager cell

when stress was put on microcellular foams; and when the cell size becomes larger and the relative density keeps constant, the decreased cell density results in fewer bubbles that can share stress put on microcellular foam, so relative tensile strength and relative tensile modulus decrease with the increase of cell size.

In order to predict the effect of cell size on the tensile strength and the tensile modulus, we also simulated the relationship between cell size and tensile property, and Equations (9) and (10) are fit to experimental data well.

$$E_r = \frac{0.667}{D_c^{0.3125}} \tag{9}$$

$$\sigma_r = \frac{1.2489}{D_c^{0.2207}} \tag{10}$$

From the results discussed above, the cell size does affect the tensile property under our experimental conditions, and the relative tensile strength and relative tensile modulus are a function of $1/D_c$. In order to predict the tensile strength and tensile modulus on the basis of relative density and cell size, the relationship between cellular structure and tensile property can be expressed in Equations (11) and (12):

$$\frac{E_f}{E_0} = A \cdot \left(\frac{\rho_f}{\rho_0}\right)^m \cdot \left(\frac{1}{D_c}\right)^n \tag{11}$$

$$\frac{\sigma_f}{\sigma_0} = B \cdot \left(\frac{\rho_f}{\rho_0}\right)^i \cdot \left(\frac{1}{D_c}\right)^j \tag{12}$$

where A, B are fitting constants; m, n, i, j are constants related to material. And these formulas can accurately express the relationship between the cellular structure and the tensile property.

4. Conclusions

In this paper, tensile tests were performed on the thin microcellular PC sheets prepared under different conditions. The results show that foaming time plays the main role on the tensile property. The cellular structure prepared by compression molding has been shown to have a significant effect on the corresponding tensile property of the microcellular PC foams. We have investigated the effect of the cellular structure on the tensile property, and found that Single Blend model can be used to predict the effect of the relative density on the relative strength for microcellular PC foams, but the experimental data of the tensile modulus is much lower than that predicted by Square-Relationship model. The cell size can affect the tensile property to some extent in our experiment. In order to accurately express the relationship between the cellular structure and the tensile property, semi-empirical models were proposed to fit the experimental data well.

Acknowledgements

The authors are grateful to the National Natural Science Foundation of China for financial support (50473026).

References

[1] Huang J. S., Lin J. Y.: Fatigue of cellular materials. Acta Materialia, **44**, 289–296 (1996).

[2] Gibson L. J., Ashby M. F.: Structure and properties. in 'Cellular solids' (eds.: Clarke D. R., Suresh S., Ward I. M.) Cambridge University Press, New York, 307–308 (1997).

[3] Lin H. R.: The structure and property relationship of commercial foamed plastics. Polymer Testing, **16**, 429–443 (1997).

[4] Ramsteiner F., Fell N., Forster S.: Testing the deformation behavior of polymer foams. Polymer Testing, **20**, 661–670 (2001).

[5] Alonso M. V., Auad M. L., Nutt S.: Short-fiber-reinforced epoxy foams. Composites Part A-Applied Science and Manufacturing, **37**, 1952–1960 (2006).

[6] Alonso M. V., Auad M. L., Nutt S.: Modeling the compressive properties of glass fiber reinforced epoxy foam using the analysis of variance approach. Composites Science and Technology, **66**, 2126–2134 (2006).

[7] Fabrice S-M., Laurent C., Cavaille J-Y., Emanuelle C.: Mechanical property of high density polyurethane foams: I. Effect of density. Composites Science and Technology, **66**, 2700–2708 (2006).

[8] Fabrice S-M., Laurent C., Cavaille J-Y.: Mechanical property of high density polyurethane foams: II. Effect of the filler size. Composites Science and Technology, **66**, 2709–2718 (2006).

[9] Martini J. E., Waldman F. A., Suh N. P.: The production and analysis of microcellular thermoplastic foams. in 'Annual Technical Conference-Society of Plastics Engineers. San Francisco, USA', **28**, 674–676 (1982).

[10] Martini J. E., Ellen J., Suh N. P.: The production and analysis of microcellular foam. Master's Thesis, Department of Mechanical Engineering, MIT (1981).

[11] Martini J. E., Suh N. P., Waldman F. A.: Microcellular closed cell foams and their method of manufacture. Patent: 4,473,665, US (1984).

[12] Waldman F. A.: The processing of microcellular foam. Master's Thesis, Department of Mechanical Engineering, MIT (1982).

[13] Kumar V., Van der Wel M.: Microcellular polycarbonate part II: Characterization of tensile modulus. in 'Annual Technical Conference-Society of Plastics Engineers. Detroit, USA', **37**, 1406–1410 (1991).

[14] Collias D. I., Baird D. G.: Tensile toughness of microcellular foams of polystyrene, styrene-acrylonitrile copolymer, and polycarbonate, and the effect of dissolved gas on the tensile toughness of the same polymer matrices and microcellular foams. Polymer Engineering and Science, **35**, 1167–1177 (1995).

[15] Sun H., Sur G. S., Mark J. E.: Microcellular foams from polyethersulfone and polyphenylsulfone preparation and mechanical property. European Polymer Journal, **38**, 2373–2381 (2002).

[16] Youn J. R., Suh N. P.: Processing of microcellular polyester composites. Polymer Composites, **6**, 175–180 (1985).

[17] Aroka K. A., Lesser L. J., McCarthy T. J.: Compressive behavior of microcellular polystyrene foams processed in supercritical carbon dioxide. Polymer Engineering and Science, **38**, 2055–2062 (1998).

[18] Lin G., Zhang X-J., Liu L., Zhang J-C., Chen Q-M., Zhang L-Q.: Study on microstructure and mechanical property relationship of short fibers/rubber foam composites. European Polymer Journal, **40**, 1733–1742 (2004).

[19] Yuan M., Turng L-S.: Microstructure and mechanical properties of microcellular injection molded polyamide-6 nanocomposites. Polymer, **46**, 7273–7279 (2005).

[20] Kumar V., Suh N. P.: A process for making microcellular thermoplastic parts. Polymer Engineering and Science, **30**, 1323–1329 (1990).

[21] Sun H. L., Mark J. E.: Preparation, characterization, and mechanical properties of some microcellular polysulfone foams. Journal of Applied Polymer Science, **86**, 1692–1701 (2002).

[22] Kumar V., Van der Wel M., Weller J., Seller K.A.: Characterization of tensile behavior of microcellular polycarbonate. Journal of Engineering Material Technology, **116**, 439–445 (1994).

eXPRESS Polymer Letters Vol.1, No.4 (2007) 226–231
Available online at www.expresspolymlett.com
DOI: 10.3144/expresspolymlett.2007.34

Strain development in a filled epoxy resin curing under constrained and unconstrained conditions as assessed by Fibre Bragg Grating sensors

M. Harsch[*1], *J. Karger-Kocsis*[2], *F. Herzog*[1]

[1]Robert Bosch GmbH, Robert Bosch Straße, 87542 Blaichach, Germany
[2]Institut für Verbundwerkstoffe GmbH, Erwin-Schrödinger-Straße, 67663 Kaiserslautern, Germany

Received 22 February 2007; accepted in revised form 5 April 2007

Abstract. The influence of adhesion to the mould wall on the released strain of a highly filled anhydride cured epoxy resin (EP), which was hardened in an aluminium mould under constrained and unconstrained condition, was investigated. The shrinkage-induced strain was measured by fibre optical sensing technique. Fibre Bragg Grating (FBG) sensors were embedded into the curing EP placed in a cylindrical mould cavity. The cure-induced strain signals were detected in both, vertical and horizontal directions, during isothermal curing at 75°C for 1000 minutes. A huge difference in the strain signal of both directions could be detected for the different adhesion conditions. Under non-adhering condition the horizontal and vertical strain-time traces were practically identical resulting in a compressive strain at the end of about 3200 ppm, which is a proof of free or isotropic shrinking. However, under constrained condition the horizontal shrinkage in the EP was prevented due to its adhesion to the mould wall. So, the curing material shrunk preferably in vertical direction. This resulted in much higher released compressive strain signals in vertical (10 430 ppm) than in horizontal (2230 ppm) direction. The constrained cured EP resins are under inner stresses. Qualitative information on the residual stress state in the molding was deduced by exploiting the birefringence of the EP.

Keywords: *thermosetting resins, cure-induced strain, Fibre Bragg Grating sensor, adhesion, shrinkage*

1. Introduction

Engineering parts produced of thermosets are widely used in different fields like the automotive, electronic, aircraft and sports industry. Their cure as neat materials or matrices of various composites often takes place in a mould to the wall of which the curing material strongly adheres. Furthermore, thermosets may get under constraints when they are employed together with other materials (metals, ceramics) having different thermal expansion behaviour than the curing resin. During curing the adhesion to the surrounding material plays a key role in terms of induced strains and, thus, stresses. A non-adhering thermoset cures under free-shrinking condition, whereas adhesion to the mould wall prohibits unhindered contraction of resin due to which inner stresses emerge in the curing material. In an early curing stage the thermoset is 'soft' with a high potential of 'elastic' deformation and relaxation. With increasing crosslinking density the flexibility of the material decreases. Under adhering condition this leads to the build-up of inner stresses which may cause low performance, shape distortion, warpage or even failure due to matrix cracking and delamination. The technique of fibre optical measurements provides the opportunity to gain information about the cure-induced strain and, thus, to enquire the stress resistance of a material. The Fibre Bragg Grating (FBG) sensing technique

---

[*]Corresponding author, e-mail: margitharsch@yahoo.de
© BME-PT and GTE

offers numerous advantages over the traditionally used methods. Due to its small diameter (ca. 125 μm) and its chemical inertness the effective network building within the EP is hardly affected. Another advantage of this FBG method is that the outcome is independent of the geometry of the sample and of the thermal profile set for its curing. Many authors applied this method for the 'health monitoring' of composite structures [1–7]. Further studies aim at the use of fibre optical technique to characterize cure of resins [8–19]. In our earlier works [8, 9] we reported about the use of FBG sensors to monitor the cure-induced strain development in epoxy resins (EP). Beside the detection of characteristic phenomena like gelation and vitrification, the coefficient of thermal expansion was determined and parameters of the cure regime on the released strain were investigated. As reported there, FBG sensors make use of the Bragg reflectivity to detect axial changes along the optical fibre [20]. The FBG is a segment of the optical fibre with a periodic modulation of the core refractive index. Its principle is shown schematically in Figure 1.

A broadband spectrum light (Incident Spectrum) is guided along the core of the optical fibre. One particular wavelength λ_B is reflected at the gratings within the fibre core whereas the other part of the incident spectrum is transmitted through the fibre. The wavelength reflected by the FBG, the Bragg wavelength λ_B, is dependent on the effective refractive index n_{eff} of the fibre and the grating periodic spacing Λ, according to the Bragg condition (1):

$$\lambda_B = 2 \cdot n_{eff} \cdot \Lambda \quad (1)$$

Strain or temperature modulations cause changes in the effective refractive index or the periodic spacing and thereby entail a shift in the Bragg grating wavelength $\Delta\lambda_B$ (c.f. Figure 1). This shift can be detected by an optical spectrum analyzer with an accuracy of 1 pm. Further information about the theoretical background of the FBG theory as well as the measuring setup of the Bragg wavelength shift, is given in the literature [8–9, 20].

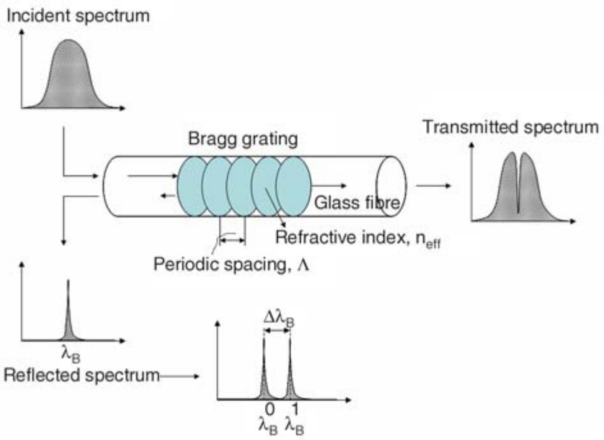

Figure 1. Principle of Fibre Bragg Grating sensor

During thermoset cure the material solidifies and contracts due to volume shrinkage. The development of compressive stresses can be measured by a shift in the reflected Bragg wavelength. Simultaneous measurements of the actual temperature allow us to eliminate the contribution of thermal changes on the wavelength signal. Adhesion to the wall may hinder the free shrinkage during cure. Therefore, the 'surroundings' influence the cure-induced strain signal to a great extent. Giordano *et al.* [17] reported about the strain signal measured by FBG after certain production steps of an EP resin. Within the mould the material had lower compressive strain than after demoulding when further relaxation amplified the compressive stresses in the cured material.

In this study we investigated the influence of adhesion on the strain development in a curing EP resin by using the fibre optical technique. Along the centre axis of a cylindrical sample holder and perpendicular to it FBG sensors were embedded in the curing material. During isothermal cure the cure-induced released strain under adhering (constrained) and non-adhering conditions (unconstrained) were measured and compared. First strain appearance measured by the FBG was compared to the validated gel point determination, based on the rheological measurement. The residual state of stress in the EP cured under constrained and unconstrained conditions was qualitatively assessed by polarized light microscopy.

2. Experimental part

2.1. Material

The investigated material was an EP system on base of Bisphenol A (Araldite MY740, molecular weight 340.41 g/mol), which was cured with a mixture of two anhydrides, viz. methyl hexahydrophthalic anhydride (molecular weight 162.14 g/mol) and hexahydrophthalic anhydride (154.17 g/mol). The mixing ratio of the EP resin to hardener was 100:83. Furthermore, the EP was loaded with a high content of inorganic filler (ca. 50 wt.%) on base of calcium silicate and calcium carbonate. All basic materials were supplied by Huntsman, Basel, Switzerland and used as provided.

2.2. Preparation and curing parameter

After stirring of resin, hardener and filler the homogenous mixture was degassed and preheated to 60°C before filling it in a cylindrical aluminium mould (sample holder). The mould itself was preheated to 75°C and equipped with an FBG sensor. To make the mould non-adherent for tests under unconstrained conditions it was covered with a thin layer of silicon oil. For constrained tests, the mould surface was roughened in order to enhance the surface to which the EP could adhere. The mould was 25 mm in diameter and ca. 25 mm in height and contained about 20 ml of the curing EP resin system. The EP was cured under isothermal condition of 75°C for 1000 min.

2.3. Fibre Bragg Grating sensing principle

For vertical strain measurements the FBG sensor was placed along the centre axis of the cylinder in the middle of the mould cavity. Horizontal measurements were realized by placing an FBG sensor at half of the height of the cylinder perpendicular to the longitudinal axis. The setup for both FBG assemblies can be seen in Figure 2.

A broad spectrum incident light with a central wavelength of 1549 nm was guided along the glass fibre. The back-reflected wavelength from the Bragg Gratings was detected by an optical spectrum analyzer and transmitted to an evaluating processor unit. To consider the influence of temperature shifts on the strain signal, the actual temperature was measured by a thermocouple in the sample next to the FBG sensor. This contribution to the detected strain signal was eliminated in all the investigated strain signals.

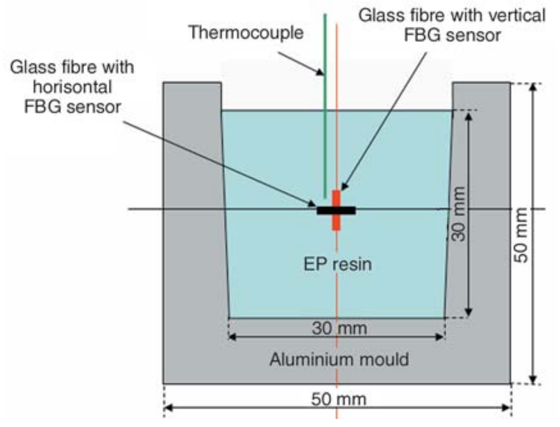

Figure 2. Setup of EP in an aluminium mould with embedded FBG sensors (vertical and horizontal)

2.4. Rheological measurement

To determine the gel point of the EP, a rheological measurement was performed on a Haake RS 1 (Thermo Electron, Karlsruhe) rheometer equipped with a thermocontroller TCP/P using 60 mm diameter parallel plates with a gap of 0.5 mm. The experiment was carried out under oscillatory conditions applying an angular frequency of 10 rad s^{-1} and an amplitude of 5%. The EP to be cured was placed into the preheated device and cured isothermally at 75°C for 190 minutes. The courses of the storage (G') and loss (G'') moduli were recorded as a function of the reaction time. The gel time was determined at the crossover of G' and G''.

3. Results

Strain signals in vertical (along the cylinder axis) and horizontal direction of the mould are investigated under constrained and unconstrained condition for isothermal cure of 1000 min at 75°C. Whereas under non-adhering condition the material undergoes a free-shrinking process, adhesion to the mould wall prevents the unhindered contraction of the EP. This is due to chemical bonding and/or mechanical 'anchoring' of the EP to the mould wall. The latter should result in inner stresses, and in worst case, even in material cracking. The stress field can be made viewable under polarized light. Polarized light microscopic pictures taken for adhering and non-adhering conditions are shown in Figure 3.

Under constrained condition (Figure 3a) the isochromates indicate the imposed stress levels quali-

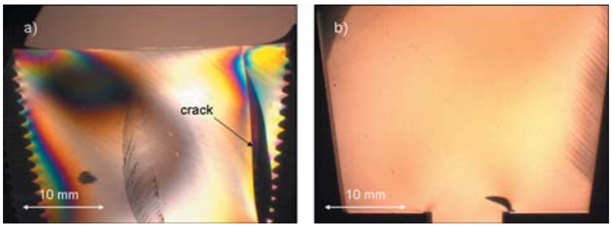

Figure 3. Sections of the EP moldings viewed under polarized light after curing with (a) and without (b) adhesion to the mould wall

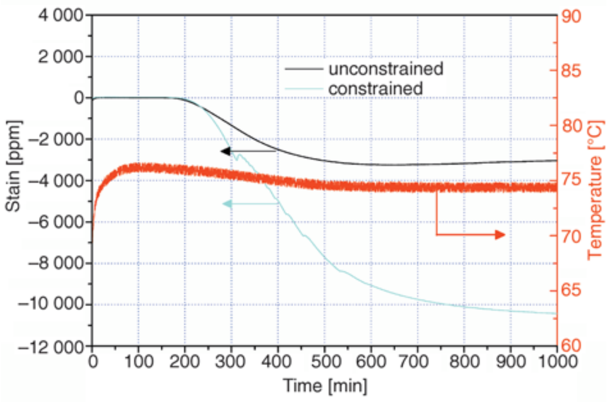

Figure 4. Strain development in the EP in vertical direction under constrained and unconstrained condition. Note that this figure contains also the related temperature-time trace

tatively – cf. colored regions. Note that on the right hand side of the moulding (arrow shows) the prevailing stresses produced a large crack. On the other hand free-shrinking condition resulted in a cured stress-free material, which can be seen in the non-coloured section of the EP molding in Figure 3b.

Strain development (strain-time curves) for the curing EP under constrained and unconstrained condition along the cylinder axis (vertical) was measured and shown together with the actual temperature in Figure 4.

As already discussed in our earlier works [8, 9], at the beginning no strain signal could be detected because the curing EP was in liquid form and the cure shrinkage was relieved by liquid flow. After about 170 minutes the FBG sensor detects a strain signal for the first time. This point was assigned to the gel point of the EP where the incipient formation of a material with infinite molecular weight occurs. The gel time of the EP resin at 75°C was also deduced from the rheological measurement. The results are shown in Figure 5 where *G′* and *G″* are plotted against time.

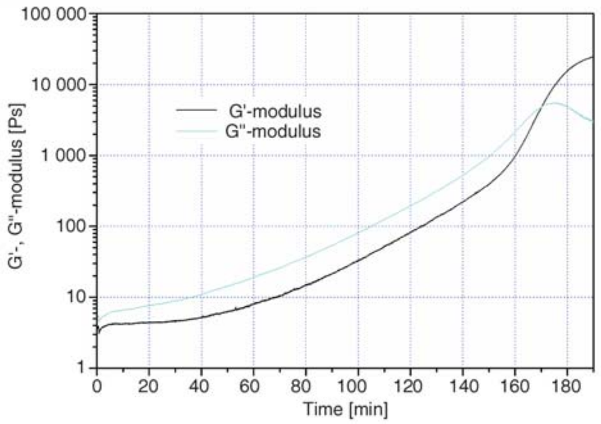

Figure 5. Reological measurement of storage (*G′*) and loss (*G″*) shear moduli of the EP as a function of time under isothermal condition of 75°C

Gelling is defined when the G′- and G″- shear moduli are equal. As can be seen in Figure 4 this occurs after about 170 minutes. The rheology result is in very good accordance with the first strain detection by the FBG sensing technique. After gelation an almost linear build-up of compressive strain took place before tending to flatten (cf. Figure 4). This is due to the advanced crosslinking of the EP. After about 380 minutes the first deviation of the linear decreasing strain line was found to represent the vitrification of the curing EP. This was proven by differential scanning calorimetry measurements, as disclosed in our earlier reports [8, 9]. Vitrification indicates the transformation from a rubbery to a glassy material and it occurs when the glass transition temperature T_g of the curing material equals the isothermal curing temperature.

Under the non-adhering condition, at the end of the isothermal curing, a released strain of about 3040 ppm was detected. In case of adhesion to the mould wall the strain signal indicated 10 430 ppm of compressive strain (cf. Figure 4). Because the adhesion to the wall is known to hinder the free-shrinkage of the EP, it is reasonable that the released strain is higher under constrained than under free-shrinking condition. Recall that for the reported measurements the FBG sensor was placed vertically in the EP resin. During crosslinking the EP contracts but radial shrinkage (i.e. horizontal) movements of the curing EP are prevented because the resin is ‘fixed’ to the wall. So the material flux occurs only in vertical direction where the surface is open (cf. Figure 2) and, thus, material ‘movement’ is possible. Correspondingly, higher compressive strain should be detectable by the FBG sensor in vertical than in horizontal direction. We suppose that the detected vertical strain under adhering condition is about three times higher than under free-shrinking condition. This is because the volume shrinkage is substituted by linear shrinkage which should contain the contribution of shrinkage of the two plane directions, as well as, the vertical contribution. In order to affirm the above speculation on the strain differences in horizontal and vertical directions the strain signal of the curing EP under adhering condition was measured simultane-

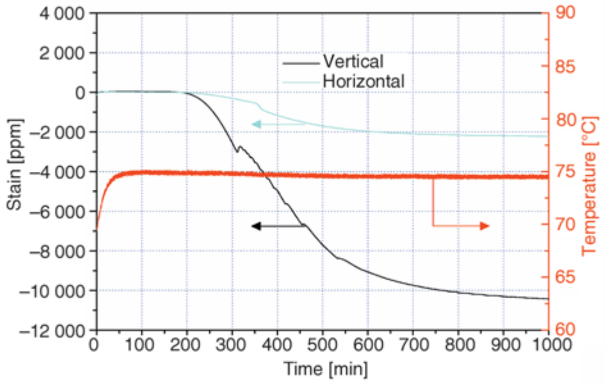

Figure 6. Strain development in the EP in vertical and horizontal directions under constrained condition. Note that this figure contains also the related temperature-time trace

ously in both, longitudinal and vertical directions (cf. Figure 6).

As can be seen in Figure 6, released strain after 1000 minutes is much lower in horizontal direction, viz. about 2230 ppm, compared to the vertical direction, which indicates 10 430 ppm. The adhesion to the mould wall prevents the build-up of strong compression stresses on the horizontal FBG sensor. Nevertheless, the small FBG signal indicates that even in this direction moderate compressive stress works due to the chemical reaction-induced shrinkage. This, in fact, induces stresses in the curing material as shown qualitatively in Figure 3. A final confirmation on the reliability of strain detection under constrained and unconstrained condition can be received by the investigation of the vertical and horizontal strain development under free-shrinking condition. The corresponding strain signals, as well as the measured temperature as a function of time are shown in Figure 7.

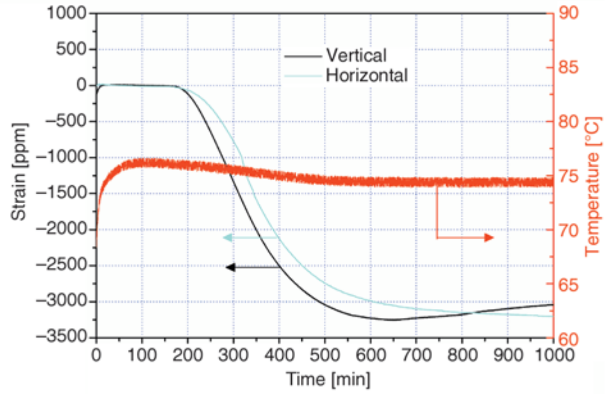

Figure 7. Strain development of the EP in vertical and horizontal directions under unconstrained condition. Note that this figure contains also the related temperature -time trace.

Table 1. Released strain in the EP after isothermal cure at 75°C for 1000 minutes

Adhesion condition	**Constrained**		**Unconstrained**	
Direction	vertical	horizontal	vertical	horizontal
Released strain [ppm]	10 430	2230	3040	3200

Apparently, the investigated strain signals in vertical and horizontal directions show almost the same results with a released strain of about 3000 ppm at the end of the experiment. The curing EP shrunk isotropically and, thus, there was practically no difference in the strain signals between vertical and horizontal FBG measurements. Whereas the vertical direction is favoured for material's movement for cure under constrained condition (c.f. Figure 6) in the present set-up, non-adhering cure conditions lead to an isotropic compression (c.f. Figure 7) due to cure-shrinkage.

The entire results of the released strain in horizontal and vertical direction after curing the EP for 1000 minutes isothermally at 75°C under constrained and unconstrained condition are summarized in Table 1.

4. Conclusions

The cure-induced strain development in a highly filled, anhydride hardened epoxy (EP) system was investigated by considering the adhesion to the moulding wall. FBG sensors were embedded vertically and horizontally in a cylindrical aluminium mould, which was made adhering (constrained) or non-adhering (unconstrained) to the EP resin. Unconstrained condition resulted in a free shrinkage of the curing EP in all directions, whereas adhesion to the mould wall prevented the unhindered contraction of the material during crosslinking. In the latter case the EP could flow only in vertical direction owing to the open surface of the mould in our setup. The strain values were the highest under constrained condition in vertical direction (10 430 ppm) which was the preferred flow direction. Note that the lateral (horizontal) movement of the curing material was restricted under constrained conditions leading to a small value of released strain (2230 ppm). By contrast, curing under free-shrinking condition (i.e. in case of a non-adhering mould wall) resulted in almost equal horizontal (3200 ppm) and vertical (3040 ppm) strain signals since isotropic shrinking was afforded. In all cases first strain appearance measured by the FBG was found to agree very well with the known determination of gel point by rheological measurement. The residual stresses in the cured moldings were made visible by taking polarized light microscopic images from sections of the samples.

References

[1] Wang H., Ogin S. L., Thorne A. M., Reed G. T.: Interaction between optical fibre sensors and matrix cracks in cross-ply GFRP laminates. Part 2: Crack detection. Composites Science and Technology, **66**, 2367–2378 (2006).

[2] Ling H. Y., Lau K. T., Cheng L., Su Z.: Mode II fracture behaviour monitoring for composite laminates using embedded fibre Bragg grating sensor. Composite Structures, **76**, 88–93 (2006).

[3] Lau K. T., Yuan L., Zhou L. M., Xu J., Woo C. H.: Strain monitoring in FRP laminates and concrete beams using FBG sensors. Composite Structures, **51**, 9–20 (2001).

[4] Murukeshan V. M., Chan P. Y., Ong L. S., Seah L. K.: Cure monitoring of smart composites using fiber Bragg grating based embedded sensors. Sensors and Actuators, **79**, 153–161 (2000).

[5] Botsis J., Humbert L., Colpo F., Giaccari P.: Embedded fiber Bragg grating sensor for internal strain measurements in polymeric materials. Optics and Lasers in Engineering, **43**, 491–510 (2005).

[6] Yashiro S., Okabe T., Takeda N.: Damage identification in a holed CFRP laminate using a chirped fiber Bragg grating sensor, Composites Science and Technology, **67**, 286–295 (2007).

[7] Okabe Y., Yashiro S., Tsuji R., Mizutani T., Takeda N.: Effect of thermal residual stress on the reflection spectrum from fiber Bragg grating sensors embedded in CFPR laminates. Composites: Part A, **33**, 991–999 (2002).

[8] Harsch M., Karger-Kocsis J., Herzog F.: Influence of cure regime on the strain development in an epoxy resin as monitored by fibre Bragg grating (FBG) sensor. Macromolecular Materials and Engineering, in press (2007).

[9] Harsch M., Karger-Kocsis J. Herzog F.: Monitoring of cure-induced strain of an epoxy resin by fibre Bragg grating sensor. Journal of Applied Polymer Science, submitted (2007).

[10] Colpo F., Humbert L., Giaccari P., Botsis J.: Characterization of residual strains in an epoxy block using an embedded FBG sensor and the OLCR technique. Composites: Part A, **37**, 652–661 (2006).

[11] Leng J. S., Asundi A.: Real-time cure monitoring of smart composite materials using extrinsic Fabry-Perot interferometer and fiber Bragg grating sensors. Smart Material Structures, **11**, 249–255 (2002).

[12] Quintero S. M. M., Quirino W. G., Triques A. L. C., Valente L. C. G., Braga A. M. B., Achete C. A., Cremona M.: Thin film stress measurements by fiber optic strain gage. Thin Solid Films, **494**, 141–145 (2006).

[13] O'Dwyer M. J., Maistros G. M., James S. W., Tatam R. P., Partridge I. K.: Relating the state of cure to the real-time internal strain development in a curing composite using in-fibre Bragg gratings and dielectric sensors. Measurement Science and Technology, **9**, 1153–1158 (1998).

[14] Chehura E., Skordos A. A., Ye C-C., James S. W., Partridge I. K., Tatam R. P.: Strain development in curing epoxy resin and glass fibre/epoxy composites monitored by fibre Bragg grating sensors in birefringent optical fibre. Smart Material Structures, **14**, 354–362 (2005).

[15] Dawood T. A., Shenoi R. A., Sahin M.: A procedure to embed fibre Bragg grating strain sensors into GFRP sandwich structures. Composites: Part A, **38**, 217–226 (2007).

[16] Cusano A., Breglio G., Giordano M., Calabro A., Cutolo A., Nicolais L.: Optoelectronic characterization of the curing process of thermoset-based composites. Journal of Optics A: Pure and Applied Optics, **3**, 126–130 (2001).

[17] Giordano M., Laudati A., Nasser J., Nicolais L., Cusano A., Cutolo A.: Monitoring by a single fiber Bragg grating of the process induced chemo-physical transformations of a model thermoset. Sensors and Actuators A, **113**, 166–173 (2004).

[18] Antonucci V., Cusano A., Giordano M., Nasser J., Nicolais L.: Cure-induced residual strain build-up in a thermoset resin. Composites: Part A, **37**, 592–601 (2006).

[19] Antonucci V., Giordano M., Cusano A., Nasser J., Nicolais L.: Real time monitoring of cure and gelification of a thermoset matrix. Composites Science Technology, **66**, 3273–3280 (2006).

[20] Othonos A., Kalli K.: Fiber Bragg Gratings. Artech House, London (1999).

eXPRESS Polymer Letters Vol.1, No.4 (2007) 232–235
Available online at www.expresspolymlett.com
DOI: 10.3144/expresspolymlett.2007.35

Effect of the initiator on thermosensitive rate of poly(*N*-isopropylacrylamide) hydrogels

X. C. Xiao[*]

School of Life Sciences, South-Central University for Nationalities, Wuhan, 430074, China

Received 28 January 2007; accepted in revised form 1 April 2007

Abstract. As the main of thermosensitive polymeric materials, poly(*N*-isopropylacrylamide) (PNIPAM) undergoes volume changes in response to external temperature changes. While in some potential applications, a fast response rate is needed. In this article, effect of the initiator on thermosensitivity of PNIPAM hydrogels was carried out. The characterization of the resulting hydrogels was gravimetrically measured, and the result displays that with increasing the initiator dosage, much faster deswelling rate and much faster shrinking/swelling dynamic response are obtained.

Keywords: *polymer gels, fast response, initiator, thermosensitivity*

1. Introduction

Environmental stimuli-sensitive polymeric hydrogels, which exhibit volume or phase transitions in response to slight environmental changes, such as temperature, pH, ionic strength, light, electric and magnetic fields, etc., have attracted a widespread interest in the past thirty years due to their potential applications in numerous fields, including drug delivery [1–3], chemical separations [4, 5], sensors [6–8], catalysis [9], enzyme and cell immobilization [10]. Because there are many cases in which environmental temperature fluctuations occur naturally, and in which the environmental temperature stimuli can be easily designed and artificially controlled, in recent years much attention has been focused on thermosensitive gels [11, 12].

As a typical temperature-sensitive hydrogel, poly(*N*-isopropylacrylamide) (PNIPAM) hydrogel undergoes a dramatic reversible volume change at lower critical solution temperature (LCST, about 32°C) [13], which is the result of rather complex polarity of this molecule. Below the LCST, the amide functionality binds water molecules via hydrogen bonding, thus imparting both water solubility and surface activity. However, moving above the transition temperature breaks these hydrogen bonds, and the polymer expels water molecules and undergoes a coil-to-globule transition, thereby precipitating and forming particles. Its LCST close to physiological temperature makes the polymer an especially good candidate for applications in biotechnology and in medicine [14–16].

In some practical applications, such as "smart" actuators and on-off switches, a fast response is needed, while the normal-type PNIPAM gel cannot successfully satisfy this requirement. To increase the response dynamics, several strategies have been explored [17–22]. In this paper, we wish to present a novel method for the preparation of a fast deswelling PNIPAM hydrogels by changing initiator dosage. The result displays that with increasing the initiator dosage, much faster deswelling rate and much faster shrinking/swelling dynamic response are obtained.

---

[*]Corresponding author, e-mail: xcxiao71@yahoo.com.cn
© BME-PT and GTE

2. Experimental

2.1. Materials

The *N*-isopropylacrylamide (NIPAM) was kindly provided by Kohjin Co., Ltd., Japan, and was used after purifying by recrystallization in hexane and acetone and then drying in vacuo at room temperature. The initiator ammonium persulfate (APS), the accelerator *N*,*N*,*N*',*N*'-tetramethylethylenediamine (TMEDA), and the crosslinker *N*,*N*'-methylenebisacrylamide (MBA) were of analytical grade and used as received without any further purification. Double-distilled water was used in all the synthesis processes.

2.2. Preparation of the hydrogels

NIPAM, MBA and APS were first dissolved in 4 ml of double-distilled water to form a monomer solution and the free radical polymerization was carried out in a glass bottle of 30 mm in internal diameter at room temperature. After mild shaking for a few minutes, 120 μl of TMEDA were added into the monomer solution to initiate the radical polymerization. The polymerizations were continued in water for 4 h. After the polymerization, the prepared hydrogel was immersed in double-distilled water at room temperature for at least 48 h and the water was regularly refreshed in order to remove unreacted compounds. After freeze-drying, all hydrogels were cut into disc-like pieces approximately 6 mm in diameter and 4 mm in thickness for the following studies. The feed composition of monomer and other agents are listed in Table 1.

Table 1. Feed composition for the preparation of PNIPAM gels

Sample code	Composition			
	NIPAM [g]	MBA [mg]	Water [ml]	Initiator [g]
A	0.4	8	4	0.08
B	0.4	8	4	0.12
C	0.4	8	4	0.16

2.3. Measurement of swelling ratio of hydrogels

For the equilibrium swelling ratio (SR) study, PNIPAM hydrogels were swollen in double-distilled water in the temperature range from 21°C to 45°C, which covers the expected range of LCST of the PNIPAM hydrogels. The gravimetric method was employed to study the hydrogels' swelling ratio. After soaking into distilled water at each testing temperature for at least 8 h, the hydrogels samples were removed and blotted with wet filter paper to remove excess water on the hydrogels surface and weighed. After measurement at one temperature, the hydrogels were re-equilibrated at another predetermined temperature for subsequent swelling ratio measurement. The average values among three measurements were taken for each sample and the equilibrium swelling ratio was calculated as Equation (1):

$$\text{Swelling ratio}\,(\text{SR}) = \frac{W_t - W_d}{W_d} \qquad (1)$$

where W_t is the weight of the hydrogels at each testing temperature and W_d is the dry weight of hydrogels after drying in vacuum.

2.4. Measurement of the oscillatory shrinking-swelling kinetics of hydrogels

To detect hydrogels with a fast response, the oscillatory shrinking-swelling kinetics of the prepared hydrogels over the 6 min temperature cycles between 26°C (below LCST) and 40°C (above LCST) in double-distilled water were examined gravimetrically. Water retention of wet hydrogel was defined as Equation (2):

$$\text{Water retentio} = \frac{W_t - W_d}{W_{t0} - W_d} \cdot 100 \qquad (2)$$

where W_{t0} is the weight of the swollen hydrogel at a predetermined time at 26°C and other terms are the same as defined above in the swelling ratio.

3. Results and discussion

3.1. Swelling ratio of PNIPAM hydrogels

Figure 1 shows the equilibrium swelling ratios of hydrogels as a function of the external temperature. As can be seen from Figure 1, when the temperature increased, all hydrogels exhibited a similar temperature-dependence that lost water and shrank in volume and it is clear that LCSTs of hydrogels lie in the vicinity of 32°C. At the temperature below the LCST, these hydrogels absorb water and become swollen. The SRs of the resulting hydrogels increase with increasing the initiator dosage.

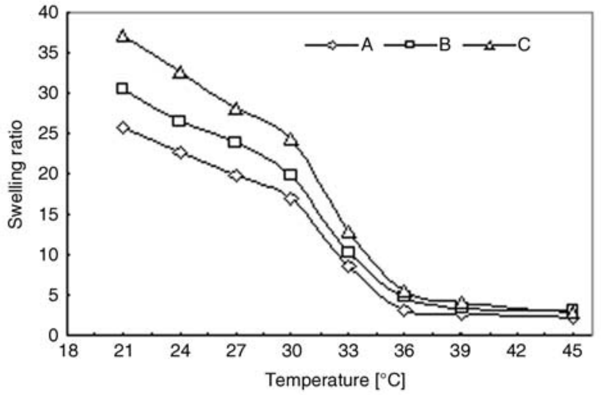

Figure 1. Temperature dependence of the SR of PNIPAM gels in the temperature range from 21°C to 45°C. The sample code is defined in Table 1

When transitions occur, the SR of sample C decreases more sharply and the phase-separation degree (changes of SR versus temperature changes around LCST) is the greatest, which demonstrates that the response rate to temperature changes of this PNIPAM hydrogel is the fastest.

3.2. The oscillatory shrinking-swelling kinetics of PNIPAM hydrogels

Figure 2 displays the oscillatory shrinking-swelling kinetics of hydrogels prepared with different the initiator dosages over the 6 min temperature cycles between 26°C (below LCST) and 40°C (above LCST) in double-distilled water. This 6 min cycle was continued for a total 6 cycles (72 min) in order to determine response of hydrogels to temperature. It is found that, although all hydrogels exhibited an oscillatory shrinking-swelling character upon cycling temperature between 26°C and 40°C and their shrinking and swelling cycles are accompanied by a consecutive reduction in water content, much more rapid, sharp and larger magnitude shrinking-swelling changes were exhibited with increasing the initiator dosage.

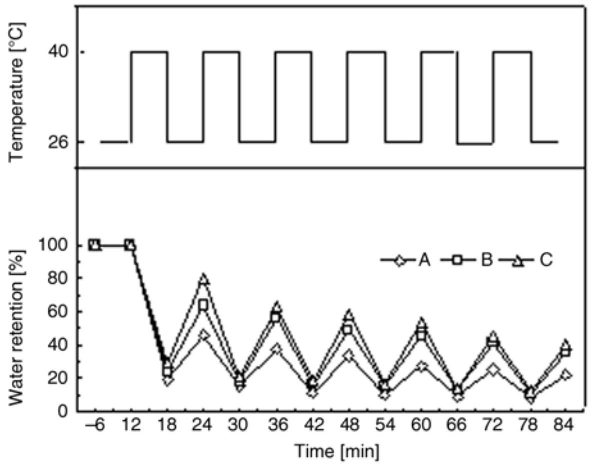

Figure 2. Oscillatory shrinking–swelling kinetics for hydrogels prepared with different initiator dosage over 6 min temperature cycles in double-distilled water between 26 and 40°C. The sample code is defined in Table 1

As redox initiator, the system APS/TMEDA can offer free radical, in which TMEDA accelerates a homolytic cleavage on moieties of APS, therefore they play a important role in the vinyl polymerization. The terminal groups of the hydrogels prepared by this polymerization are hydroxy groups (–OH) resulting from cleavage of persulfate initiator [23, 24]. So the content of hydrophilic group (–OH) increases with increasing the initiator dosage. For traditional PNIPAM hydrogels, there is a hydrophilic and hydrophobic balance of polymer side groups, i. e., –CONH– is hydrophilic and $–CH(CH_3)_2$ is hydrophobic [11]. This balance is broken by the addition of –OH and the final percentages of hydrophilic groups increase with increasing the content of –OH. The resulting polymer chains get more widely expanded in the aqueous media with increasing the initiator dosage. Moreover increasing the initiator concentration affects both the chain length and the crosslinking density of the gels. The dangling chains can increase response rate of hydrogels [17, 18]. Both lead to the larger SR of hydrogels and much faster speed to absorb water at temperature below the LCST. So it is easy to understand hydrogels exhibits faster deswelling rate.

4. Conclusions

To prepare poly(*N*-isopropylacrylamide) hydrogel with fast response rate, effect of the initiator on thermosensitivity of PNIPAM hydrogel was carried out in this article. The characterization of the final hydrogel was gravimetrically measured, and the result displays that much faster deswelling rate and much faster shrinking/swelling dynamic response are obtained with increasing the initiator dosage, owing to increase of –OH that derived from the system APS/TMEDA.

Acknowledgements

This work was financially supported by South-Central University For Nationalities (YZZ06002). The author gratefully acknowledges the help of the Kohjin Co., Ltd, Japan, for kindly supplying the *N*-isopropylacrylamide.

References

[1] Kwon I. C., Bae Y. H., Kim S. W.: Electrically credible polymer gel for controlled release of drugs. Nature, **354**, 291–293 (1991).

[2] Jeong B., Bae Y. H., Lee D. S., Kim S. W.: Biodegradable block copolymers as injectable drug-delivery systems. Nature, **388**, 860–862 (1997).

[3] Murthy N., Thng Y. X., Schuck S., Xu M. C., Frechet J. M.: A novel strategy for encapsulation and release of proteins: hydrogels and microgels with acid-labile acetal cross-linkers. Journal of the American Chemical Society, **124**, 12398–12399 (2002).

[4] Kawaguchi H., Fujimoto K.: Smart latexes for bioseparation. Bioseparation, **7**, 253–258 (1998).

[5] Kondo A., Kaneko T., Higashitani K.: Development and application of thermo-sensitive immunmicrospheres for antibody purification. Biotechnology and Bioengineering, **44**, 1–6 (1994).

[6] Hu Z. B., Chen Y. Y., Wang C. J., Zheng Y. D., Li Y.: Polymer gels with engineered environmentally responsive surface patterns. Nature, **393**, 149–152 (1998).

[7] Panchapakesan B., DeVoe D. L., Widmaier M. R., Cavicchi R., Semancik S.: Nanoparticle engineering and control of tin oxide microstructures for chemical microsensor applications. Nanotechnology, **12**, 336–349 (2001).

[8] van der Linden H., Herber S., Olthuis W., Bergveld P.: Development of stimulus-sensitive hydrogels suitable for actuators and sensors in microanalytical devices. Sensors and Materials, **14**, 129–139 (2002).

[9] Bergbreiter D. E., Case B. L., Liu Y. S., Caraway J. W.: Poly(*N*-isopropylacrylamide) soluble polymer supports in catalysis and synthesis. Macromolecules, **31**, 6053–6062 (1998).

[10] Guiseppi-Elie A., Sheppard N. F., Brahim S., Narinesingh D.: Enzyme microgels in packed-bed bioreactors with downstream amperometric detection using microfabricated interdigitated microsensor electrode arrays. Biotechnology and Bioengineering, **75**, 475–484 (2001).

[11] Xiao X. C., Chu L. Y., Chen W. M., Wang S., Li Y.: Positively thermo-sensitive monodisperse core-shell microspheres. Advanced Functional Materials, **13**, 847–852 (2003).

[12] Xiao X. C., Chu L. Y., Chen W. M., Wang S., Xie R.: Preparation of submicrometer-sized monodispersed thermoresponsive core-shell hydrogel microspheres. Langmuir, **20**, 5247–5253 (2004).

[13] Pelton R.: Temperature-sensitive aqueous microgels. Advances in Colloid and Interface Science, **85**, 1–33 (2000).

[14] Jeong B., Kim S. W., Bae Y. H.: Thermosensitive sol-gel reversible hydrogels. Advanced Drug Delivery Reviews, **54**, 37–51 (2002).

[15] Okano T., Yamada N., Okuhara M., Sakai H., Sakurai Y.: Mechanism of cell detachment from temperature-modulated, hydrophilic-hydrophobic polymer surfaces. Biomaterials, **16**, 297–303 (1995).

[16] Liang D., Zhou S., Song L., Zaitsev V. S., Chu B.: Copolymers of poly(*N*-isopropylacrylamide) densely grafted with poly(ethylene oxide) as high-performance separation matrix of DNA. Macromolecules, **32**, 6326–6333 (1999).

[17] Kaneko Y., Sakai K., Kikuchi A., Yoshida R., Sakurai Y., Okano T.: Influence of freely mobile grafted chain length on dynamic properties of comb-type grafted poly(*N*-isopropylacrylamide) hydrogels. Macromolecules, **28**, 7717–7723 (1995).

[18] Yoshida R., Uchida K., Kaneko Y., Sakai K., Kikuchi A., Sakurai Y., Okano T.: Comb-type grafted hydrogels with rapid de-swelling response to temperature change. Nature, **374**, 240–242 (1995).

[19] Nakamoto C., Motonaga T., Shibayama M.: Preparation pressure dependence of structure inhomogeneities and dynamic fluctuations in poly(*N*-isopropylacrylamide) gels. Macromolecules, **34**, 911–917 (2001)

[20] Chen J., Park H., Park K.: Synthesis of superporous hydrogels: hydrogels with fast swelling and superabsorbent properties. Journal of Biomedical Materials Research, **44**, 53–62 (1999).

[21] Zhang X. Z., Zhuo R. X., Yang Y. Y.: Using mixed solvent to synthesize temperature sensitive poly(*N*-isopropylacrylamide) gel with rapid dynamics properties. Biomaterials, **23**, 1313–1318 (2002).

[22] Kabra B. G., Gehrke S. H.: Synthesis of fast response, temperature-sensitive poly(*N*-isopropylacrylamide) gel. Polymer Communications, **32**, 322–323 (1991).

[23] Feng X. D., Guo X. Q., Qiu K. Y.: Study of the initiation mechanism of the vinyl polymerization with the system persulfate/*N*,*N*,*N*',*N*'-tetramethylethylenediamin. Die Makromolekulare Chemie, **189**, 77–83 (1988).

[24] Guilherme M. R., da Silva R., Rubira A. F., Geuskens G., Muniz E. C.: Thermo-sensitive hydrogels membranes from PAAm networks and entangled PNIPAAm: effect of temperature, cross-linking and PNIPAAm contents on the water uptake and permeability. Reactive & Functional Polymers, **61**, 233–243 (2004).

eXPRESS Polymer Letters Vol.1, No.4 (2007) 236–244
Available online at www.expresspolymlett.com
DOI: 10.3144/expresspolymlett.2007.36

Elimination of the reactivation process in the adhesion of chlorinated SBS rubber with polychloroprene adhesives

M. V. Navarro-Bañón, M. M. Pastor-Blas, J. M. Martín-Martínez*

Department of Inorganic Chemistry, University of Alicante, 03080 Alicante, Spain

Received 12 January 2007; accepted in revised form 3 April 2007

Abstract. Chlorination treatment of a thermoplastic styrene-butadiene-styrene rubber (SBS) with a 3 wt% solution of trichloroisocyanuric acid (TCI) in methyl ethyl ketone (MEK) introduces chlorinated and oxidized moieties on the rubber surface which increase its surface energy and produces surface microroughness. Consequently adhesion properties, evaluated by T-peel strength measurements in chlorinated SBS/solvent based-polyurethane adhesive/leather joints, are enhanced. In this study, two solvent-based polychloroprene adhesives (PCP0 and PCP30R) have been considered as an alternative to the commonly used solvent-based polyurethane adhesive (PU). A thermoreactive phenolic resin was added to one of the polychloroprene adhesive formulations (PCP30R). This tackifier resin favors chlorination of the adhesive and reinforces the interface between the chlorinated adhesive and the chlorinated rubber surface. Besides, PCP30R adhesive does not need adhesive reactivation and considerable high T-peel strength value (5.7±0.3 kN/m) was obtained. Elimination of the reactivation process implies a considerable improvement of the manufacturing process in the footwear industry.

Keywords: *rubber, SBS rubber, surface treatment, polychloroprene, polyurethane*

1. Introduction

Styrene-butadiene-styrene thermoplastic rubbers (SBS) are commonly used in the footwear industry as sole materials. Their non polar nature imparts poor adhesion properties to these rubbers, thus a surface treatment is required prior to adhesive joint formation [1, 2]. Halogenation with trichloroisocyanuric acid (TCI) solutions in organic solvents (ketones or esters) is the most widely used surface treatment for rubber soles in the footwear industry [3]. This treatment creates chlorinated and oxygenated species and imparts roughness to the rubber surface. Consequently, appropriate rubber-leather joints with a good performance are obtained when using a polyurethane adhesive [4, 5].

Once applied upon the treated rubber surface and the leather, the solvent of the polyurethane adhesive is allowed to evaporate for 1 hour. Then, the dry polyurethane adhesive film needs to be melted under infrared irradiation (adhesive reactivation) in order to permit fluency of polyurethane chains, prior to the adhesive joint formation. This adhesive reactivation is a time consuming process and the temperature needs to be carefully controlled [6]. Polychloroprene adhesives do not need reactivation after solvent evaporation, as polychloroprene adhesive tack is maintained for a longer time (i. e. open time), compared to polyurethane adhesives. However, incompatibility between polychloroprene and the chlorinated species introduced on the rubber surface by the halogenating treatment is believed to be responsible for their often lack of adhesion, although this has not been demonstrated in the literature [6]. Thus, the aim of this study is to modify the formulation of the polychloroprene adhesive in order to achieve good adhesion properties with a chlorinated SBS rubber. The possible elimination of the reactivation process from the

---

*Corresponding author, e-mail: mercedes.pastor@ua.es
© BME-PT and GTE

adhesive joint formation will be considered and the interactions produced between the polychloroprene and the chlorinated rubber will be analyzed.

2. Experimental

2.1. Materials

The thermoplastic styrene-butadiene-styrene (SBS) rubber used in this study was obtained from Kraton D-4270CS pellets, an oil-extended (45 phr non-staining paraffin oil) radial block SBS copolymer. The SBS rubber test samples (25 mm width, 150 mm length, 3 mm thick) were prepared by Synthelast, S.A. (Elche, Alicante, Spain) by injection molding in a heated mold (150°C) and contain 10 wt% calcium carbonate as filler and 0.3 wt% phenolic antioxidant.

The surface of the SBS rubber was treated with methyl ethyl ketone (MEK) solutions containing 3 wt% trichloroisocyanuric acid (TCI) (98 wt% purity, Merck): 3 wt% TCI/MEK. The solution was brushed on the SBS rubber surfaces and allowed to react at room temperature in air for one hour.

Adhesive strengths were evaluated from T-peel tests on joints produced between the surface chlorinated SBS rubber and roughened leather using two different polychloroprene adhesives. Both polychloroprene adhesives were formulated with the same base polymer (DENKA A-90) but PCP0 did not contain any resin and PCP30R was formulated with 30 phr (parts per hundred) of a thermoreactive phenolic resin (SP-154) provided by Shenectady Europe (SI Group, Béthune, France) [7]. Table 1 shows the formulations of the two polychloroprene adhesives. To prepare the PCP30R polychloroprene adhesive solution the resin and the metallic oxides were previously stirred in a laboratory mixer at 1000 rpm (revolutions per minute) for 30 minutes. After that, the polychloroprene was added and the solution was stirred at 2000 rpm for 1 hour, and later on at 2500 rpm for 3 more hours. To prepare the polychloroprene adhesive solution with no resin in its formulation (PCP0) all the ingredients were simultaneously mixed and stirred at 2000 rpm for 1 hour and at 2500 rpm for 2 hours.

Table 1. Formulation of polychloroprene adhesives PCP0 and PCP30R

Component [phr]	PCP0	PCP30R
PCP	100	100
MgO	–	4
ZnO	–	5
Antioxidant	2	2
Phenolic resin (SP154)	–	30
Solvents	333	431
H_2O	–	2

PCP: DENKA A-90
ZnO: ZINKOXYD AKTIV (Rubber Chemicals)
MgO: ANSCOR Q (Britmag)
Antioxidant: IRGANOX 1010 (Ciba)
Solvents: 45:20:35 (Hexane:toluene:acetone)

The results obtained with polychloroprene adhesives were compared with those obtained with a solvent-based polyurethane adhesive (PU). To prepare the solvent-based polyurethane adhesive solution polyurethane pellets (Desmocoll 540 provided by Bayer, Leverkusen, Germany) were added to MEK and stirred at 2000 rpm for 2 hours to obtain the adhesive solution.

Calf leather used in the adhesive joints was supplied by INESCOP (Elda, Alicante, Spain) (Tensile strength = 13 MPa; Elongation-at-break = 60%; ash content at 950°C less than 5 wt%).

2.2. Experimental techniques

2.2.1. Fourier transform infrared (FTIR) spectroscopy

The chemical modifications produced on the SBS rubber by treatment with 3 wt% TCI/MEK in about 3 μm depth were assessed by ATR-IR spectroscopy. A Bruker Tensor 27 FTIR spectrometer (Bruker Optik, Ettlingen, Germany) was used and a KRS-5 (thallium bromoiodide) crystal was employed. The angle of incidence of the IR beam was 45°, and 200 scans were collected and averaged with a resolution of 4 cm^{-1}.

2.2.2. X-Ray photoelectron spectroscopy (XPS)

XPS was used to determine the chemical composition on the outermost (5–10 nm) treated SBS surface. A VG Scientific Microtech Multilab spectrometer (VG Microtech, Hastings, E Sussex, UK) with a Mg Kα X-ray source (1253.6 eV) operating at 25 keV and 300 W, and a 45° take-off angle was used. Prior to analysis, the samples were placed in a vacuum chamber until a pressure lower than $1\cdot10^{-6}$ Pa was obtained. The analysis was performed on 5 mm×2 mm pieces of SBS rubber at a residual pressure lower than $1\cdot10^{-6}$ Pa. For each sample, a survey scan encompassing the region 0–1200 eV was first obtained. Multiplex scanning of all observed photopeaks in the survey scan were carried out in a 20 eV range. Binding energies of all photopeaks were referenced to the C 1s photopeak position for C–C and C–H (hydrocarbons) species at 285.0 eV. 1.8 eV was used as FWHM (Full Width at Half Maximum) for the C 1s photopeak. Atomic concentration calculations were carried out using a VGX900-W system.

2.2.3. Contact angle measurements

A Ramé Hart 100 goniometer (Ramé-Hart, Inc., Mountain Lakes, NJ, USA) was used to obtain the contact angle values on the treated SBS rubber surface. Prior to contact angle measurements, the treated SBS rubber surfaces were wiped with ethanol to remove organic contaminants and the solid by-product residues due to the chlorination treatment [8]. The treated SBS rubber pieces were placed into the thermostated chamber of the goniometer, which had previously been saturated with the vapour of the test liquid at 25°C for at least 10 minutes before placing 4 µl drops on the treated SBS rubber surface. The contact angles were measured 15 minutes after placing the drops. The test liquids used were bidistilled-deionized water and methane diiodide. The experimental error was ±2 degrees. Surface energy was evaluated from contact angle measurements using the Owends and Wendt approximation [9].

2.2.4. Scanning electron microscopy (SEM)

The morphological modifications produced on the treated SBS rubber surface were analyzed by SEM. An environmental scanning electron microscope HITACHI S-3000N (Hitachi Ltd, Tokyo, Japan) was used. The electron beam energy was 20 kV. The samples were gold coated to obtain sufficient contrast in the micrographs.

An EDX (Energy dispersive X-ray) analyzer coupled to the SEM instrument was used to monitor the chemical composition of the solid residues on the treated SBS rubber surfaces produced as a consequence of the chlorination treatment. For EDX analysis, the samples were not gold-coated.

2.2.5. Dynamical Mechanical Thermal Analysis (DMTA)

The mechanical and viscoelastic properties of the adhesives were assessed by dynamical-mechanical-thermal analysis using a Rheometric Scientific DMTA MK III equipment (Rheometric Scientific, Piscataway, New Jersey, NJ). The measurements were obtained in two points bending mode, using a frequency of 1 Hz and a strain amplitude between peaks of 32 µm. The temperature range was varied from –80°C to 80°C by using a heating rate of 5°C/min. Rectangular test sample pieces of (1.0–2.0 mm)×(10.0–20.0 mm)×(60.0–70.0 mm) were used in the measurements.

2.2.6. Differential Scanning Calorimetry (DSC)

Thermal properties of the adhesives were determined by Differential Scanning Calorimetry in a TA Instruments DSC Q100 V 6.2 equipment (TA Instruments, Barcelona, Spain). Samples of 10–20 mg were analyzed. The sample was introduced in an aluminium hermetic sample holder. Two heating runs were performed. The samples were initially heated from –80°C to 80°C at a heating rate of 10°C/min, then they were suddenly cooled down to –80°C, and after that, a second heating run (under the same experimental conditions) was carried out. The glass transition temperature (T_g) values were determined from the DSC curves obtained in the second heating run. This procedure was used to remove the thermal history of the sample.

2.2.7. T-peel tests

Adhesive joints between test pieces of chlorinated SBS rubber (150 mm×25 mm×7 mm) and roughened leather (150 mm×30 mm×3 mm) were produced using a solvent-based polyurethane adhesive (PU) and two polychloroprene adhesives (PCP0 and PCP30R). Before bonding, the leather surface was roughened in a Superlema (Superlema S.A., Zaragoza, Spain) roughening machine operating at 2800 rpm. A P100 aluminium oxide abrasive cloth was used and about 0.5 mm of leather were removed. Then, two consecutive adhesive coatings (the second coating was applied 10 minutes after applying the first one) were applied with a brush on the roughened leather surface. On the other hand, one hour after chlorination, the adhesive solution was applied by brushing on the treated SBS rubber surface. The adhesive was allowed to dry for 45 min at room temperature. In some cases, the dried solid adhesive film was melted at 80°C under infrared radiation (reactivation process) and immediately placed into contact under a pressure of 0.8 MPa for 10 seconds to achieve a suitable joint. To determine the adhesive strength values of the treated SBS rubber/polyurethane adhesive/roughened leather joints, an Instron 4411 (Instron Ltd., Buckinghamshire, United Kingdom) was used at a peel rate of 0.1 m/min. The adhesive joints were tested 72 hours after bond formation.

3. Results and discussion

3.1. Surface modifications introduced on the SBS rubber surface by the treatment with a 3 wt% TCI/MEK solution

The ATR-IR spectrum of the as-received SBS rubber (Figure 1) shows typical absorption bands from polybutadiene (C–H stretching at 2925 and 2850 cm^{-1}, –CH$_2$ scissoring at 1450 cm^{-1}, –CH$_2$ twisting at 1380 cm^{-1} and out of plane deformation of 1,4-trans C=C at 960 cm^{-1}) and from polystyrene (aromatic C–H stretching at 3010 cm^{-1}, aromatic C–C stretching at 1601 cm^{-1}, out of plane deformation of aromatic C–H at 910 and 700 cm^{-1}) units. There is also C–O–C bending absorption at 870 cm^{-1} of calcium carbonate in the rubber formulation. The treatment of the SBS rubber with a 3 wt% TCI/MEK solution introduces oxygenated (C=O stretching at 1700 cm^{-1}, C–H bending of –CH$_2$CO at 1400 cm^{-1} and C–O stretching at 1065 cm^{-1}) and chlorinated (C–H bending of –CH$_2$Cl at 1420 cm^{-1} and C–Cl stretching at 760 and 540 cm^{-1}) moieties on the rubber surface. Besides, a N–C=O stretching band appears at 1750 cm^{-1} (probably due to the TCI and/or isocyanuric acid crystals, reaction by-product between TCI and rubber, deposited on the treated rubber surface).

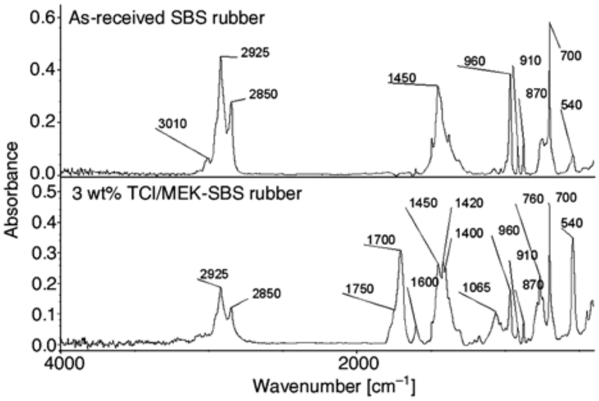

Figure 1. ATR-IR spectra of the as-received SBS rubber surface and SBS rubber surface treated with 3 wt% TCI/MEK

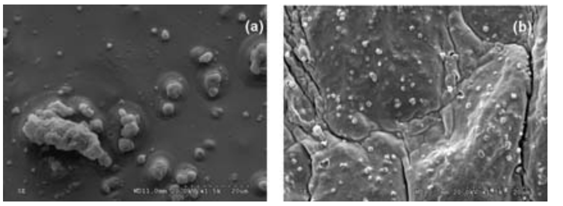

Figure 2. SEM micrographs of (a) as-received SBS rubber surface and (b) SBS rubber surface treated with 3 wt% TCI/MEK

SEM micrograph of as-received SBS rubber shows calcium carbonate particles (filler in the SBS rubber formulation) (Figure 2). The nature of these calcium carbonate particles was assessed by EDX analysis. Besides, the treatment of the SBS rubber surface with TCI/MEK partially dissolves the rubber surface and creates microcracks [10]. On the other hand, chlorinated SBS rubber shows not only calcium carbonate but also chlorine containing crystals, from unreacted TCI on the rubber surface. Considering that these TCI crystals may act as a weak boundary layer preventing contact of rubber surface with the adhesive, chlorinated rubber surfaces were wiped with absolute ethanol (95 wt%) 1 hour after chlorination treatment to remove unreacted TCI from the rubber surface [11]. After ethanol wiping, XPS analysis and contact angle measurements on SBS rubber surface were assessed.

The XPS analysis of the as-received rubber and rubber treated with TCI/MEK shows that the treatment with this chlorinating system introduces oxygen and chlorine on the rubber surface (Table 2a). On the other hand, some nitrogen is detected on the treated rubber surfaces, probably due to TCI or isocyanuric acid crystals deposited on the treated rubber surface, which has been previously detected by ATR-IR spectroscopy (Figure 1). C1s curve fitting (Table 2b) reveals the creation of C–O, C=O and C–Cl polar moieties on the chlorinated SBS rubber surface and also the presence of N–C=O from unreacted TCI and/or isocyanuric acid on the treated rubber surface.

The introduction of the oxygenated and chlorinated species on the SBS rubber surface by the treatment with TCI/MEK produced a decrease of contact angle (evaluated with bidistilled-deionized water and methane diiodide) and an increase of the rubber surface energy from 41.2 to 51.2 mJ/m^2, mainly

Table 2a. Elemental atomic percentages (XPS) obtained on the as-received SBS rubber surface and SBS rubber surfaces treated with TCI/MEK

	Atomic percentage		
	Binding energy [eV]	**As-received [at %]**	**Treated with TCI/MEK [at %]**
C1s	285.0	97.9	88.4
O1s	531.0	0.6	6.6
N1s	398.0	0.3	1.6
$Si2p_{3/2}$	99.0	0.6	–
$Zn2p_{3/2}$	1022.0	0.6	–
$Cl2p_{3/2}$	199.0	–	3.3
	O/C	0.01	0.07

Table 2b. Atomic percentages (XPS) of C1s curve fitting obtained on the as-received SBS rubber surface and SBS rubber surfaces treated with TCI/MEK

	Binding energy [eV]	As-received [at %]	3 wt% TCI/MEK [at %]
C–H,C–C	285.0	95.6	83.8
C–O, C–Cl	286.5	4.4 (C–O)	14.8 (C–O, C–Cl)
C=O, N–C=O	288.0	–	1.1
$RCOO^-$	288.9	–	0.3

Table 3. Contact angle measurements (bidistilled-deionized water and methane diiodide), total (γ_s), polar (γ_s^p) and dispersive (γ_s^d) components of the surface energy of as-received SBS rubber and SBS rubber treated with TCI/MEK

Adhesive	θH_2O [°]	θCH_2I_2 [°]	γ_s^d [mJ/m²]	γ_s^p [mJ/m²]	γ_s [mJ/m²]
As-received	88±2	37±1	40.0	1.2	41.2
3 wt% TCI/MEK	62±1	51±1	40.5	10.7	51.2

due to the increase of its polar component (from 1.2 mJ/m² to 10.7 mJ/m²) (Table 3).

3.2. Adhesion properties of the chlorinated SBS rubber with polyurethane and polychloroprene adhesives

3.2.1. Characterization of the Polyurethane and Polychloroprene adhesives

Three different adhesives were considered in this study: a polyurethane adhesive (PU) with a % solid content of 17.2±0.1 and two polychloroprene adhesives: PCP0 (23.4±0.2% solid content) and PCP30R (26.3±0.3% solid content). Brookfield viscosities of these adhesives were 2865±60, 11710±90 and 4180±60 mPa·s, respectively.

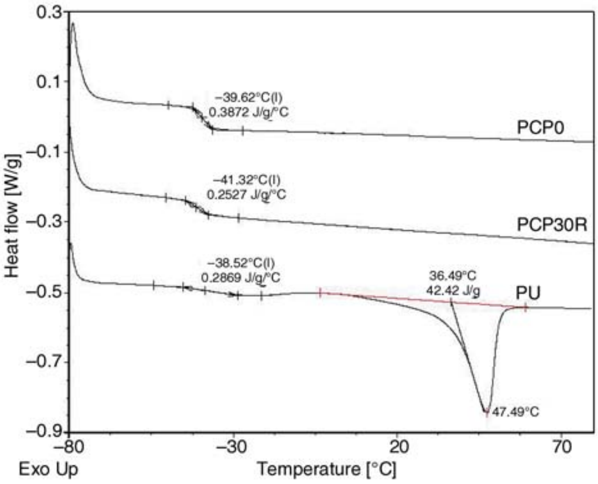

Figure 3. DSC thermograms of PU, PCP0 and PCP30R adhesives

Thermal properties of the PU, PCP0 and PCP30R adhesives were characterized by DSC. In the thermograms (Figure 3) obtained from the second thermal run of polychloroprene adhesives a melting peak does not appear, indicating that the crystallization of the polychloroprene adhesives is slower than the polyurethane crystallization. Thus, the open time of polychloroprene adhesives (time when tack properties are maintained) is higher than that of the polyurethane adhesive. For this reason, the adhesive joints formation with polychloroprene adhesives may not require the adhesive heat reactivation. On the other hand, the T_g values obtained for the PU, PCP0 and PCP30R adhesives are similar.

Figure 4a shows the logarithm of the storage modulus (log*E'*) obtained for the PU, PCP0 and PCP30R adhesives by DMTA analysis. It can be observed that the polyurethane adhesive is more elastic than the polychloroprene adhesives. On the other hand, the phenolic resin added to the polychloroprene adhesive increases its storage or elastic modulus. Thus, the addition of this phenolic resin to the adhesive formulation improves the rheological properties of the polychloroprene adhesive. The tanδ curves (Figure 4b) obtained for the three adhesives (PU, P0 and P30R) display the same behaviour than the log*E'* curves.

On the other hand, the dry solid film of polyurethane adhesive shows the highest surface energy (47.2 mJ/m²) (Table 4), which is more similar to chlorinated rubber surface energy (51.2 mJ/m²) (Table 3). On the other hand, polychloroprene

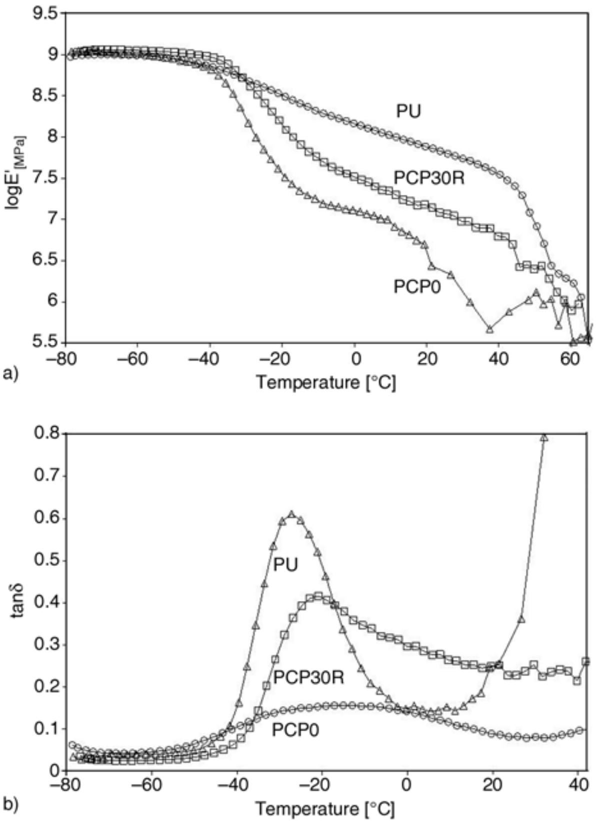

Figure 4. (a) Log*E*' (storage modulus) *versus* temperature and (b) tanδ versus temperature for PU, PCP0 and PCP30R adhesives

adhesives present similar surface energy (38 mJ/m^2) (Table 4).

Chemistry of the adhesives was analyzed by ATR-IR spectroscopy (Figure 5). The ATR-IR spectrum of the polyurethane film shows typical bands due to N–H stretching at 3330 cm^{-1}, C–H stretching at 2955 and 2855 cm^{-1}, C=O stretching due to urethane at 1725 cm^{-1}, aromatic C–C stretching at 1600 cm^{-1}, N–CO stretching, N–H bending and C–N stretching due to urethane at 1530 cm^{-1}, C–H bending at 1460 cm^{-1}, C–N stretching and N–H bending at and 1260 cm^{-1}, C–O–C stretching at 970, 1065, 1165 and N-H out of plane deformation at 730 cm^{-1}. The ATR-IR spectra of PCP0 and PCP30R polychloroprene adhesives show the following absorption bands: =C–H stretching of aromatic rings (3025 cm^{-1}), C–H stretching (2910, 2860 cm^{-1}), C=C stretching (1650 cm^{-1}), C–H bending (1445 cm^{-1}), out of plane bending =C–H (820, 780, 675 cm^{-1}), C–Cl stretching (820 cm^{-1}). PCP30R polychloroprene adhesive also shows absorption from the thermoreactive phenolic: aromatic C–C stretching (1600 cm^{-1}), asymmetric C–H bending (1480 cm^{-1}), CO–H bending and symmetric C–H bending (1360 cm^{-1}), out of plane C–O stretching (1210 cm^{-1}), asymmetric C–O–C stretching (1070 cm^{-1}) and symmetric C–O–C stretching and aromatic C–H out of plane bending (875 cm^{-1}). On the other hand, the ATR-IR spectrum of the roughened leather used in the adhesive joints (Figure 5) shows several bands due to collagen (the main constituent of animal skin): N–H and C–N bands (N–H stretching at 3300 cm^{-1}, C–N stretching and N–H bending at 1540 cm^{-1}, C–N bending at 1240 cm^{-1}), methylene bands (C–H stretching at 2920 and 2845 cm^{-1}, C–H bending at 1450 cm^{-1}), and ester bands (C=O stretching at 1650 cm^{-1}, C–O stretching at 1030 cm^{-1}).

Table 4. Contact angle measurements (bidistilled-deionized water and methane diiodide), total (γ_s), polar (γ_s^p) and dispersive (γ_s^d) components of the surface energy of dry solid adhesive films (PU, PCP0 and PCP30R)

Adhesive	θH_2O [°]	θCH_2I_2 [°]	γ_s^d [mJ/m^2]	γ_s^p [mJ/m^2]	γ_s [mJ/m^2]
PU	69±2	27±2	39.7	7.6	47.2
PCP0	72±2	51±1	27.5	10.2	37.7
PCP30R	84±2	43±2	35.4	2.9	38.2

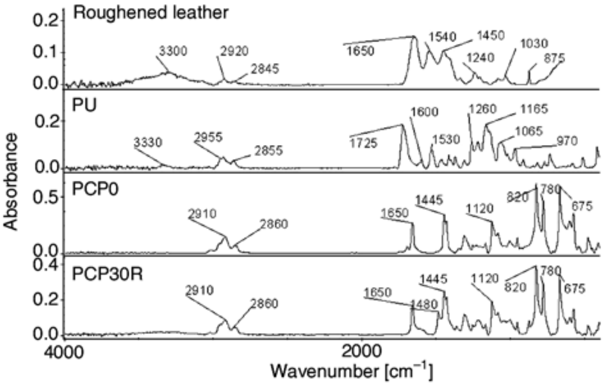

Figure 5. ATR-IR spectra of the roughened leather, PU, PCP0 and PCP30R adhesives before joint formation

3.2.2. Elimination of the reactivation process in the adhesion of chlorinated SBS rubber with polychloroprene adhesive

Table 5 shows that the treatment of the SBS rubber with TCI/MEK improves the adhesion properties of the rubber to PU and PCP30R adhesives. However, the chlorinated SBS rubber exhibits poor adhesion properties to PCP0 adhesive. In all cases the dry adhesive film was melted at 80°C under infrared radiation (reactivation process) and immediately

Table 5. T-peel strength [kN/m] obtained for joints produced between as-received and TCI/MEK-treated SBS rubber and roughened leather using PU, PCP0 and PCP30R adhesives. Failure mode: *A* – adhesion failure; *M* – cohesive in the rubber failure (failure obtained by ATR-IR spectroscopy on both failed surfaces)

	T-peel strength [kN/m] (Failure mode)	
Adhesive	**As received**	**TCI/MEK**
PU	0.2±0.1 (*A*)	6.1±0.1 (*M*)
PCP0	0.7±0.1 (*A*)	0.4±0.1 (*A*)
PCP30R	0.2±0.1 (*A*)	6.9±0.1 (*M*)

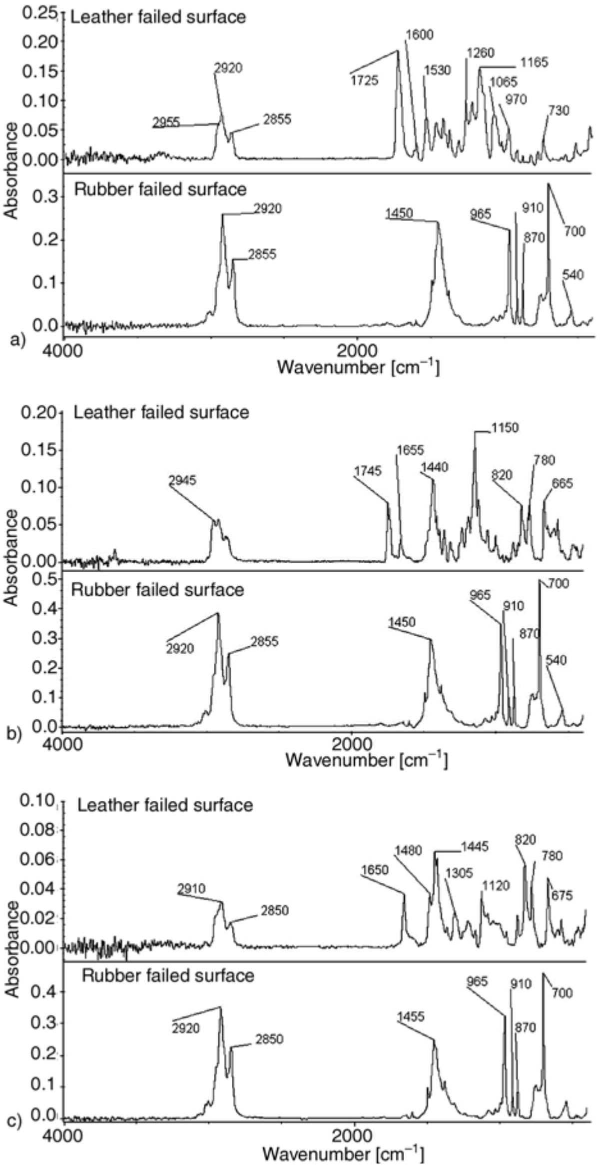

Figure 6. ATR-IR spectra of the failed surfaces obtained after T-peel test of (a) as-received SBS rubber/PU adhesive/roughened leather joint; (b) as-received SBS rubber/PCP0 adhesive/roughened leather joint; (c) as-received SBS rubber/PCP30R adhesive/roughened leather joint

placed into contact under a pressure of 0.8 MPa for 10 seconds to achieve a suitable joint.

The T-peel strength values obtained for the adhesive joints prepared with chlorinated SBS rubber using PU and PCP30R adhesives were high and a cohesive in the chlorinated rubber failure (*M*) was obtained, while an adhesion failure (*A*) was obtained for joints produced with the as-received SBS rubber. The failure mode was assessed by ATR-IR spectroscopy comparing ATR-IR spectra of as-received rubber (Figure 1), leather and adhesives (Figure 5) to ATR-IR spectra of failed surfaces (Figures 6 and 7). Thus, Figure 6 shows that on the leather failed surfaces adhesive absorption is present while the rubber failed surfaces shows absorption from rubber. Thus, adhesion failure is produced with as-received rubber (Figure 8a) irrespective of the adhesive used (polyurethane or polychloroprene). On the other hand, Figures 7a and 7c show the absorption bands from chlorinated rubber (C–H bending of $–CH_2Cl$ at 1420 cm^{-1} and C–Cl stretching at 760 and 540 cm^{-1}) on both failed surfaces, indicating that a cohesive in the chlorinated rubber failure is produced (Figure 8b) when using polyurethane adhesive or polychloroprene adhesive with a phenolic resin in its formulation (PCP30R).

However, Figure 7b shows polychloroprene absorption on the leather failed surface and rubber absorption on the rubber failed surfaces. Consequently, when using a polychloroprene adhesive with no resin in its formulation (PCP0) in the joints between chlorinated SBS rubber and roughened leather, a low T-peel strength value was obtained (Table 5) and a mainly adhesion to rubber failure (*A*) mode (Figure 8a). Thus, the addition of the phenolic resin to the polychloroprene adhesive formulation is appropriate to obtain good adhesion performance with a polychloroprene adhesive.

As the reactivation process is time consuming and temperature must be carefully controlled, reactivation process was eliminated from the adhesive joints preparation (Figure 8c) when using the PCP30R polychloroprene adhesive. This is possible as open time (time when tack properties are maintained) for polychloroprene adhesive is longer than for polyurethane adhesive (Figure 3). Adhesive reactivation is not necessary with the PCP30R adhesive as a considerable high T-peel strength value (5.7±0.3 kN/m) was obtained in the joint

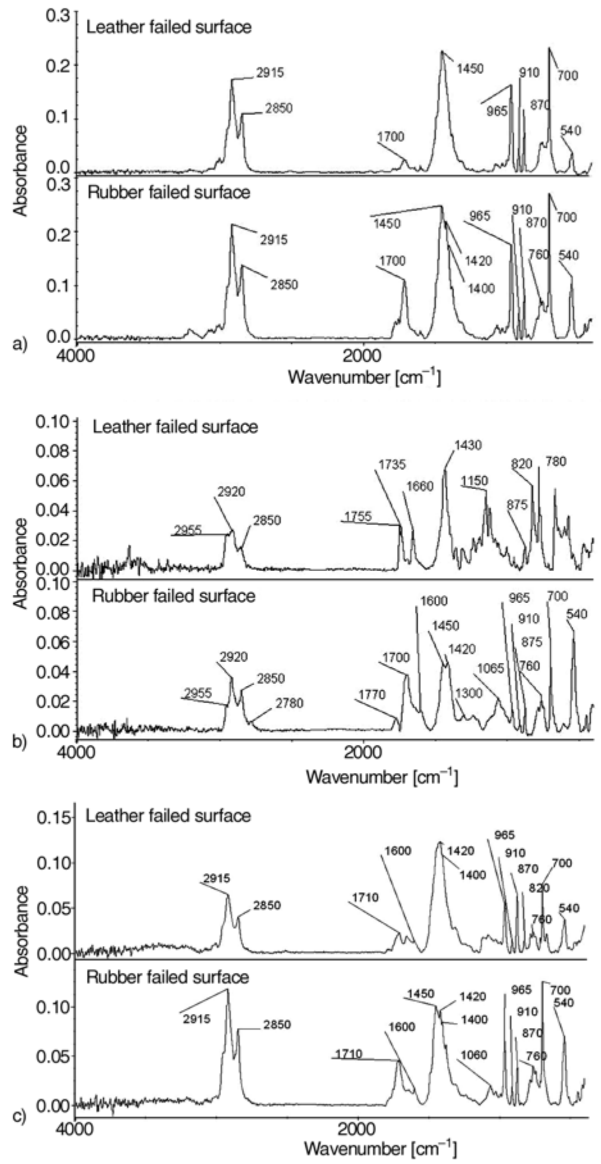

Figure 7. ATR-IR spectra of the failed surfaces obtained after T-peel test of (a) chlorinated SBS rubber/PU adhesive/roughened leather joint; (b) chlorinated SBS rubber/PCP0 adhesive/roughened leather joint; (c) chlorinated SBS rubber/PCP30R adhesive/roughened leather joint

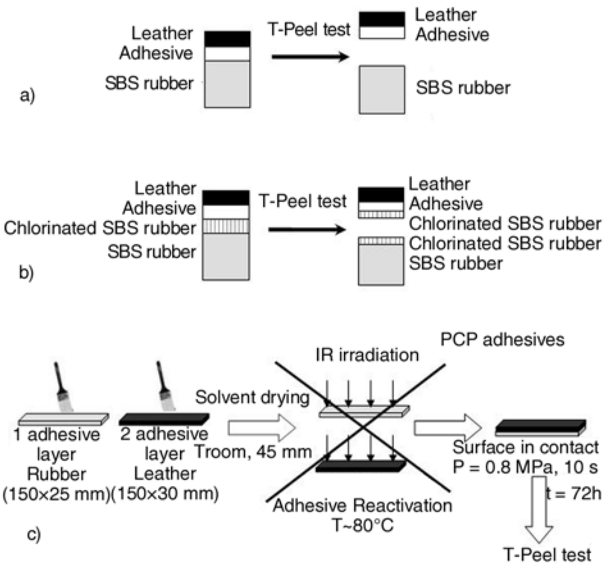

Figure 8. (a) Adhesion failure mode; (b) cohesive in the chlorinated rubber failure mode; (c) Preparation of adhesive joints

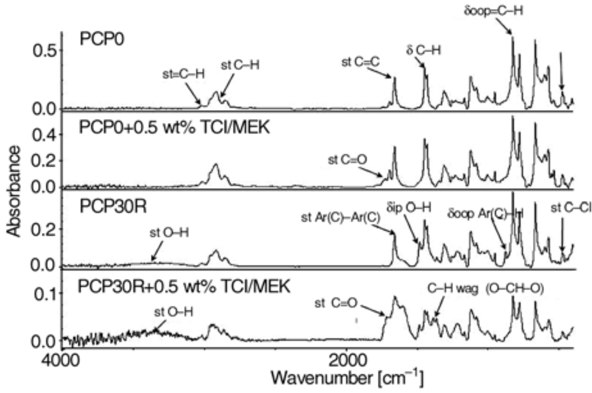

Figure 9. ATR-IR spectra of PCP0 and PCP30R adhesive films before and after immersion in a 0.5 wt% TCI/MEK solution

between chlorinated SBS rubber and roughened leather using a not reactivated PCP30R adhesive, value that is just slightly lower than the T-peel strength value obtained for the reactivated PCP30R adhesive (6.9 kN/m) (Table 5).

Previous studies dealing with the interface produced between polyurethane adhesive and chlorinated SBS rubber showed that chlorination of the polyurethane adhesive was produced by the unreacted TCI deposited on the treated SBS rubber. The creation of an interface with a distinctive chemistry resulted in the improvement of the adhesion properties of the treated SBS rubber towards polyurethane adhesive [12–15]. Therefore, possible chlorination of the polychloroprene adhesives was considered and both PCP0 and PCP30R solid adhesive films were immersed in the chlorinating solution.

ATR-IR spectra (Figure 9) were obtained for PCP0 and PCP30R adhesive films before and after immersing the adhesive films in a 0.5 wt% TCI/MEK solution during 10 s. It can be observed that the PCP0 adhesive film was not modified by immersion in a 0.5 wt% TCI/MEK solution. Only a weak absorption band due to C=O stretching can be observed. However, the PCP30R adhesive film reacts with TCI to create C=O moieties (C=O stretching at 1720 cm^{-1}) and O–CH–O moieties (C–H wag vibration at 1385 cm^{-1}).

Consequently, the improvement of the rheological properties of the polychloroprene adhesive produced by the addition of a thermoreactive phenolic resin (which imparts elasticity to the polychloroprene adhesive) together with the ability of chlorination of the polychloroprene adhesive by the TCI may be responsible for the good adhesion performance.

4. Conclusions

The surface treatment with a 3 wt% TCI/MEK increases the SBS rubber surface energy and introduces surface roughness improving the adhesion properties of the SBS rubber surface towards PU and PCP30R adhesives.

The rheological properties and the adhesion properties of the polychloroprene adhesive towards chlorinated SBS rubber improved by addition of a thermoreactive phenolic resin in its formulation. The presence of a thermoreactive phenolic resin in the polychloroprene adhesive formulation imparts elasticity and also favours the oxidation of the adhesive film by TCI, resulting in good adhesion properties.

It is possible to eliminate the reactivation process from the adhesive joint formation when using a polychloroprene adhesive with a thermoreactive phenolic resin in its formulation.

Acknowledgements

Financial support from Science and Technology Ministry – MCYT, Spain (project MAT 2001-0625-C02-01) and Generalitat Valenciana, Spain (project GV04B-567) is gratefully acknowledged. The authors would like to thank INSOCO (Elche, Alicante, Spain) for supplying polychloroprene and polyurethane; SYNTHELAST (Elche, Alicante, Spain) for providing the SBS rubber used in this research; SAFIC-ALCAN (Barcelona, Spain) for supplying the resins used in this study.

References

[1] Langerwerf J. S. A.: Halogenation: bonding without roughing. Schuh-Technik, **6**, 731–733 (1973).

[2] Wadell W., Evans L., Gillick J., Shuttleworth D.: Polymer surface modification. Rubber Chemistry and Technology, **65**, 687–696 (1992).

[3] Pettit D., Carter J. A.: Behaviour of urethane adhesives on rubber surfaces. Journal of Adhesion, **5**, 333–349 (1973).

[4] Oldfield D., Symes T. E. F.: Surface modification of elastomers for bonding. Journal of Adhesion, **16**, 77–95 (1983).

[5] Lawson D. F., Kim K. J., Fritz T. L.: Chemical modifications of rubber surfaces: XPS survey of the reactions of thrichloroisocyanuric acid at the surfaces of vulcanized elastomers. Rubber Chemistry and Technology, **69**, 245–252 (1996).

[6] Pedrón-Haba S., Sánchez-Navarro M. M., Arán-Aís F., Torró-Palau A. M., Orgilés-Barceló A. C.: Properties of polychloroprene adhesives containing terpene phenolic resin tackifiers in 'Proceedings of the 28th Annual Meeting of the Adhesion Society, Mobile, USA' 267–269 (2005).

[7] Gardziella A., Pilato L. A., Knop A.: Phenolic Resins. Chemistry, Applications, Standardization, Safety and Ecology. Springer, Berlin (2000).

[8] Pastor-Blas M. M., Sánchez-Adsuar M. S., Martín-Martínez J. M.: Surface modification of synthetic vulcanized rubber. Journal of Adhesion Science and Technology, **8**, 1093–1114. (1994).

[9] Owens D. K., Wendt R. C.: Estimation of the surface free energy of polymers. Journal of Applied Polymer Science, **13**, 1741–1747 (1969).

[10] Romero-Sánchez M. D., Pastor-Blas M. M., Martín Martínez J. M.: Improved adhesion between polyurethane and SBR rubber treated with thrichloroisocyanuric acid solutions containing different concentrations of chlorine. Composite Interfaces, 10, 77–94 (2004).

[11] Pastor-Blas M. M., Sánchez-Adsuar M. S., Martín-Martínez J. M.: Weak surface boundary layers in styrene-butadiene rubber. Journal of Adhesion, **50**, 191–210 (1995).

[12] Pastor-Blas M. M., Ferrándiz-Gómez T. P., Sepulcre-Javaloyes P. D., Martín-Martínez J. M.: Degradation of a styrene-butadiene-styrene rubber treated with an excess of thrichloroisocyanuric acid in 'Polymer Analysis and Degradation' (eds.: Jiménez, A., Zaikov, G. E.) Nova Science Publishers, New York, 193–212 (2000).

[13] Pastor-Blas M. M., Martín-Martínez J. M., Boerio F. J.: Mechanisms of adhesion in surface chlorinated thermoplastic rubber/thermoplastic polyurethane adhesive joints. Rubber Chemistry and Technology, **75**, 825–837 (2002).

[14] Pastor-Blas M. M., Martín-Martínez J. M., Boerio F. J.: Influence of chlorinating solution concentration on the interactions produced between chlorinated thermoplastic rubber and polyurethane adhesive at the interface. Journal of Adhesion, **78**, 39–77 (2002).

[15] Pastor-Blas M. M., Martín-Martínez J. M., Boerio F. J.: Study of the interface between chlorinated thermoplastic rubber and polyurethane adhesive in 'Trends in Molecular and High Molecular Science', (eds. Zaikov, G. E., Monakov, Y. B., Jiménez, A.) Nova Science Publishers, New York, 53–66 (2005).

eXPRESS Polymer Letters Vol.1, No.4 (2007) 245–251
Available online at www.expresspolymlett.com
DOI: 10.3144/expresspolymlett.2007.37

Effect of nucleating agents on crystallization kinetics of PET

X. L. Jiang[*1], *S. J. Luo*[1], *K. Sun*[1], *X. D. Chen*[2]

[1]State Key Laboratory of Metal Matrix Composites, Shanghai Jiao Tong University, Shanghai 200030, China
[2]Shanghai Sunny New Technology Development Co. Ltd., Shanghai, 201108, China

Received 27 January 2007; accepted in revised form 7 April 2007

Abstract. Effects of three nucleating agents concluding talc, sodium benzoate (SB) and an ionomer (Ion., Na^+) on crystallization of poly(ethylene terephthalate) (PET) were studied by differential scanning calorimetry (DSC) and polarized optical microscope (POM), the parameters of crystallization kinetics were obtained through Avrami and Ozawa equations. The fold surface free energy σ_e of pure PET and PET/nucleating agent blends was calculated by Hoffman-Lauritzen theory. The results indicate that the three kinds of nucleating agents increase the crystallization rate constant through promoting their nucleating effect for PET crystallization, among which SB is the best one with the same content. The crystallization mode of PET might shift from three-dimensional growth to two-dimensional growth by the addition of the nucleating agents. The values of σ_e of PET/nucleating agent blends are much less than that of pure PET, and PET/SB (99:1) blend has the least value of σ_e (18.2 mJ/m^2). The conclusion based on Hoffman theory is similar to the analysis by Avrami and Ozawa equations.

Keywords: *thermal properties, poly(ethylene terephthalate) (PET), nucleating agents, crystallization kinetics*

1. Introduction

Poly(ethylene terephthalate) (PET) has already been widely used in the production of fiber, film, bottles and engineering plastics, which derives from its good balance of thermal and mechanical properties. However, it has not gained noticeable application in the field of injection molding because of its low crystallization rate. In order to accelerate the crystallization rate of PET and obtain the desired morphology and properties, a great deal of effort has been made into studying the crystallization kinetics corresponding to the change of the performed properties [1–9].

It is generally considered that the addition of nucleating agents gives rise to increase the crystallization rate of PET [10–13]. A number of suggestions have been reported to add different substances acting as nucleating agents to PET in order to improve its applied or processing properties. The additives exert an influence on the rate of the crystallization process, its morphology, the spherulite size and its distribution and so the physical properties of final product [14–16].

The nucleating agents can be mainly divided into three kinds: inorganic additives, organic additives and polymers, the nucleating effect on PET crystallization depends on several aspects, such as the size and geometry of the particles, the surface structure and interfacial interactions with the polymer matrix [10–12]. A lot of study has discussed the effect of a single nucleating agent on the crystallization of PET, but this paper focuses on the effect of three kinds of nucleating agents on the crystallization kinetics of PET, such as talc, sodium benzoate (SB) and an ionomer (Ion., Na^+) which belongs to inorganic additives, organic additives and polymers, respectively. Based on Hoffman-Lauritzen theory,

---

[*]Corresponding author, e-mail: jx1110@sjtu.edu.cn

© BME-PT and GTE

the fold surface free energy σ_e, of PET/nucleating agent blends are compared with that of pure PET.

2. Experimental

2.1. Materials

Poly(ethylene terephthalate) (PET) with the intrinsic viscosity of 0.80 dl·g^{-1} was produced by Jinshan Petroleum Chemistry Company (Shanghai, China). The nucleating agents were included talc, sodium benzoate (SB) and an ionomer Na$^+$. The talc (800 mesh) was supplied by Haicheng Company (Zhejiang, China). The sodium benzoate with analytically pure was supplied by Shanghai Chemical Reagent Company (Shanghai, China). The ionomer Na$^+$ (Surlyn 8920) with the melting point of 88°C was supplied by DuPont Company (the United States). Figure 1 shows the chemical structure of the ionomer Na$^+$.

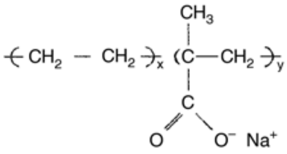

Figure 1. The chemical structure of the ionomer Na$^+$

2.2. Sample preparation

Before the blending, PET was dried in a vacuum oven at 80°C for 10 h. The talc, the sodium benzoate, and the ionomer Na$^+$ were all dried under vacuum at 60°C for 10 h. PET was mixed with three kinds of nucleating agents above in the chamber of a Haake Rheometer RC90 (Germany) at 265°C and 80 rpm, respectively. The mix process lasted about 5 min, the composition was moved out and used for all differential scanning calorimetry (DSC) studied on crystallization kinetics.

2.3. DSC analysis

The crystallization behavior was analyzed with a PerkinElmer Paris 1 DSC instrument in a nitrogen atmosphere. The specimens were weighted in the range 5 to 6 mg. Overall crystallization rate studies were carried out on completely amorphous samples. For the cases of nonisothermal crystallization, the samples were heated to 265°C at a rate of 10°C/min and held for 5 min to erase all previous thermal history. The first cooling runs at rates of 5, 10, 15 and 20°C/min from 265°C to room temperature were recorded.

For isothermal crystallization experiments, the samples were heated to 265°C at a rate of 10°C/min and held for 5 min to erase all previous thermal history, then cooled rapidly (100°C/min) to the proposed crystallization temperature (T_c) and maintained at that temperature for the time necessary for the complete crystallization of pure PET and PET/nucleating agent blends. The enthalpy evolved during the isothermal crystallization was recorded as a function of time at different T_c's. After crystallization, the samples were heated to 265°C at a rate of 10°C/min. The melting temperature (T_m) and enthalpy of fusion (ΔH_f) values of the composites were calculated from the maximum and the area under the endothermic peak, respectively.

3. Results and discussion

3.1. The isothermal crystallization kinetics of PET based on Avrami equation

The crystallization kinetics of polymers under isothermal conditions for various modes of nucleation and growth can be well approximated by the known Avrami equation [17, 18]. The general form of the Equation (1) is:

$$X_t = 1 - \exp(-K_t t^n) \qquad (1)$$

where X_t is the relative crystallinity at different crystallization times, n is a constant depending on the mechanism of nucleation and the form of crystal growth, and K_t is crystallization rate constant related to nucleation and growth parameters. X_t can be calculated according to Equation (2):

$$X_t = \frac{Q_t}{Q_\infty} = \frac{\int_0^t \frac{\mathrm{d}H}{\mathrm{d}t}\mathrm{d}t}{\int_0^\infty \frac{\mathrm{d}H}{\mathrm{d}t}\mathrm{d}t} \qquad (2)$$

where Q_t and Q_∞ are the amounts of enthalpy generated at time t and infinite time t_∞, respectively, and dH/dt is the enthalpy evolution rate.

The Avrami equation can be written as follows (3):

$$\ln[-\ln(1 - X_t)] = n\ln t + \ln K_t \qquad (3)$$

From a graphic representation of $\ln[-\ln(1 - X_t)]$ versus $\ln t$, n (the slope of the straight line) and the

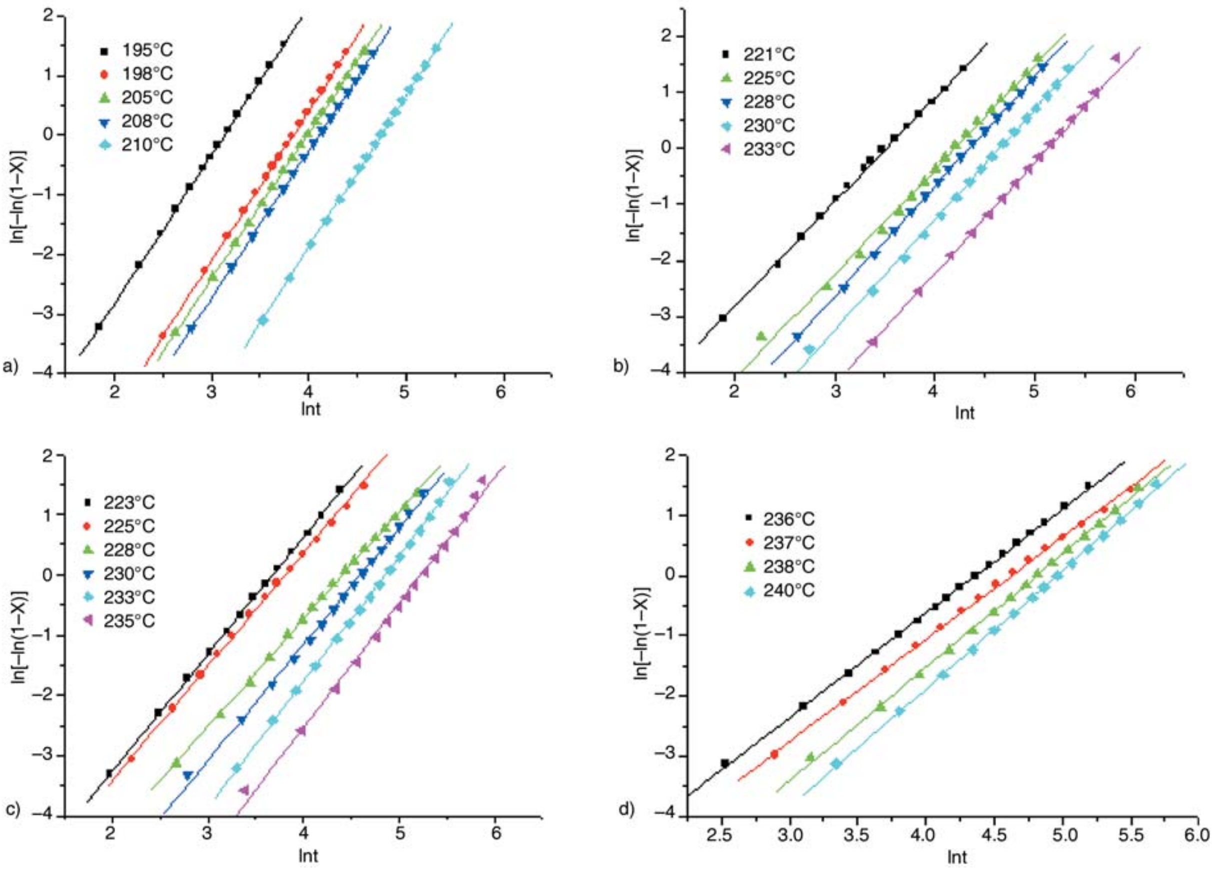

Figure 2. Plots of ln[–ln(1–X_t)] *versus* ln t for isothermal crystallization of pure PET and PET/nucleating agent blends. (a) pure PET; (b) PET/talc = 99:1; (c) PET/Ion., Na+ = 99:1; (d) PET/SB = 99:1

crystallization rate constant K_t (the intersection with the y axis) can be obtained. The plots of ln[–ln(1 – X_t)] *versus* ln t are shown in Figure 2 and the parameters are listed in Table 1. As shown in Table 1, the crystallization rate constant K_t of pure PET and PET/nucleating agent blends decreases with increasing temperature. K_t of PET/nucleating agent blends is larger than that of pure PET, and PET/SB (99:1) blend has the largest K_t. The results show that three nucleating agents can increase the crystallization rate of PET, the nucleating effect of the ionomer Na^+ is slightly better than that of the talc, SB has the most excellent nucleating effect for the crystallization of PET according to the same content of nucleating agent.

Generally, for most of crystallization polymers, the value of Avrami exponent n was found to vary between 1 and 4, corresponding to various growth forms from rod-like to sphere-like [4, 19]. The Avrami model lumps together the formation of nuclei and their subsequent growth. As shown in Table 1, the Avrami exponent n for pure PET is close to 2.5, it shows that the crystallization mode is a three-dimensional growth of nuclei [20]. While

Table1. Parameters of isothermal crystallization from Avrami equation (T_c: the crystallization temperature, K_t: the crystallization rate constant, n: the Avrami exponent, $t_{1/2}$: the crystallization half-time)

Samples	T_c [°C]	K_t	n	$t_{1/2}$ [s]
Pure PET	195	$3.841\cdot10^{-4}$	2.51	49.8
	198	$6.086\cdot10^{-5}$	2.53	100.2
	205	$5.739\cdot10^{-5}$	2.45	120.0
	208	$3.949\cdot10^{-5}$	2.47	150.6
	210	$5.179\cdot10^{-6}$	2.57	234.6
PET/talc = 99:1	221	$1.503\cdot10^{-3}$	1.85	27.0
	225	$4.062\cdot10^{-4}$	1.86	55.2
	228	$2.035\cdot10^{-4}$	1.96	63.0
	230	$1.104\cdot10^{-4}$	1.96	87.0
	233	$4.111\cdot10^{-5}$	1.97	139.2
PET/Ion., Na^+ = 99:1	223	$7.916\cdot10^{-4}$	1.94	32.4
	225	$7.808\cdot10^{-4}$	1.88	36.6
	228	$3.796\cdot10^{-4}$	1.78	66.0
	230	$1.421\cdot10^{-4}$	1.93	83.4
	233	$4.130\cdot10^{-5}$	1.98	109.2
	235	$2.066\cdot10^{-5}$	1.96	160.8
PET/SB = 99:1	236	$5.097\cdot10^{-4}$	1.74	63.6
	237	$3.878\cdot10^{-4}$	1.70	80.4
	238	$1.168\cdot10^{-4}$	1.88	101.4
	240	$5.797\cdot10^{-5}$	1.97	118.8

the values of n for PET/nucleating agent blends are found to below 2. This indicates that the crystallization mode of PET might shift to two-dimensional growth with heterogeneous nucleation [20]. The result shows that the crystallization mode of PET has been changed by the addition of nucleation agents.

The crystallization half-time $t_{1/2}$ is defined as the time at which the extent of crystallization is completed 50%. The shorter the half-time, the faster the crystallization rate. It can be determined from the measured kinetic parameters [21–22] (4):

$$t_{1/2} = \left(\frac{\ln 2}{K_t}\right)^{1/n} \tag{4}$$

The value of $t_{1/2}$ is listed in Table 1. $t_{1/2}$ increases with increasing crystallization temperature T_c. A higher crystallization temperature leads to a lower supercooling degree, the nuclei for the crystallization are more difficult to form.

3.2 The nonisothermal crystallization kinetics of PET based on Ozawa equation

There are several modes for the study of non-isothermal crystallization kinetics of polymers. The Avrami equation can be directly used to study non-isothermal crystallization, but it didn't take into account the effect of the constant cooling on the crystallization, so the non-linearity of Avrami plots were often obtained. While accounting for the effect of cooling (or enthalpying) rate Φ on crystallization from the melt (or the glassy state), Ozawa [23] amended and extended Avrami equation, and the Ozawa equation is (5):

$$X(T) = 1 - \exp\left(-\frac{K(T)}{\Phi^m}\right) \tag{5}$$

where Φ is the cooling rate, m is the Ozawa exponent that depended on the crystal growth and nucleation mechanism and $K(T)$ is the crystallization rate constant.

The Ozawa equation can be written Equation (6).

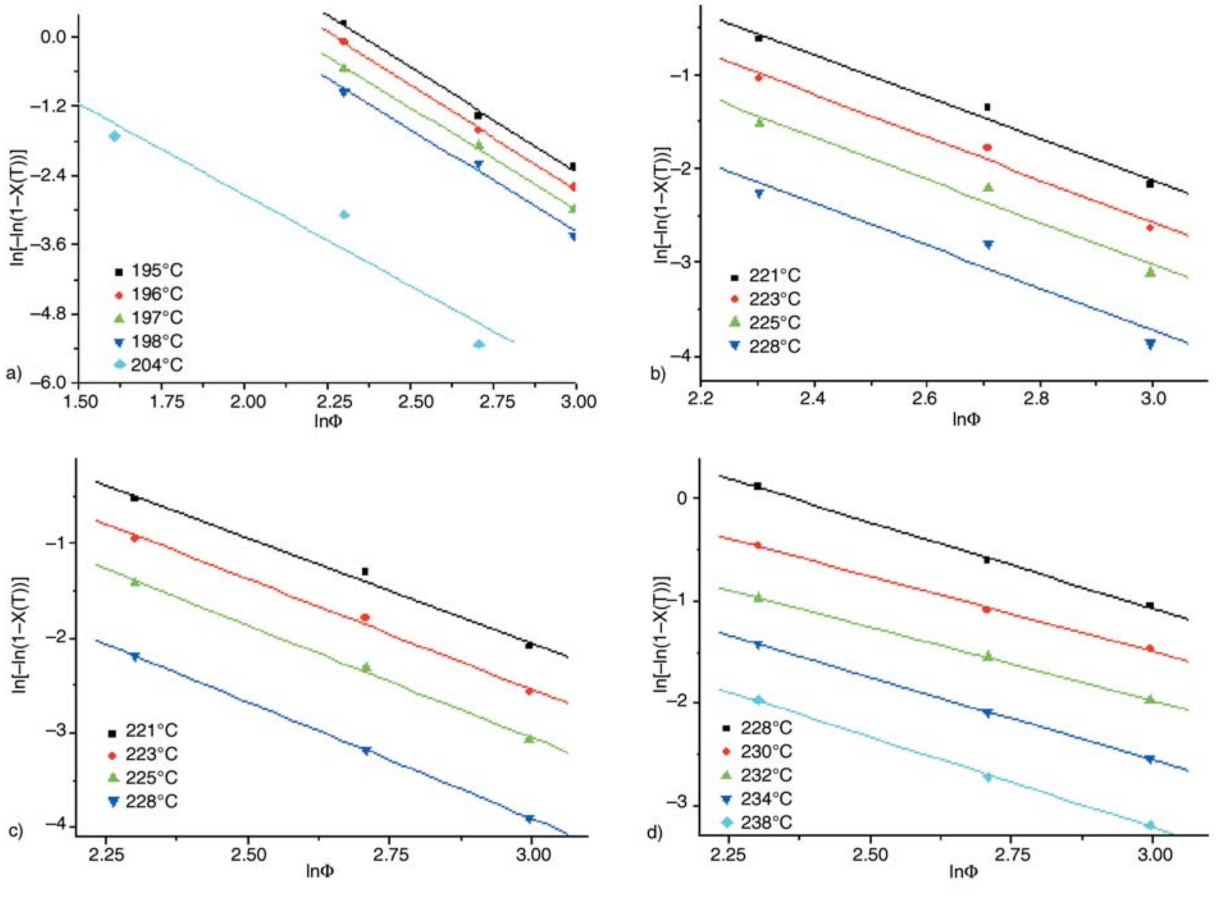

Figure 3. Plots of ln{–ln[1–$X(T)$]} *versus* lnΦ for nonisothermal crystallization of pure PET and PET/nucleating agent blends. (a) pure PET; (b) PET/talc = 99:1; (c) PET/Ion., Na^+ = 99:1; (d) PET/SB = 99:1

Table 2. Parameters of nonisothermal crystallization from the Ozawa equation (T: the crystallization temperature, $K(T)$: the crystallization rate constant, m: the Ozawa exponent)

Sample	T [°C]	lnK(T)	m
Pure PET	195	8.49	3.61
	196	8.25	3.63
	197	7.53	3.50
	198	7.26	3.54
	204	3.56	3.14
PET/talc = 99:1	221	4.50	2.21
	223	4.24	2.27
	225	3.78	2.27
	228	3.01	2.25
PET/Ion., Na$^+$ = 99:1	221	4.64	2.23
	223	4.45	2.33
	225	4.09	2.38
	228	3.48	2.41
PET/SB = 99:1	228	3.99	1.69
	230	2.93	1.47
	232	2.35	1.44
	234	2.30	1.62
	236	2.09	1.77

$$\ln\{-\ln[1 - X(T)]\} = \ln K(T) - m\ln\Phi \qquad (6)$$

According to Equation (6), $\ln\{-\ln[1 - X(T)]\}$ against $\ln\Phi$ is plotted in Figure 3. The Ozawa plots of linear relationship between and $\ln\Phi$ shows that the Ozawa equation can be priority to explain the nonisothermal crystallization behavior of pure PET and PET/nucleating agent blends. The Ozawa parameters, m and crystallization rate constant $K(T)$, can be obtained through the slope and intercept of the fitting for those data shown in Figure 3 and listed in Table 2.

The value of the Ozawa exponent m for pure PET is almost equal to 3, in good agreement with the results reported by Ozawa [23]. In general, an Ozawa exponent $m = 3$ suggests that the mode at the nonisothermal crystallization of PET is of three-dimensional growth with an athermal nucleation mechanism. While the values of m for PET/nucleating agent blends are below 3. This indicates that the crystallization mode might change, which also found in isothermal crystallization process.

The crystallization rate constant $K(T)$ of pure PET and PET/nucleating agent blends decreases with increasing temperature. $K(T)$ of PET/nucleating agent blends is higher than that of pure PET. This also indicates that the crystallization rate of PET increases by the addition of the nucleating agent. PET/SB (99:1) blend has the largest value of $K(T)$ at the same temperature. So among three kinds of nucleating agents, SB has the most excellent nucleating effect for PET crystallization. The nucleating effect of Ion., Na$^+$ is slightly better than that of the talc which is the same as the analysis of isothermal crystallization.

3.3. The fold surface free energy based on Hoffman-Lauritzen relationship

In studying the crystallization kinetics of crystalline polymers, we need to know the equilibrium melting temperature (T_m^0) to calculate the degree of supercooling [23]. After crystallization at T_c, T_m was obtained by the reheating of the samples at a rate of 10°C/min. It was possible to calculate T_m^0 by the plotting of T_c *versus* T_m and to observe the intersection of this line with another line with a slope equal to 1 ($T_m = T_c$) [24]. Plots of T_m against T_c are shown in Figure 4, and the values of T_m^0 are listed in Table 3.

The crystallization rates at different temperatures were expressed in the form of reciprocal of crystallization half-time $t_{1/2}$. Using Hoffman-Lauritzen relationship between the radial growth rate of crystal and crystallization temperature based on crystallization regime theory [25], and following Chan and Isayev [26] $(1/t_{1/2})$ and $(1/t_{1/2})_0$ were used to

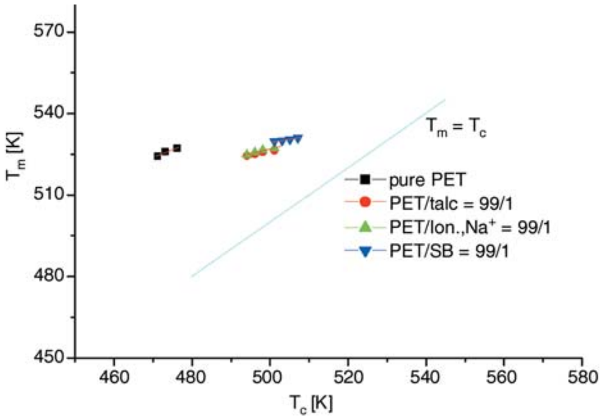

Figure 4. The determination of the equilibrium melting temperature

Table 3. Thermodynamic characteristics of the PET and PET/nucleation agent blends (T_m^0: the equilibrium melting temperature, σ_e: the fold surface free energy)

	Pure PET	PET/talc (99:1)	PET/Ion., Na$^+$ (99:1)	PET/SB (99:1)
T_m^0 [K]	568	542	541	536
σ_e [mJ/m^2]	80.3	25.4	21.3	18.3

substitute for the growth rate G and a pre-exponential factor G_0, respectively. The temperature dependence of the crystallization half life $t_{1/2}$ is given by Equation (7).

$$\frac{1}{t_{1/2}}=\left(\frac{1}{t_{1/2}}\right)_0 \exp\left[\frac{-U^*}{R(T-T_\infty)}\right]\exp\left[\frac{-K_g}{T(\Delta T)f}\right] \quad (7)$$

where T is the crystallization temperature, R is the universal gas constant, $\Delta T = T_m{}^0 - T$ is the supercooling, and $f = 2T/(T + T_m{}^0)$ is a correction factor accounting for the reduction in the latent enthalpy of fusion as the temperature decreased, $T_m{}^0$ being the equilibrium melting temperature. There are four material constants in Equation (7). $(1/t_{1/2})_0$ is a pre-exponential factor that includes all terms independent of temperature, U^* is the activation energy for the transport of crystallizing units across the phase boundary, T_∞ is the temperature below which such transport ceases, and K_g is the nucleation parameter. According to Hoffman theory [25], the parameters U^* and T_∞ are the recommended values of 6284 J/mol and T_g – 30 K, respectively, T_g being the glass transition temperature. Plots of $\ln(1/t_{1/2}) + U^*/R(T - T_\infty)$ against $1/T(\Delta T)f$ are shown in Figure 5, and the slope of the line is K_g.

The nucleation parameter K_g is given by Equation (8).

$$K_g=\frac{zb\sigma\sigma_e T_m^0}{\Delta H_f k_B} \quad (8)$$

where b is the monomolecular layer thickness, taken to be the perpendicular separation of (010) planes, this is 5.53 Å [2]. σ is the side surface free energy of the polymer crystal, σ_e is the fold surface free energy, ΔH_f is the enthalpy of fusion per unit volume ($2.1\cdot10^8$ J/m^3) [2] and k_B is the Boltzmann constant equaling to $1.35\cdot10^{-23}$ J/mol·K. z is relationship with crystallization regimes of PET. At high crystallization temperatures (above 490 K), corresponding to small degrees of supercooling, regime I kinetics are operative [13]. In this case, surface nucleation involved in crystal growth leads to rapid completion over the surface of the new phase prior to the next nucleation event, and the value of z is 4. According to the crystallization temperature, the crystallization of PET/nucleating agent blends belongs to this regime. At large degrees of supercooling, i. e. below 490 K, regime II are operative [13], where the rates of the secondary nucleation and spread of the molecular strip along the growing face are comparable, in this case, the value of z is 2 and the crystallization of pure PET belongs to this regime. The side surface free energy σ is often estimated as [25] (9):

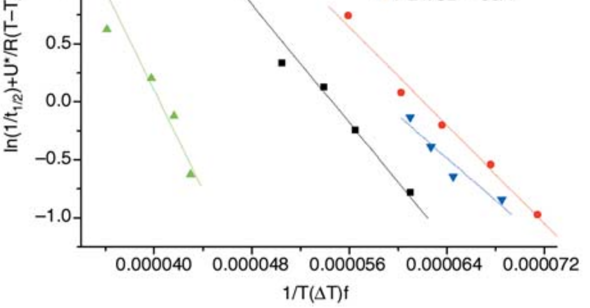

Figure 5. Plots of versus for isothermal crystallization of pure PET and PET/nucleating agent blends

$$\sigma=\alpha\Delta H_f(a_0 b_0)^{1/2} \quad (9)$$

where α was derived empirically to be 0.11 by analogy with the known behavior of hydrocarbons . The unit cell dimensions, a_0 and b_0 for PET used in the analysis are 4.57 and 5.95 Å, respectively [2]. Combining Equation (8) and Equation (9), we can observe the Equation (10) as follows:

$$K_g=\frac{zb\alpha\sigma_e(a_0 b_0)^{1/2}T_m^0}{k_B} \quad (10)$$

σ_e of pure PET and PET/nucleating agent blends are determined, and listed in Table 3.Generally speaking, the smaller the fold surface free energy σ_e, the faster the crystallization rate of polymer crystal. As shown in the Table 3, the value of σ_e of pure PET is 80.3 mJ/m^2, which is in an agreement with reference [25]. The fold surface free energy σ_e of PET/nucleating agent blends are obviously less than that of pure PET, and PET/SB (99:1) blend has the least value of σ_e (18.3 mJ/m^2). The result shows that the conclusion based on Hoffman theory is consistent with the analysis by Avrami and Ozawa equations.

4. Conclusions

The effects of three kinds of nucleating agents, including talc, SB and Ion., Na$^+$ on the crystallization kinetics of PET were studied by using DSC.

The parameters of the isothermal and the non-isothermal crystallization kinetics were obtained through Avrami and Ozawa equations, respectively. The results indicate that three nucleating agents can increase the crystallization rate of PET, and SB has the most excellent nucleating effect for the crystallization of PET with the same content of nucleating agent. The crystallization mode of PET might shift from three-dimensional growth to two-dimensional growth by the addition of the nucleating agents. The fold surface free energy σ_e are obtained by using Hoffman-Lauritzen relationship, the values of σ_e of PET/nucleating agent blends are much less than that of pure PET, and PET/SB (99:1) blend has the least value of σ_e (18.2 mJ/m^2). The conclusion based on Hoffman theory is consistent with the analysis by Avrami and Ozawa equations.

References

[1] Li B. Z., Yu J. Y., Lee S., Ree M.: Crystallizations of poly(ethylene terephthalate co ethylene isophthalate). Polymer, **40**, 5371–5375 (1999).

[2] Rahman M. H., Nandi A. K.: On the crystallization mechanism of poly(ethylene terepthalate) in its blends with poly(vinylidene fluoride). Polymer, **43**, 6863–6870 (2002).

[3] Kong X. H., Yang X. N., Zhou E., Ma D. H.: Non-isothermal crystallization kinetics of ethylene Terephthalate-ethylene oxide segmented copolymers with two crystallizing segments. European Polymer Journal, **36**, 1085–1090 (2000).

[4] Sajkiewicza P., Carpaneto L., Wasiak A.: Application of the Ozawa model to non-isothermal crystallization of poly(ethylene terephthalate). Polymer, **42**, 5365–5370 (2001).

[5] Zhang Z., Ren M., Zhao J., Wu S., Sun H.: Kinetics of non-isothermal cold crystallization of uniaxially oriented poly(ethylene terephthalate). Polymer, **44**, 2547–2551 (2003).

[6] Zhang Y.H., Gu L.X.: Study of non-isothermal crystallization kinetics and sequence distribution in poly(ethylene terephthalate-co-isophthalate). European Polymer Journal, **36**, 759–765 (2000).

[7] Run M. T., Wu S. Z., Zhang D. Y., Wu G.: Melting behaviors and isothermal crystallization kinetics of poly(ethylene terephthalate)/mesoporous molecular sieve composite. Polymer, **46**, 5308–5316 (2005).

[8] Guan B. X., Phillips P. J.: Does isothermal crystallization ever occur? Polymer, **46**, 8763–8773 (2005).

[9] Lu X. F., Hay J. N.: Isothermal crystallization kinetics and melting behaviour of poly(ethylene terephthalate). Polymer, **42**, 9423–9431 (2001).

[10]. Chen Y., Xu M., Li Y. Y., He J. S.: Effect of nucleating agent and nucleation promoter on the crystallization of polyethylene terephthalate. Acta Polymerica Sinica, **20**, 8–14 (1999).

[11] Liu S. L., Ma J. H., Liang B. R.: Study on activity of nucleating agent and promoters for PET. Synthetic Technology and Application, **14**, 6–9 (1999).

[12] Guo R. Y., Wei D. F., Lu H.: Effects of nucleating and nucleation promoter on the crystallization of polyethylene terephthalate. Polymer Materials Science and Engineering, **19**, 121–124 (2003).

[13] Incarnato L., Motta O., Acierno D.: Thermal behaviour of the PET/Rodrun 3000 system. Polymer, **39**, 5085–5091 (1998).

[14] Menczel J., Varga J.: Influence of nucleating agents on crystallization of polypropylene I. talc as a nucleating agent. Journal of Thermal Analysis, **28**, 161–174 (1983).

[15] Zhang M. L., Liu Y. L., Zhang X. H.: The effect of elastomeric nano-particle on the mechanical properties and crystallization behavior of polypropylene. Polymer, **43**, 5133–5138 (2002).

[16] Saujanya C., Radhakrishnan S.: Structure development and crystallization behaviour of PP/nano particulate composite. Polymer, **42**, 6723–6731 (2001).

[17] Avrami M. J.: Kinetics of phase change-I. General theory. Journal of Chemistry and Physics, **7**, 1103–1109 (1939).

[18] Avrami M.: Granulation, phase change and microstructure kinetics of phase change. III. Journal of Chemistry and Physics, **9**, 177–184 (1941).

[19] Jabarin S. A.: Crystallization kinetics of polyethylene terephthalate. I. Isothermal crystallization from the melt. Journal of Applied Polymer Science, **34**, 85–96 (1987).

[20] Garcia D.: Heterogeneous nucleation of poly(ethylene terephthalate). Journal of Polymer Science: Polymer Physics Edition, **22**, 2063–2072 (1984).

[21] Li J., Zhou C. X., Wang G., Tao Y., Liu Q., Li Y.: Isothermal and nonisothermal crystallization kinetics of elastomeric polypropylene. Polymer Testing, **21**, 583–589 (2002).

[22] Arroyo M., Lopez-Manchado M. A., Avalos F.: Crystallization kinetics of polypropylene: II. Effect of the addition of short glass fibres. Polymer, **38**, 5587–5593 (1997).

[23] Ozawa T.: Kinetics of non-isothermal crystallization. Polymer, **12**, 150–156 (1971).

[24] Hoffman J. D., Miller R. L.: Kinetics of crystallization from melt and chain folding in polyethylene fractions revisited: theory and experiment. Polymer, **38**, 3151–3206 (1997).

[25] Hoffman J. D., Davis G. T., Lauritzen J. L.: The rate of crystallization of linear polymers. In: 'Treatise on Solid State Chemistry' (ed.: Hannay N. B.) Plenum Press, New York, Vol. 3, 497–614 (1976).

[26] Chan T. W., Isayev A. I.: Quiescent polymer crystallization: Modeling and measurements. Polymer Engineer and Science, **34**, 461–471 (2004).